PETROLEUM RESEARCH JOURNAL

TECHNICAL PAPERS

ENGINEERING

Numerical Study of Vortex Shedding from Different Shaped Bluff Bodies ...
Abubaker Awidat Salem and Yasser Fathi Nassar 1

Overview of Three-Phase Relative Permeability Experimental Data .....
Mabruk A. Benrewin 11

A New Technique for Converting Acid Core Data to Field Application .....
Nehad ELhemmali and Mohamed Nasr 21

Estimation of the Error Range of True Vertical Depth Determination .....
G. Szigeti 37

Validation of Theoretical Coning Models Using Numerical Single-Well Simulation .....
Salem M. Alakhdar, Abdelhameed A. Urayet and Mabrouk A. Benrewin 43

Modified Approach to Calculate Water Influx (Unsteady State) .....
Jawad Radhi R. Al-Assal 53

EXPLORATION

Veeniacythereis Ibnalhaithami and Veenia (Veenia) ibnalhazmi, Two New Ostracode Species from the Upper Cretaceous of Iraq .....
Jenan M. Taha Al-Bashir 57

Trace Elements and Stable Isotopes For The Abu Ghaylan Formation, Central Jabal Nafusah, NW Libya .....
Mahmoud T. El-Bakai, Aisha K. Shalghoum and Salama R. Ali 65

CHEMISTRY

Determination of Copolymer Composition Monomer Reactivity Ratios and Distribution Sequences of Different Acenaphthalene Copolymers Using the Ultra-Violet Absorption Method .....
Saleh A. Al-Zamzam 77

VOLUME 16 – (2004)

Petroleum Research Centre
P.O.Box 6431, Tripoli
Great Socialist People's Libyan Arab Jamahiriya

Petroleum Res. J. Vol. 16 (2004): P. 1–10, 25 Figs.

Numerical Study of Vortex Shedding from Different Shaped Bluff Bodies

Abubaker Awidat Salem and Yasser Fathi Nassar*

دراسة عددية لظاهرة الدوامات خلف أجسام مختلفة الأشكال

أبو بكر عويدات سالم وياسر فتحي نصار

تم التعامل مع الجريانات المضطربة باستخدام نموذج Baidwi-Lamax وذلك بالاعتماد على برنامج حاسوب متخصص لنماذج الدوامية دالة السريان المشتقة من معادلات Navier-Stokes للجريان اللانضغاطي غير المستقر. كما استخدم البرنامج أيضاً لتحليل السريانات في مقاييس الجريان الدوامية وتحديد أفضل مواصفات الأداء، وتمت مقارنة أرقام Strouhal المحسوبة مع الأرقام التجريبية، حيث أوضحت مجالات السريان أن لشكل الجسم تأثير على حجم وقوة الدوامات المتولدة وكان أكبرها خلف الجسم الأسطواني على هيئة حرف T.

وأعطت الحسابات مؤشراً واضحاً لتكون الدوامات الثانوية قرب جدار المقياس والوجه الأمامي للجسم، هذا بالإضافة إلى تكون الدوامات الابتدائية.

Abstract: *A computer code based on the stream function-vorticity formulation of the unsteady incompressible Navier-Stokes equations has been adapted to treat turbulent flows using the Baidwin-Lamax turbulence model. The code was then used to analyze the flow inside vortex flow meters with the aim of optimizing performance. The computed Strouhal numbers compared well with those acquired experimentally and the computed flow fields indicated how the bluff body shape could influence the size and strength of the shed vortices, with T-shaped cylinder producing the largest vortices. In addition to the primary vortices shed from bluff body, the computations gave a clear indication of the formation of secondary vortices near the meter wall and the front face of the bluff body.*

* Mechanical Engineering Department, University of Sebha, P. 0. Box 53808, Brack, Ash Shati, Libya.
abubakerawidat@hotmail.com

Keywords: vortex shedding; bluff bodies; simulation.

Nomenclature

A+	= 26.0, constant in equation (5)
b	Constant in equation (7)
C_{CP}	= 1.6, constant in equation (8)
C_{KLEP}	= 0.3, constant in equation (11)
C_{WK}	= 0.25, constant in equation (9)
D	Diameter of bluff body
D	Pipe diameter
D_V	Van Driest damping factor
F	Vortex shedding frequency; dominant frequency
$F_{KLEB}(Y)$	Kelebanoff intermittency factor
F_{MAX}	Maximum of function F(Y)
F_{WAKE}	Outer function in equation (10)
K_C	= 0.0 168, Clauser's constant (equations (1)and (8))
K_V	Von Karman's constant (equation (4))
L	Length of vortex shedder in flow direction
Re	Reynolds number
St	Strouhal number

t	Time
T	Dimensionless time
u	Velocity component in x direction
u_τ	Friction velocity
U	Free-stream velocity
V	Velocity component in y direction
X,Y	Cartesian coordinates
Y	Distance from the wall
Y_{max}	Value of Y at which F(Y) (equation (10)) is maximum
δ	Boundary layer thickness
δ^*	Displacement thickness
ν_e	Effective viscosity
ν_l	Laminar viscosity
ν_τ	Turbulent viscosity
X	= 0.4, constant in equation(7)
Ω	Vorticity

INTRODUCTION

The aim of the vortex shedding flow meter manufacture is to produce a device, which efficiently produces strong vortices. This means designing a bluff body, which, with small pressure losses, generates easily detectable vortices whose shedding frequency varies linearly with flow rate over a wide range of Reynolds numbers. Trial and error techniques have been applied widely to perform the development of such meters but they do not necessarily ensure the optimum design of these devices.

New research tools have emerged recently for both experimental and analytical applications. Experimental progress has advanced through Laser Doppler velocimetery, which has been successfully applied to fluid metering research[1,2]. Analytically, computer modeling techniques have been established which might offer an accurate and reliable method for flowmeter improvements[3].

As computer speed and storage capacity have increased in the last two decades, the latter technique has become feasible for handling complex flows, such as unsteady flows, which usually require large amounts of computer time. An early computer simulation of vortex shedding at low Reynolds number was reported by From and Harlow[4]. However, examination of the literature shows that relatively few numerical studies of shedding from bluff bodies have been done. Moreover, most of the work was carried out using a circular cylinder[5] as the vortex shedder, with other bluff bodies receiving much less attention. However, the flow past shedders of rectangular, elliptical and T-shaped cross-section have been studied more recently[6, 7]. Most numerical studies of vortex shedding are performed at fairly low Reynolds numbers in order to exclude the complications by the introductions of a turbulence model. In some of the calculations undertaken, with turbulence modeling, numerical errors might have influenced the results, and, thus, unsatisfactory results are not always attributable to the turbulence model. Here, a turbulence model was added to a laminar computer code[8] in order to study the flow structures around the bluff body at realistic Reynolds numbers.

This paper presents the results of a study designed to extend the laminar computer code[8], based on the stream function-vorticity formulation of the unsteady incompressible Navier- Stokes equation, to treat turbulent flows. The aim is to analyze the flows past the bluff shedder bodies used in many commercial vortex shedding flow meters in order to optimize the bluff body design.

EDDY-VISCOSITY TURBULENCE MODEL

In 1877, Boussineq[9] proposed that the turbulent shear stresses in the momentum equations could be replaced by the product of the mean velocity gradient and a turbulent viscosity ν_τ. The turbulent viscosity was then expressed in terms of auxiliary equations, constructing the turbulence model. In 1925 Prandtl[10] proposed the first turbulence model, which has become known as the mixing-length hypothesis. This model employs an algebraic relation for ν_τ, which is equal to the local product of the magnitude of the mean rate of strain and the square of a characteristic length scale of the turbulent motion.

It is well known that the eddy-viscosity is not constant across a boundary layer, as the turbulence is suppressed close to the wall. Thus, many experiments were performed in order to drive this equation. As a consequence, many algebraic eddy-viscosity models have been produced. One of the most widely used models for the turbulent flow field calculation is that proposed by Cebeci and Smith[11] as double layer turbulence model. This takes the form:

$$(\nu_\tau)_{outer} = K_C U \delta^* [1 + 5.5(Y/\delta)^6]^{-1} \quad (1)$$

where δ is the boundary layer thickness, Y is the normal distance from the wall and K_C is the Clauser constant .This model was then modified[12] by

substituting new relations for conditions at the outer edge of the boundary layer. In particular, the numerical solution was facilitated by eliminating the need to determine the displacement thickness and the boundary layer thickness. This was achieved by introducing two factors, C_{KLEB} and C_{CP}, which were given constant values .The values are discussed later in this section.

In the present investigation, the laminar viscosity v_l in the original laminar program[8] was replaced by:

$$v_e = v_l + v_\tau \tag{2}$$

where v_e is the effective viscosity. The laminar viscosity was assumed constant throughout the present work, while the turbulent viscosity was computed using the Baldwin-Lomax turbulence model[12]. In the Baldwin-Lomax formulation, v_τ is given by:

$$v_\tau = \begin{cases} (v_\tau)_{inner} & Y \le Y_C \\ (v_\tau)_{outer} & Y > Y_C \end{cases} \tag{3}$$

where Y_C is the smallest value of Y at which the values of the viscosity from the inner and outer region formulae are equal. In the inner region, the eddy-viscosity is given by Prandtl-Van Driest formulation:

$$(v_\tau)_{inner} = (K_v Y D_v)^2 \, |\Omega| \tag{4}$$

where K_V is the Von Karman constant and D_V is the Van Driest damping factor, which is given by:

$$D_v = 1 - \exp(-Y / A) \tag{5}$$

where A^+ is a constant and Y^+ is given by:

$$y^+ = \frac{u_\tau}{v_w} \tag{6}$$

where v_w is the kinematic viscosity at the wall and u_τ is the friction velocity. In the present work, v_τ was computed by using Prandtl's velocity distribution law as follows:

$$\frac{u}{u_\tau} = \frac{1}{\chi} \ln Y + b \tag{7}$$

where $\chi = 0.4$ and b are constants. In the outer region, Baldwin and Lomax replaced Clauser's formulation (used by Cebeci and Smith[11]) by the following relation:

$$(v_\tau)_{outer} = K_C \, C_{CP} \, F_{WAKE} \, F_{KLEB}(Y) \tag{8}$$

where C_{CP} is an additional constant. The outer function F_{WAKE} is given by:

$$F_{WAKE} = \text{the smaller of } \left\{ \begin{matrix} Y_{max} F_{max} \\ C_{wk} \, Y_{max} \, u^2_{DIF} / F_{max} \end{matrix} \right\} \tag{9}$$

where C_{WK} is a constant, and F_{MAX} and Y_{MAX} are determined from the function:

$$F(Y) = Y|\Omega|[1 - \exp(-Y^+ / A)] \tag{10}$$

F_{max} is the maximum value that the function F(Y) takes in a local profile , and Y_{MAX} is the value of Y at which F_{max} occurs The function F_{KLEB} (Y) appearing in equation (8) is the Klebanoff intermittency factor, which is given by:

$$F_{KLEB}(Y) = [1 + 5.5 \, (C_{KLEB} \, Y / Y_{max})^6]^{-1} \tag{11}$$

where C_{KLEB} is a constant. The quantity U_{DIF} is the difference between the maximum and minimum total velocity in the profile:

$$u_{DIF} = (\sqrt{u^2 + v^2})_{max} - (\sqrt{u^2 + v^2})_{min} \tag{12}$$

The constants appearing in the above equations were determined by Baldwin and Lomax by requiring the boundary layer profiles computed with the present model to be in agreement with those determined using the Cebeci and Sn jth model mentioned earlier. The values were determined to be:

$A^+ = 26$, $K_V = 0.4$, $K_C = 0.0168$, C_{CP}, $= 1.6$, $C_{KLEB} = 0.3$ and $C_{WK} = 0.25$.

The major difficulty faced here in applying the present model to the calculation of the confined flow past a vortex shedder is to find the correct estimate for Y. This is due to the presence of the shedder walls and as a consequence there is more than one possible Y value. However, the value of Y was computed as the normal to the main flow direction, since this value gave the best results compared with the experimental values.

RESULTS AND DISCUSSION

Using the modified Laminar program and the Baldwin-Lomax turbulence model, the computation

of the flow inside the vortex shedding flowmeter at the bluff body mid-span was performed. This program was also tested with the mixing-length turbulence model but the results are not shown in the present paper due to the poor agreement with the experimental and the current computed values. The parameters involved were the shape of the bluff body and its dimensions, the dimensions of the meter body and the Reynolds number. In order to check the performance of the program together with the turbulence model, all of these parameters were set to the experimental values (detailed in Reference 13), and, therefore, the computed values of Strouhal number are compared with those acquired experimentally for all of the configurations involved. The solution was performed on a uniform (190 x73) mesh, the first number being the number of mesh cells in the x-direction and the second in the y-direction. The computed frequencies are based on the periodic fluctuations of the stream function on the centerline just downstream of the shedder. The frequency was averaged over about five cycles, after allowing the fluctuations to reach a state of approximately constant frequency and amplitude.

The computations of the flow for the vortex meter incorporating a circular cross-section shedder were performed, using the computation grid shown in figure 1. Figure 2 presents a plot of computed instantaneous stream function, 0.055 pipe diameters downstream of the rear face of the shedder, against dimensionless time (T=tU/D) at a Reynolds number (Re = Ud/v) of 9125.

The computed Strouhal numbers (St=fd/U) for various Reynolds numbers are shown together with experimental values in figure 3. For a Reynolds number of 9125, the stream function at T = 10.18 is shown in figure 4. The flow is seen to separate from the bluff body, forming a corrugated wake downstream. This can be seen more clearly in figure 5, which shows the corresponding vorticity contours. There is evidence that a thin contact line is formed between successive vortices, which is the consequence of the entrainment of fluid from one side of the centerline meeting the fluid from the other side. The flow around the rectangular cross-section shedder inside the vortex meter was computed using the computation grid shown in figure 6. The variation of the stream function 0.137 pipe diameters downstream of the rear face of the shedder is shown in figure 7. It is quite clear that the stream function oscillation for this shedder, like that for the circular one, rapidly reaches a reasonably constant amplitude and frequency. The computed Strouhal numbers of various Reynolds numbers are shown, together with the experimental values, in figure 8. For a Reynolds number of 9125, the flow at dimensionless time 11.62 is shown in figure 9 as a stream function plot, and in figure 10 as vorticity contours. In figure 9, the vortices seem to be swept along the rear face of the

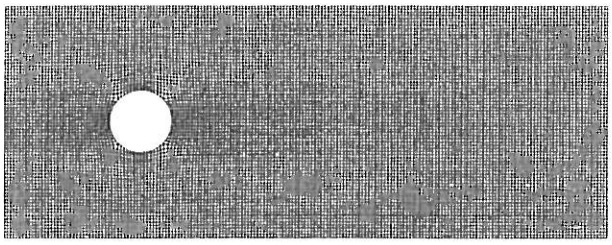


Fig. 1. Computation grid for circular shedder.

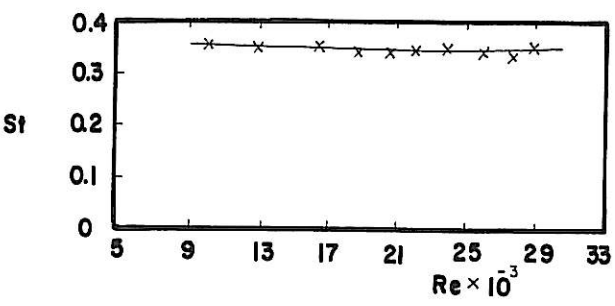


Fig. 3. Strouhal number versus Reynolds number for circular shedder (electrode on splitter plate): x, test meter data; __ , theoretical data.

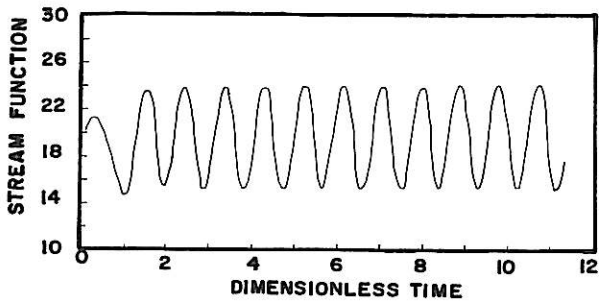


Fig. 2. Instantaneous stream function 0.055 diameters downstream of circular shedder (Re = 912.5).

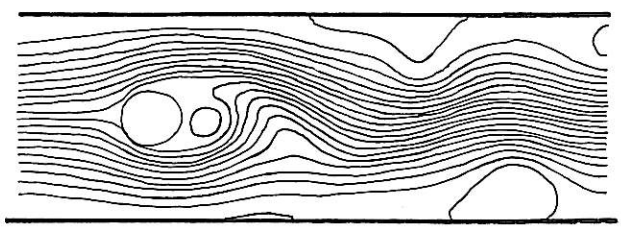


Fig. 4. Flow past circular shedder at T = 10.18 (Re = 9125).

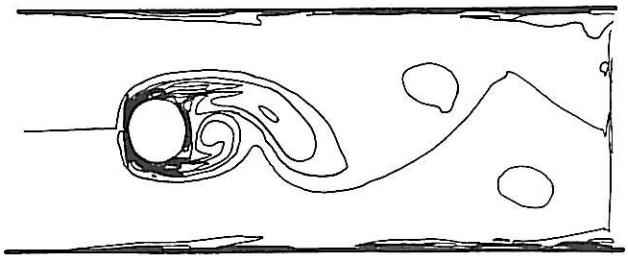


Fig. 5. Vorticity contours for circular shedder.

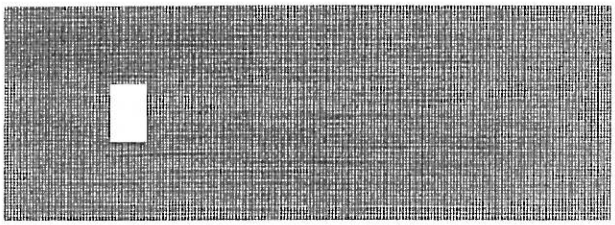


Fig. 6. Computation grid for rectangular shedder.

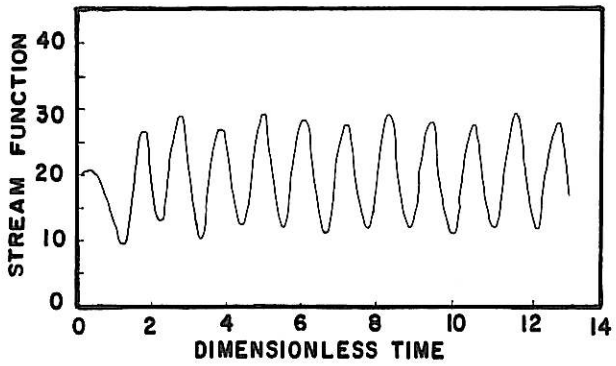


Fig. 7. Instantaneous stream function 0.137 diameters downstream of rectangular shedder (Re = 9124).

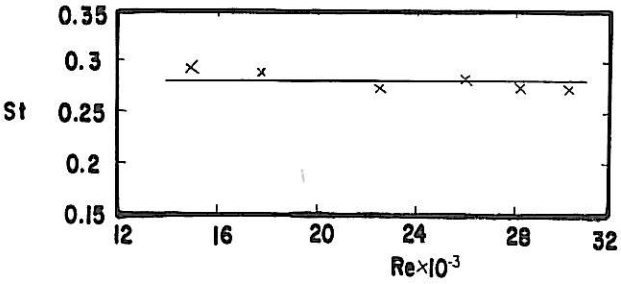


Fig. 8. Strouhal number versus Reynolds number for rectangular shedder (electrode on front face of shedder): x, test meter data ___, theoretical data.

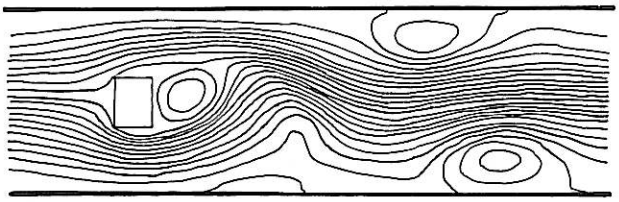


Fig. 9. Flow past rectangular shedder at T = 11.62 (Re = 9125).

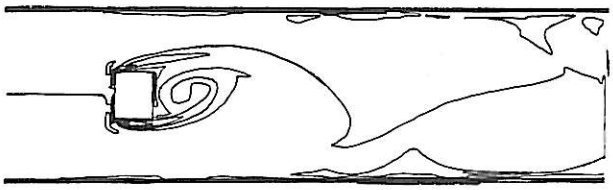


Fig. 10. Vorticity contours for rectangular shedder.

shedder, which is consistent with the other results (see Cousins et al[14]) indicating that the rectangular shedder with L/d close to 0.6 can produce such action, reinforcing the vortex shedding. The vorticity plot (Fig. 10) shows a tendency of the boundary layer to separate from the sharp leading corners of the shedder, and some evidence of reverse flow towards the body surface that is induced by the primary vortices. This plot also shows that small vortices form at both sides of the front face of the shedder. The growth of these vortices was seen to alternate and coincide with the alternating shedding of the primary vortices. These vortices are perhaps responsible for the modulation of the streaming current collected by the electrode attached to the front face of the shedder inside the electrostatic vortex meter [15].

The computation grid (Fig. 11) was used for the calculation of the flow in the vortex meter incorporating a trapezoidal cross-section shedder. The stream function was monitored 0.11 pipe diameters downstream of the rear face of the shedder and its fluctuation is shown (Fig. 12) in which regular vortex shedding is rapidly achieved. The Strouhal number was calculated for a set of Reynolds numbers, which are shown together with the experimental data (Fig. 13). The stream function for a Reynolds number of 9125 is shown in figure 14 at T = 13.0. The corresponding contour of vorticity is shown in figure 15. In this figure, it is quite clear that the vortices do not disappear after their detachment from a teardrop to a more or less circular shape. This action was not apparent for the circular and rectangular cross – section shedders (Figs 5 and 10).

The flow around the triangular cross-section shedder in the vortex meter was calculated using the computation grid shown (Fig. 16). Figure 17 shows the fluctuations of the stream function 0.068 pipe diameters downstream of the bluff body trailing edge. It is clear that, unlike the stream function fluctuations for the previous shedders, the present one exhibits a rather long time to achieve steady state vortex

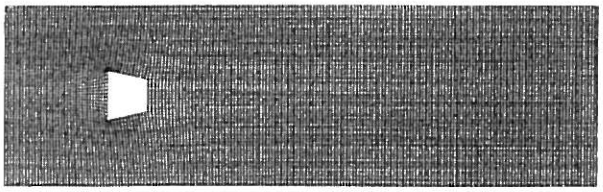


Fig. 11. Computation grid for trapezoidal shedder.

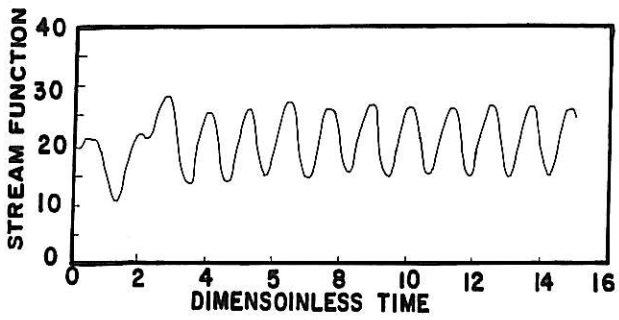


Fig. 12. Instantaneous stream function 0.11 diameters downstream of trapezoidal shedder (Re = 9125).

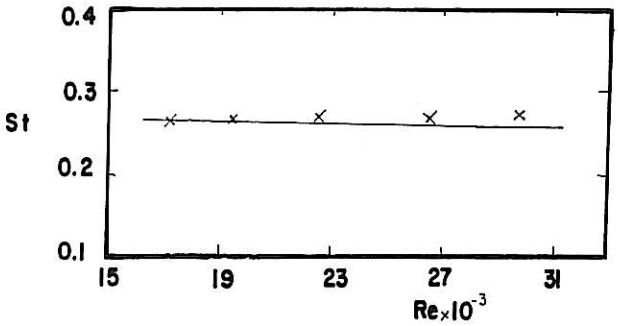


Fig. 13. Strouhal number versus Reynolds number for trapezoidal shedder (electrode on front face of shedder): x, test meter data; __, theoretical data.

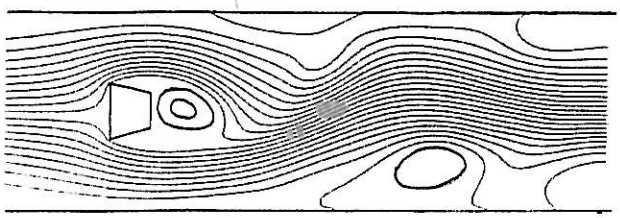


Fig. 14. Flow past trapezoidal shedder at T = 13.0 (Re = 9125).

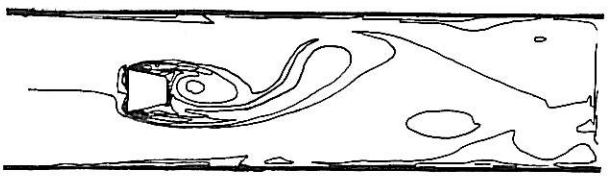


Fig. 15. Vorticity contours for trapezoidal shedder.

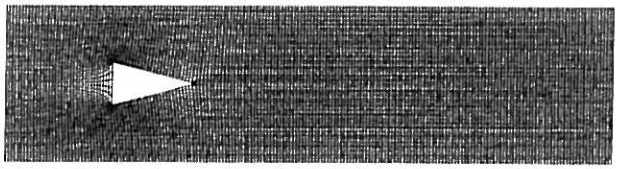


Fig. 16. Computation grid for triangular shedder.

shedding. However, the computed Strouhal numbers (in the regular fluctuation region) for various Reynolds numbers are shown together with experimental values (Fig. 18). It is interesting to monitor the evolution of the flow in the early stages of the calculation. Figure 19 shows illustrative plots for a Reynolds number of 9125. It is clear that at T = 0.16 (Fig. 19a), the flow is approximately symmetrical and in contact with the bluff body sidewalls. The subsequent plot (T = 0.72) reveals the breakup of the symmetrical state when the top recalculation zone moves downward, displacing the bottom recalculation zone. In this figure, it is clear that the vortices are irregular and this may coincide with the large amplitude fluctuations in stream function occurring during the early stages of vortex shedding (Fig. 17). Once the steady-state shedding is reached, the vortices become more regular, like those shown in figure 19c for T = 6.28. The corresponding vorticity contour is shown (Fig. 20).

The flow around a T-shaped shedder in the vortex meter was calculated using the computation grid shown (Fig. 21). Figure 22 shows the fluctuations of the stream function 0.055 pipe diameters downstream of the bluff body trailing edge. Again, the regular fluctuations are rapidly achieved. The Strouhal numbers computed for various Reynolds numbers are shown together with experimental values (Fig. 23).

The stream function at dimensionless time 15.12, for a Reynolds number of 9125, is shown (Fig. 24). Also, the corresponding vorticity contour is shown (Fig. 25). This figure shows that the vortices are larger than those shed by the previous shedders. This may concur with the early finding [16] that the inclusion of a splitter plate into the wake flow from a bluff body renders the separated shear layers thicker and more diffuse. This may highlight the importance of the shedder shape in producing strong vortices, whilst also improving the linearity and the rangeability of the meter incorporating it. This is also in agreement

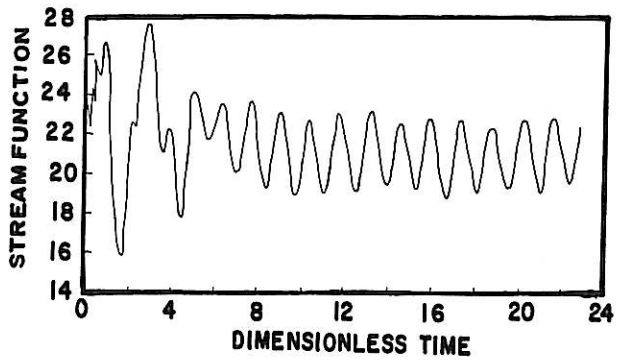


Fig. 17. Instantaneous stream function 0.068 diameters downstream of triangular shedder (Re = 9125).

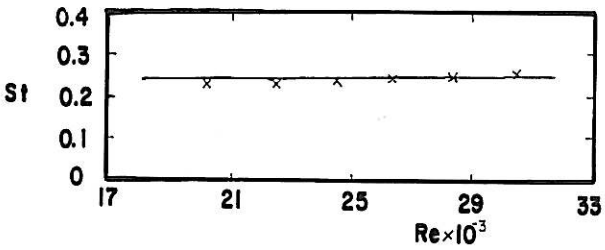


Fig. 18. Strouhal number versus Reynolds number for triangular shedder (electrode on front face of shedder): x, test meter data; __, theoretical data.

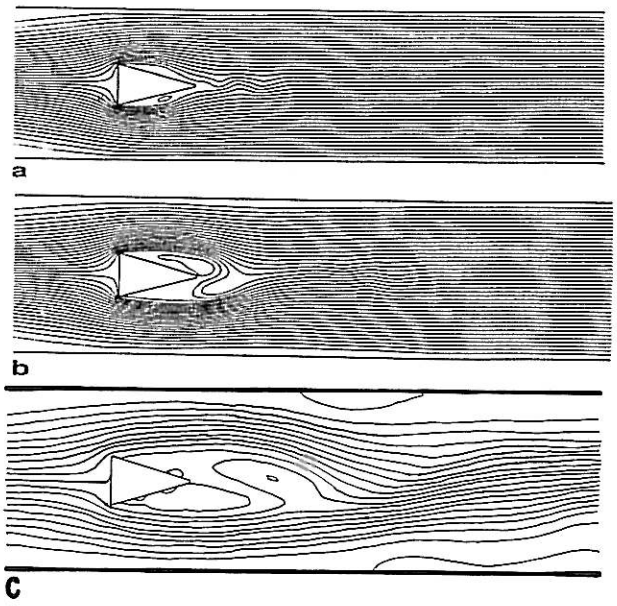


Fig. 19. Flow past triangular shedder (Re = 9125): (a) T = 0.16; (b) T = 0.72; (c) T = 6.28.

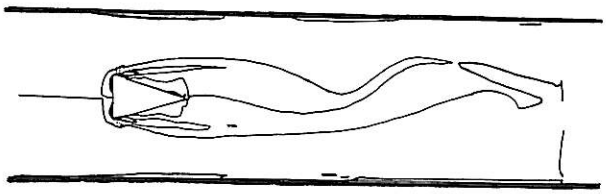


Fig. 20. Vorticity contours for triangular shedder.

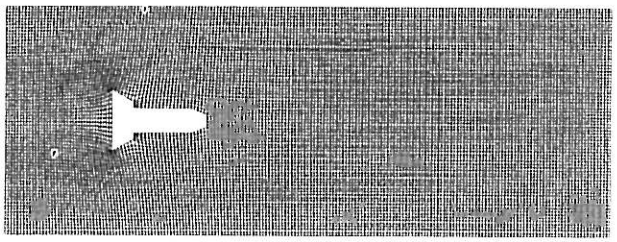


Fig. 21. Comutation grid for T-shaped shedder.

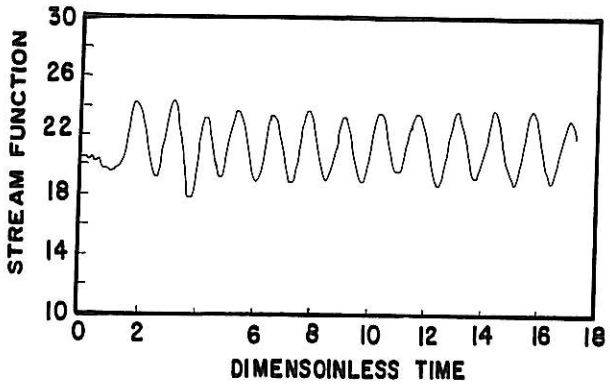


Fig. 22. Instantaneous stream function 0.055 diameters downstream of T-shaped shedder (Re = 9125).

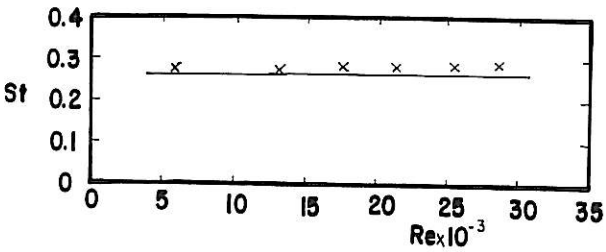


Fig. 23. Strouhal number versus Reynolds number for T-shaped shedder (electrode on front face of shedder): x, test meter data; __, theoretical data.

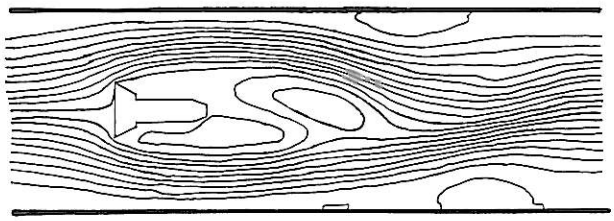


Fig. 24. Flow past T-shaped shedder at T = 15.12 (Re = 9125).

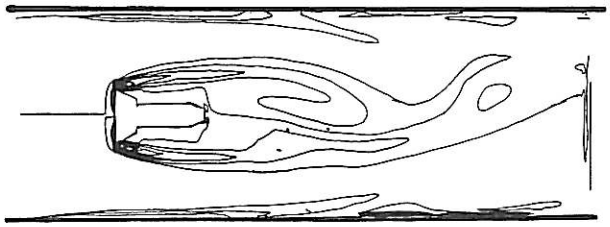


Fig. 25. Vorticity contours for T-shaped shedder.

with the experimental results[13] in which the meter using the T-shaped shedder produced the best signal quality and best meter performance.

For all of the shedders tested, the results indicate that the vortices are concentrated at the centerline of the meter body downstream of the shedder. This may explain the good signal collected by a sensor mounted in this region.

The stream function and vorticity plots reveal that mobile recalculation zones are noticeable on the sidewalls. These wall vortices are formed alternately immediately before the primary vortices collapse. In particular, the pressure at the sidewall decreases to a minimum at a point opposite to the center of the main vortex shed from the bluff body and the pressure downstream of this point increases again. The adverse pressure action seems to encourage the wall vortex to form. This action was noticed experimentally[17] and numerically[6] when this phenomenon was related to the effects of Reynolds number and the blockage ratio d/D. This may explain the rather unexpected performance of the electrode attached to the inner wall of the electrostatic vortex meter downstream of the shedder. Finally, the computed Strouhal numbers compare very well with the experimental data. This may suggest that the computer code together with the turbulence model performed satisfactorily and so can be applied successfully for modeling the unsteady phenomena in other meter types such as the fluidic meter.

CONCLUSIONS

The computer simulation described in this paper was performed in order to examine the flow past the shedder inside a vortex meter. The main points are summarized below:

1. The computed Strouhal numbers are in good agreement with those acquired experimentally. This suggests that the original laminar computer code was successfully extended to handle flow by the addition of the Baldwi-Lomax turbulence model. Accordingly, this model is suitable for modeling separated flows with large recalculation action.

2. The results indicate how the shedder shape can influence the strength of the shed vortices. Among the shedders assessed in this study, the T-shaped shedder produced the largest vortices. This agrees with experimental results in which vortex meters incorporating this shedder gave the best signal quality.

3. There is some indication that small vortices are formed at both sides of the front face of the shedder. These vortices are formed alternately and they are perhaps responsible for the modulation of the steaming current that is collected by the electrode attached to the front face of the shedder inside the electrostatic vortex meter.

4. The vortices seem to be concentrated near the centerline of the meter body behind the shedder. This may explain the good signal collected by a sensor placed in this region.

5. The wall vortices were clearly nearly noticeable in all of the computed flows. These were formed as a result of the adverse pressure gradient on the wall, which is induced by the primary vortices seed from the bluff body. These vortices may also modulate the streaming current collected by the electrode attached to the inner wall of the electrostatic meter.

REFERENCES

[1] Yeh,T. T., Robertson, B. and Mattar, W.M,1983. LDV measurements near a vortex shedding strutcture mounted in a pipe. *J. Fluid Eng., ASME* **105** 185-196.

[2] Nakatani, N., Nishikawa, T., Yoneda, Y. and Yamada, T. 1978. The flow analysis of the vortex shedding flowmeter by the Doppler velocimetery . *Proc . IMEKO, Symp. On Flow Meas.* And *Control in Ind'*. Tokyo 103-108.

[3] Mattingly, G. E.,1985 Prospects for improvements in fluid metering via new esearch tools. *Inter. Conf. On Flow Meas. IMEKO*, Melbourne 1-14.

[4] Fromm, J. E. and Harlow, F. H., 1963. Numerical

solution of the problem of vortex street development. *Phys. Fluid*, **6**, 1976, 975-982.

[5] Jam, P.C. and God, B. S., 1976. Shedding of vortices behind a circular cylinder. *Comput. Fluids,* **4** 137-142.

[6] Davis, R. W., Moore, E. F. and Purtell, L. P. 1984. A numerical experimental study of confined flow around rectangular cylinders. *Phys. Fluids*, **27** (1) 46-59.

[7] Park, j.K., Park, S. O. and Hyun, j. M., Flow regimes of unsteady laminar flow past a slender elliptic cylinder at incidence. *Int. j. Heat Fluid Flow*, **10** (4) 311-317.

[8] Johnson, M. W. 1990. Computation of flow in a vortex-shedding flowmeter. *Flow Meas. Instrum.* **1**(4) 201-208.

[9] Boussinesq, J., 1877. Theorie de l'ecoulement tourbillant. *Mem. Pre. Par.div. Sav.* **23**, Paris.

[10] Prandtl, L., 1925. Bericht uber Untersuchungen zur ausgebildeten Turbulenz. *ZAMM*,**5** (1925), 136. 136.

[11] Cebeci, T. and Smith, A., 1974. *Analysis of Turbulent Boundary Layers* Academic Press, New York.

[12] Baldwin, B. and Lomax, H., 1978. Thin-layer approximation and algebraic model for separated turbulent flows. *AIAA* Paper 78-257 1-8.

[13] El Wahed, A. K., 1991. Electrostatic streaming current and its application to the vortex shedding meter. PhD Thesis, University of Liverpool (1991).

[14] Cousins, T., Foster, S. A. and Johnson, P. A.,1973. A linear and accurate flowmeter using vortex shedding. Inst. Meas. And Control Symp. On Power Fluids for Process Control (1973) 45-56.

[15] Sproston, J. L., El Wahed, A. K. and Johnson, M. W. An electrostatic vortex shedding meter. *Flow Meas. Instrum.* **1**(4) 183-190.

[16] Lucas, G. P. and Turner, j. T., 1985. Influence of cylinder goemetry on the quality of its vortex shedding signal. *Inter Conf. On Flow Meas., IMEKO*, Melbourne (1975) 81-88.

[17] Nagata, H., Kakehi, Y., Tsunekawa, M. and Hasegawa, T., 1975. Unsteady flow past a circular cylinder stared impulsively. *Bull. JSME* **18** (123) 992-1001.

Petroleum Res. J. Vol. 16 (2004); P. 11–20, 3 Figs.

Overview of Three-Phase Relative Permeability Experimental Data

Mabruk A. Benrewin*

مراجعة للمعلومات العملية للنفاذية النسبية ذات الأطوار الثلاثة

المبروك أحمد بن روين

تتطلب دراسات محاكاة أو تقييم المكامن النفطية معلومات للنفاذية النسبية ذات الأطوار الثلاثة التي يمكن الحصول عليها من القياسات المعملية أو بواسطة النماذج النظرية، وترجع بداية الدراسات المعملية إلى عام 1941 إلا أن الصعوبات الفنية التي واجهت معظم البحاث في قياسات النفاذية النسبية أدت إلى ندرة المعلومات في هذا المجال. وتقدم هذه الورقة مراجعة لمعظم نتائج التجارب التي تم نشرها وملخصاً لأهم الإستنتاجات التي تم التوصل إليها حتى تاريخ إعدادها.

Abstract: *Three-phase relative permeability data are required to run reservoir simulation studies or to evaluate reservoir performance. These data can be obtained from laboratory measurements or by theoretical models. Experimental studies have been carried out since 1941. The difficulties observed during the experimental procedures and calculations have limited the work conducted in this area. Only scattered amounts of published data are available in this subject.*

This paper gives an overview on the work done on experimental three phase relative permeability data, which presented in chronological order for the subject along with the main conclusions.

INTRODUCTION

Leverett and Lewis[1] were the first to publish results for three-phase relative permeability in unconsolidated sandstones in 1941. Unfortunately, only few experimental studies have been reported in the literature. Table 1 summarizes, in chronological order, most of the experiments results reported to date. In this brief ovreview, the main conclusions of the experimental results are presented.

* Al-Fateh University, Faculty of Engineering, Petroleum Engineering Dept. Tripoli, Libya.

THREE-PHASE WATER RELATIVE PERMEABILITY

Several investigators[1,3,8,9,11,12,13,18] reported that in water-wet systems, the three-phase relative permeability to water depends mainly on the water saturation and the effect of saturation history on the water relative permeability is insignificant. Accordingly, two and three-phase water relative permeability are approximately the same at the same water saturation. Others[2,4,5,7,10] have found that three-phase water relative permeability is not just a function of it's own saturation but is dependent upon the saturation of all three phases.

Water isoperms, as reported by many investigators, are shown in figure 1. Water isoperms are either linear or concave toward 100% water apex. Linear isoperms indicate that the water relative permeability is a function of its own saturation while the concave water isoperms indicate higher water relative permeability when both gas and oil are present than in the presence of gas and oil alone. Linear isoperms are more likely to represent the water isoperms because water relative permeability does not depend on the saturation history in water-wet systems.

THREE-PHASE GAS RELATIVE PERMEABILITY

Leverett and Lewis[1] reported that the three-phase gas relative permeability is slightly less than

Table 1. Chronological listing of three-phase relative permeability experiments

Ref #	Date	Authors	Rock Propertis				Exp. type	Saturation Measures	Treat of	Treat of	Kr function			Isoperms		
			Rock type	Porosity %	k,mD	Wettability	Dynamic ss	Resistiviy	Hysteresi	End effect	Krw	Kro	Krg	Water	Oil	Gas
1	1941	Leveret	Uncons ss	42	5000-16000	...	Dynamic ss	Resistiviy	Ignored	Neglected	Sw	Sw,So,Sg	Sw,So,Sg	Linear	Concave	Convex
2	1951	Caudle	Cons ss	23	35	oil	Steady state	Vacum distill	Ignored	Neglected	Sw,So,Sg	Sw,So,Sg	Sw,So,Sg	Concave	Concave	Convex
3	1956	Corey et al	Berea ss	....	...	water	Steady state	Gravity	Diff Cores	Diaphragm	Sw	Sw,So,Sg	Sg	.....	Concave	Linear
4	1956	Reid	Uncons ss	35	3100	...	Steady state	Resist-Gama	Ignored	Mid cores	Sw,So,Sg	Sw,So,Sg	Sw,So,Sg	Concave	Convex	Concave
5	1962	Snell	Uncons ss	35	7100	water	Steady state	Rcl+Neutron	Revaluated	Mid cores	Sw,So,Sg	Sw,So,Sg	Sw,So,Sg	Concave	Convex	Convex
6	1966	Sarem	Berea ss	20	275	water	Unsteady	Volumetric	Ignored	Neglected	Sw	....	Sg	Linear	Linear	Linear
7	1966	Donald	Berea ss,ls	19-20	42.4-	water	Unsteady	Volumetric	Ignored	High rates	Sw,So,Sg	Sw,So,Sg	Sw,So,Sg	Concave	Concave	Convex
8	1967	Saraf	Boise ss	26	1450	water	Steady state	NMR	Diff Cores	Mid cores	Sw	Sw,So,Sg	Sg	...	Convex	Linear
9	1970	Schneinder	Torpedo ss	24	370	water	Steady state	Resist+Xray	Evaluated	Not discussed	Sw	Sw,So,Sg	Sw,So,Sg	Linear	Linear	...
10	1982	Vanspronsen	Berea ss	21.3-26	480-600	water	Steady state	Centrifuge	O/W imbib	High rates	Sw,So,Sg	Sw,So,Sg	.....	Concave	Concave	...
11	1982	Saraf et al	Berea ss	23	510-580	water	Steady state	M-balance	Not Discussed	Mid cores	Sw	Sw,So,Sg	Sg	Linear	Concave	Linear
12	1988	Oak et al	Berea ss	...	160-210	water	Steady state	X-ray	Not Discussed	Mid cores	Sw	Sw,So,Sg	Sw,So,Sg	Linear	Linear	Convex
13	1990	Oak	Berea ss	...	200-1000	water	Steady state	X-ray	Not Discussed	Not discussed	Sw	Sw,So,Sg	Sg	Linear	...	...
14	1990	Narahara	Berea ss	21.5	635-860	water-mixed	Unsteady	Centrifuge	Not Discussed	Comp-Cores	Sw	So	Sg	...	...	...
18	1990	Dria et al	Dolomite	20.2	24	water	Steady state	Tracer	Not Discussed	High rates	Sw	So	Sg	...	...	...
15	1991	Marek et al	LS	23.4	...	mixed	Steady state	Ct Scanner	Not Discussed	Not discussed	.....	...	.....	...	Convex	...
23	1993	Kalaydjian	s.s	0.16-0.196	800-2300	water	Steady state	X-ray scan	Evaluated	semi-perm	....	....	...	....	...	....
24	1993	Baker et al	s.s	....	....	various	gravity drain	....	....	....	....	So+Sw	....	....	....	....
25	1994	Skauge et al	s.s	....	....	water	gravity drain	Gamma ray	....	....	....	....	....	....	....	....
26	1995	Eleri et al	s.s	18.2-22.5	234	water	Steady state	Gamma ray	....	Scaled	Sw	....	....	....	....	....
27	1995	Naylor et al	s.s	....	....	water	Unsteady	radioactive	....	....	....	So	....	....	....	....
28	1995	Goodyear	s.s	....	....	water	Unsteady		....	....	....	....	....	....	....	....
29	1996	Vizika	Sand packs	35	10000-14000	various	gravity drain	Ct Scanner	....	....	....	....	....	....	....	....
30	1996	Nordtvedt	Chalk	0.398	2.27	water	Unsteady	Ct Scanner	....	....	....	....	....	....	....	....
31	1998	Sahni et al	Sand packs	....	....	water	gravity drain	Ct Scanner	....	....	....	....	....	....	....	....
32	2000	Di carlo	Sand packs	....	....	various	gravity drain	Ct Scanner	Evaluated	....	....	....	....	....	....	....

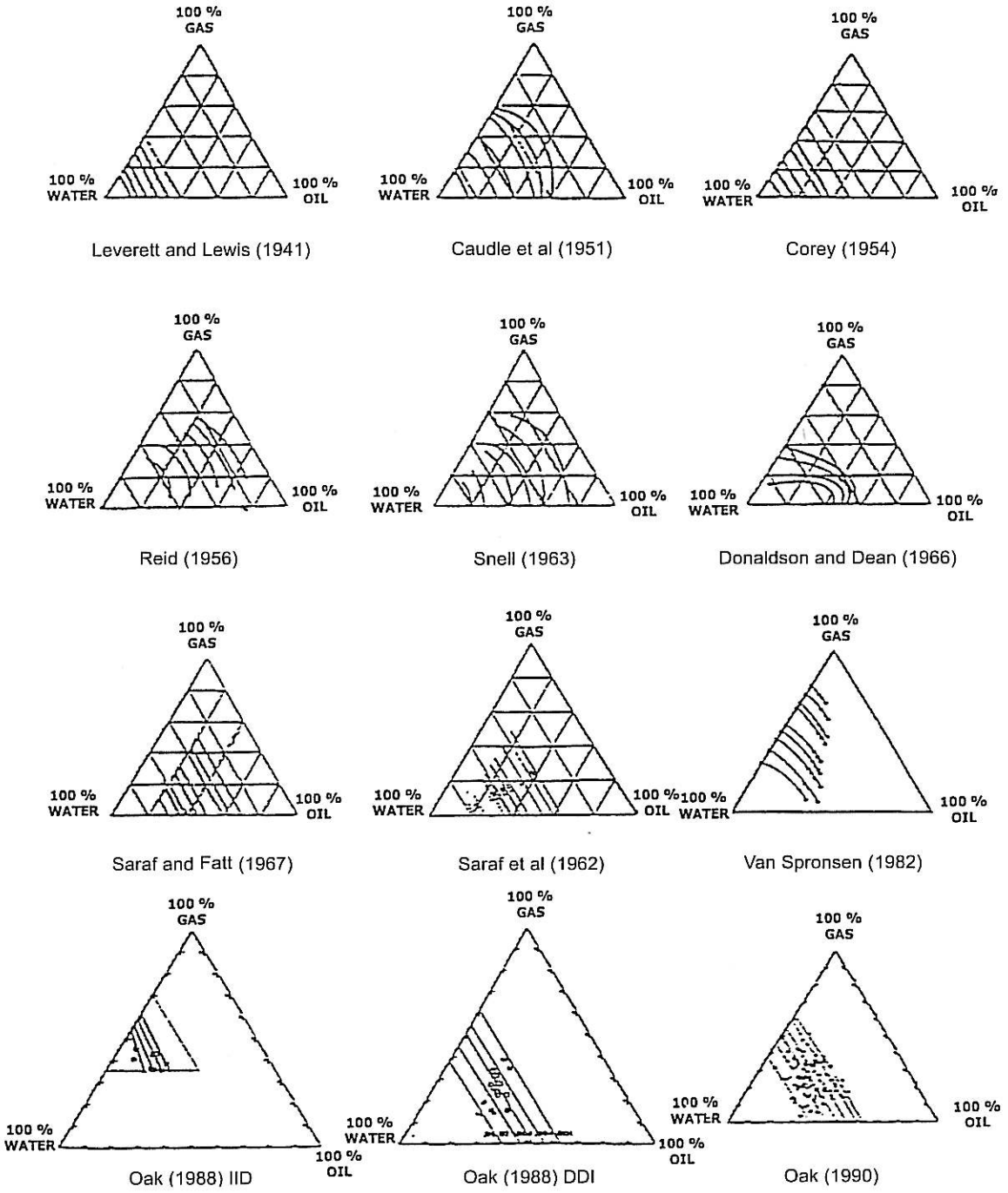


Fig. 1. A collection of water isoperms from the current literature.

what would correspond to the same gas saturation in two-phase flow. Saraf and Fatt[8] found that the three-phase gas relative permeability depends only on the total liquid saturation and is independent of oil and water saturations taken individually. Some investigators[3,6,14,18] found that three-phase gas relative permeability is a function of its own saturation only. Others[2,4,5,7,9] reported that gas relative permeability is dependent upon the saturation of all three phases.

Oak[13] and Saraf *et al*[11] reported that gas relative permeability depends mainly on gas saturation and saturation history of the gas phase. Both two-phase and three-phase relative permeability are approximately the same at the same saturation and saturation histories of the gas phase. Dicarlo *et al*[32] found that the gas relative permeability is smaller in an oil-wet medium than in a water-wet medium and explained their observations in terms of wetting spreading and pore scale configurations of fluids.

Gas isoperms from a variety of major studies are shown in figure 2. No definite trend can be observed because of errors associated with experimental measurements and dependence of gas relative permeability on the saturation history.

THREE-PHASE OIL RELATIVE PERMEABILITY

Leverett and Lewis[1] reported that oil relative permeability varies in a complex manner. Caudle

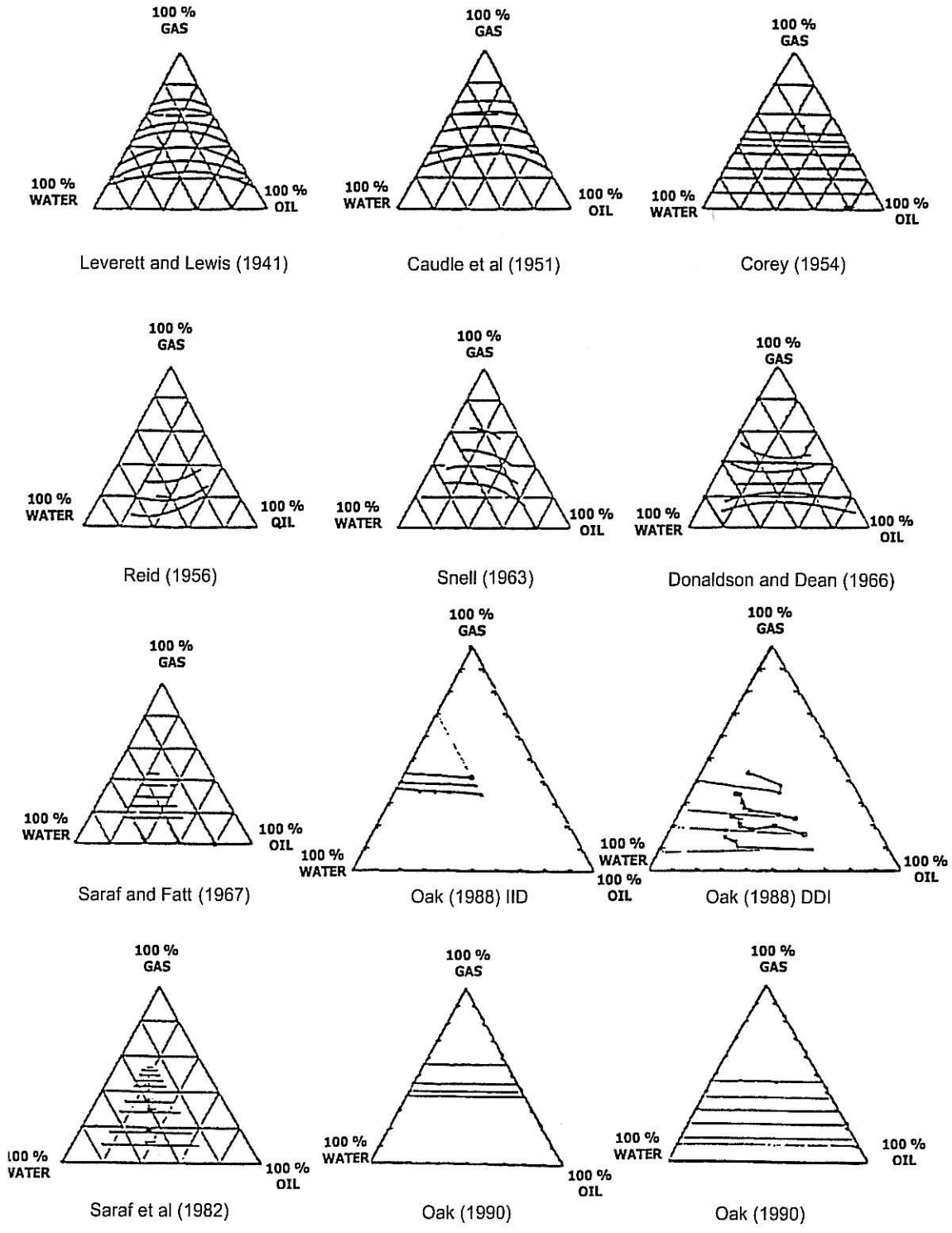


Fig. 2. A collection of gas isoperms from the current literature.

and Slobod[2] found that oil permeability is dependent on the saturation of all phases. Sarem [6] and Dria and Pope[18] found that oil relative permeability is a function of oil saturation only.

Other investigators[3,9,7,8,11,12,13] found that three-phase oil permeability varies not only with oil saturation but also with saturation of water and gas. The variation depends on saturation history.

Figure 3 shows oil isoperms from a number of studies. These results indicate that no general trend can be observed. The shape of theses isoperms are referred to as being concave or convex with respect to the 100 % oil saturation apex. More than half of the studies show a concave type of oil isoperms which indicates that, at high oil saturation, the oil permeability is higher when both gas and brine are present than in

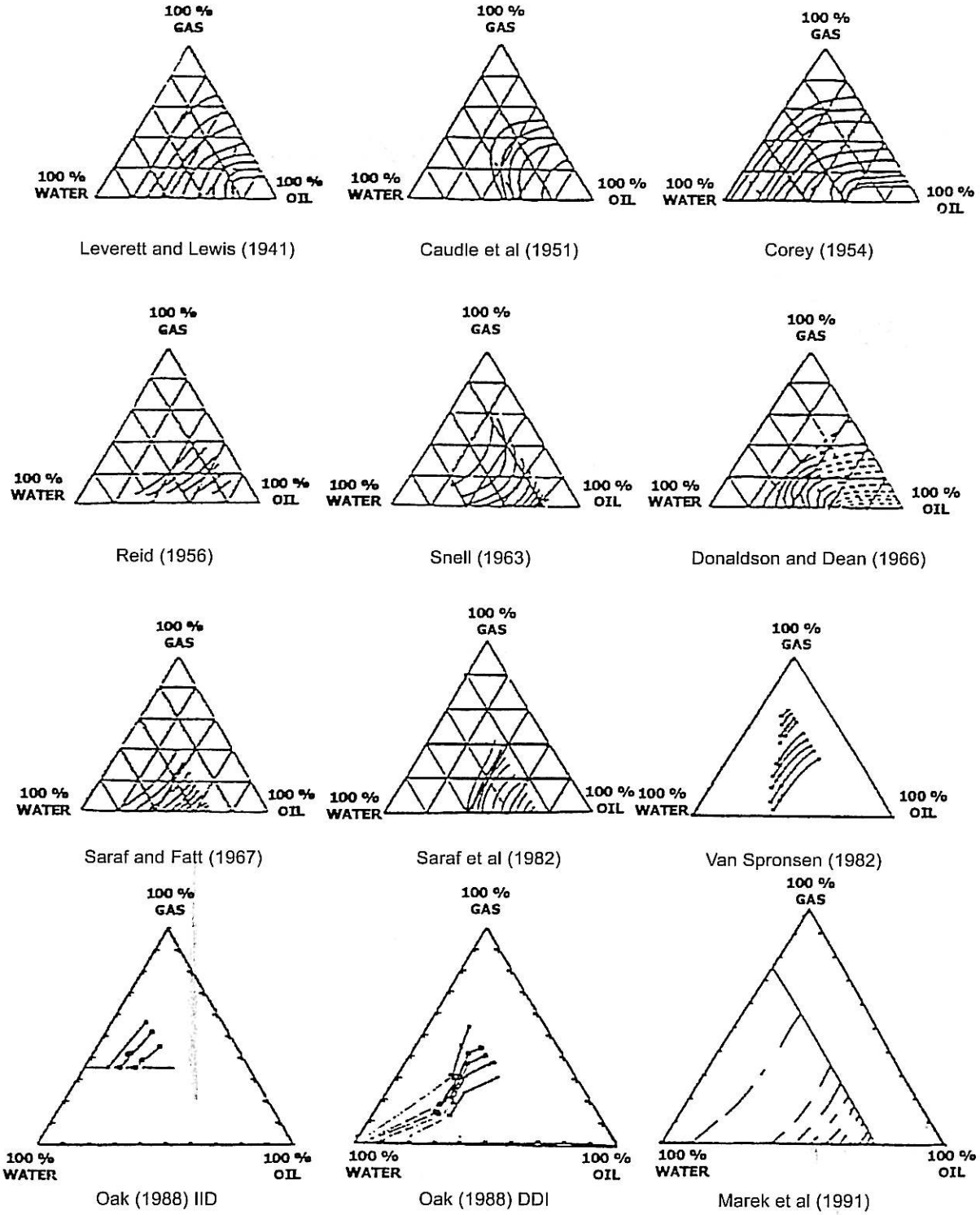


Fig. 3. A collection of oil isoperms from the current literature.

the presence of gas and brine alone. Saturation history affects the shape and the type of the oil isoperms.

Oak [13] found that more than half of the studies on the primary DDI* show convex type oil isoperms while the oil isoperms for secondary DDI and IDI are concave. Oil isoperms for unconsolidated sandstones are likely to be convex toward 100% oil apex.

FACTORS AFFECTING THREE-PHASE RELATIVE PERMEABILITY

1-Effect of Saturation History

Most experimental studies either have ignored or incompletely reported saturation history effect. Oak *et al* [12] have reported two cases of saturation histories . They found that in the primary DDI*, oil and gas relative permeability depend on three-phase saturations and in the primary IID, oil and gas relative permeability depend on their own saturation only. The water relative permeability is a function of water saturation only for both DDI and IID saturation histories.

Oak [13] studied six cases of saturation histories. He indicated that gas relative permeability depends upon the saturation history of the gas phase. The three-phase gas relative permeability was divided into two groups. In group 1, the gas saturation changes in increasing directions (drainage) as in the case of primary and secondary DDI's, DDI and IDI. In group 2, the gas saturation changes in decreasing directions, as in the case of IID, IDD, and DID. It was concluded that the effect of saturation history on the water permeability is insignificant and for gas and oil relative permeability it shows significant variations. As a result, oil and gas relative permeability varied with both their saturation and saturation histories.

2- Effect of Trapped Phases

The displacement of trapped oil by gas is a flow mechanism that occurs only in the three–phase flow system. Oak[13] postulated the following mechanism: If oil is present in a pore, the displacement by gas depends upon whether or not the oil is isolated .If oil is trapped and isolated by water, the displacement is hindered until the water trapping oil is displaced by gas .If the oil maintains continuous flow channels, the oil is immediately displaced by gas as the gas invades the same pore. Thus, the displacement of trapped oil by gas is one of the important events that result in the saturation history effect.

In the water-wet porous media, at a given oil saturation when the water saturation is high and the gas saturation is low, some oil is trapped by the water phase in dead end pores. This results in a lower oil permeability, but as the water saturation is decreased, this effect becomes less pronounced. In a predominately oil–gas system with only small amount of water present, oil (being wetting phase) is not trapped by the gas. Therefore, in the region where the water saturation is low and the gas saturation is high, oil permeability is high when compared to high water and low gas saturation eventhough the oil saturation is the same[8].

Narahara *et al*[14] found that gas-oil primary drainage relative permeability, measured with connate water present, are the same as those measured without connate water present for both water-wet and mixed-wet Berea sandstone provided that the water phase was immobile and the gas-oil relative permeability are expressed as function of total liquid saturation.

Kyte *et al*[16] and Holmgren and Morse[22] demonstrated that in the presence of a gas phase, the residual oil saturation is lower than in the absence of gas. The presence of a gas phase caused a decrease in the residual oil saturation in a water-wet media. It was believed that the ultimate residual oil saturation is trapped by water and that the gas phase, which in turn was trapped within the oil, occupied a portion of space which in the absence of gas would be occupied by oil. In the oil-wet media, the ultimate residual oil saturation is believed to be in the form of pendular rings around the contact points of the rock grains. The gas phase simply occupied space, which in the absence of gas would have been occupied by water. Hence, the trapped gas has no effect on the residual oil in oil-wet media.

Scheneider and Owens[9] found that for oil wet systems the presence of trapped gas affected only the water relative permeability because of the interference between the water and gas (non-wetting phase). Relative permeability to oil was not greatly affected by the presence of trapped gas saturation because oil is the wetting phase. For water-wet system, with trapped gas present, the highest oil

* The notations DDI, IID, and DIC are used for simplicity to describe the saturations history. The letters indicate directional saturation changes of each fluid phase, in order of water, oil and gas, either decreasing, increasing or remains constant.

relative permeability values (at high oil saturation) fell below the oil relative permeability values obtained in the absence of gas saturation (zero gas saturation). The gas phase as the non-wetting phase with respect to oil had displaced oil from some of the larger flow channels. In the case of low oil saturation, the relative permeability to oil in the absence of gas saturation was lower than in the case of trapped gas present.

Saraf *et al*[11] reported that oil relative permeability was influenced by the direction of gas saturation change. Oil relative permeability was higher at a given oil saturation when gas saturation was decreasing than when gas saturation was increasing. This means simply that the trapping gas enables oil to flow more freely, or alternatively, since they occupy similar pore space. The achievement of gas mobility occurs at the expense of oil mobility. When a core was water flooded after gas flood, a higher ultimate recovery of oil was achieved. The gas seems to release part of the trapped oil allowing it to flow before the gas itself gets trapped in place of the oil.

3- Effect of Wettability:

Most experiments have been performed on uniform water-wet systems. In recent years, some measurements have been made in oil-wet, mixed-wet and fractionally-wet systems [14,15,17,24,29,33].

Oak *et al* [12] studied three-phase relative permeability in an intermediate-wet Berea sandstone and found that the water relative permeability was a function of water saturation only for water-wet media while in oil-wet and intermediate-wet media, the water relative permeability showed some hysteresis and was a function of two saturations. It was also found that the oil relative permeability was a function of two saturations and saturation history and the gas relative permeability was a function of gas saturation and appeared to be insensitive to wettability changes.

Di carlo *et al*[32] measured oil, water and gas relative permeability during three-phase gravity drainage on oil-wet, water-wet, mixed-wet and fractionally-wet sand packs. They found that under uniform wetting, the relative permeability of the most-wetting phase (water in a water-wet pack and oil in oil-wet pack) are similar. They also found that the relative permeability of intermediate-wet phase (oil in water-wet pack) are very different at low saturations. They observed that the gas relative permeability is smaller in oil-wet medium than in a water-wet medium at the same gas saturation.

4-Effect of Spreading:

The spreading coefficient of oil in water in presence of gas, denoted by S, is defined as:

$$S = \gamma_{wg} - (\gamma_{wo} - \gamma_{og})$$

Where γ = represents the interfacial tension between the phases.

When S is positive, the oil tends to form spreading films on the water subtrates thus favoring the hydraulic continuity of the oleic phase and leads to very low residual oil saturation. Kalaydjian *et al*[23] showed that both oil and gas relative permeability are lower under negative than under positive spreading conditions.

Vizika and Lombard[29] concluded that in water-wet and mixed-wet porous media oil relative permeability are higher for positive spreading conditions than for negative spreading conditions. In water-wet porous media, both oil and gas relative permeability are lower in the case of non-spreading and for low oil saturation. In oil-wet porous media, the same oil and gas relative permeability are obtained for both spreading and non-spreading cases.

LABORATORY CONDITIONS

Most of the experimens were carried out to improve the measurement techniques. The techniques used for measuring the relative permeability data ranged from resistivity measurement of fluid saturation to up -to-date technology of X-ray Computed Tomography (CT) scanning.

Most of the experiments were run under steady-state conditions and few were run under unsteady-state conditions. Steady-state methods proved to have broadest applicability and flexibility in controlling changes in the saturation of each of the three fluid phases in the system[9]. However, Unsteady-state methods are possibly the simplest and quickest methods of obtaining three–phase relative permeability data[6]. Steady-state three-phase relative permeability to both water and oil are similar to those obtained by unsteady-state methods. Schneider and Owens[9] found that steady state gas relative permeability are lower compared to unsteady-state values for increasing gas saturation, whereas the reverse is true for decreasing gas saturation (this may be related to the trapping of different amounts of gas in the two process).

Eleri *et al*[26] showed that more hysteresis is observed in the unsteady-state relative permeability curves than in the steady-state relative permeability curves. They also indicated that the unsteady-state relative permeability curves observed more oil-wet conditions than the steady-state relative permeability curves.

Berea sandstone has been used extensively in the experiments. The rock properties of the Berea sandstone are close in porosity values but not in absolute permeability values. Water-wet conditions are always considered for Berea sandstone. Few studies were conducted in carbonate rocks[15,18,23].

Air and N_2 are the most common gases used to represent the gas phase in three-phase relative permeability measurements because of their low interaction with other fluids. Dria and Pope [(18] showed that there are significant differences in results between the three-phase relative permeability measured when the gas is CO_2 and when the gas is N_2 or Air. All the experiments used refined hydrocarbon liquids and brine solutions to represent both the oil phase and the water phase. Eleri *et al* [26] concluded that extensive flushing of a restored core with refined oil may lead to a non- representative relative permeability data and should be, therefore, avoided. Use of ideal clean fluids rather than reservoir fluids may put some limitation on the use of experimental data to represent the reservoir conditions.

Experimental errors were reported in many experiments. Most of the errors are attributed to lack of consideration of the capillary end effect and hysteresis effect. Measurement of the data is always a problem, and most of the experimental work was targeted to improve the techniques of measurement rather than to study the phenomena of three -phase flow. The work of Leverett and Lewis [1] did not take into consideration the capillary end effect and hysteresis. Errors were also reported due to dead space in the cell and failure to reach equilibrium. Their work was considered incomplete.

Caudle and Slobod[2] used vacuum distillation for determining fluid saturations. This technique is very lengthy and time consuming. The authors described their work as incomplete. Fayers and Matthew[17] considered the results of Corey *et al*[3] incorrect because of uncertainties associated with non-uniform trapped water and the limited number of consistent results. There were possible errors in oil and gas saturation measurement when using Gamma-ray absorption due to differential absorption of Gamma rays by the oil and water phases.

The method proposed by Sarem[6] is simple and comparatively fast, but the assumptions that all relative permeability depend only on their saturations seem to be unrealistic and also neglecting capillary effect is a weak assumption.

Oak[13] reported that no data can be collected for high gas saturation because of an experimental limitation on the maximum gas injection rate.

All the experiments were run under different conditions and different measurement techniques in such a way that it becomes difficult to compare the results. A general standard of experimental procedures has not been set by the oil industry in order to make the studies of the three-phase relative permeability more compatible.

CONCLUSIONS

Based on this overview of the experimental work on three-phase relative permeability data, the following conclusions can be drawn:

1- Analysis of the experimental results indicates that there is no agreement on the qualitative or quantitative results obtained from the experiments. The discrepancy may be due to the different types of measurement techniques, different saturation histories, neglect of capillary end effect and hysteresis effect, and other experimental conditions.

2- The majority of the experiments in water-wet systems agree on the following points.
   a- The three–phase water relative permeability depends on its saturation and does not depend on the saturation history.
   b- The three-phase oil relative permeability behaves in a complex manner. It depends not only on its saturation but also in the other phase's saturation and on the saturation history.
   c- The three-phase gas relative permeability depends on the oil, gas, and water saturation and may depend on the saturation history.

3- There are insufficient data for oil-wet systems. It is difficult to determine whether the oil, gas and water isoperms are significantly different from isoperms of water wet systems.

4- The effect of trapped oil and trapped gas on relative permeability has not been resolved.

5- Lack of experimental data have been reported for three-phase oil permeability at low oil saturation and for three-phase gas permeability at high gas saturation

6- More attention should be given to the saturation history for three-phase relative permeability studies. It is concluded from the latest experimental work that saturation history has an effect on the results of the relative permeability.

7- The complexity of experimental and calculation procedures for the three-phase relative permeability are primary reasons why published data in this area are limited.

REFERENCES

[1] Leverett, M.C and Lewis,W.B; 1941. Steady flow of gas-oil-water mixtures through unconsolidated sands. *Trans. AIME* **142**.107-16.

[2] Caudle.B.H, Slobod.R.L 1951. Further development in the laboratory determination of relative permeability, *Trans.AIME* **192**, 145-50.

[3] Corey, A.T.,Rathjens, C.H., Henderson, J.H., Wyllie, M.R., 1956. Three-phase relative permeability. *Trans.AIME* **207**.349-51.

[4] Reid.S., 1956. The *Flow of Three Immiscible Fluids in Porous Media*. PhD Dissertation, Univ. of Brinigham UK.

[5] Snell, R.W., 1963. The saturation history dependence of three-phase oil relative permeability. *J. Ins.Pet*, March, **49**, 81-84.

[6] Sarem, A.M., 1966. Three-phase relative permeability measurement by unsteady-state method. *SPEJ.* Sep. 1966, 199-205: Trans AIME 237.

[7] Donaldson,E.C and Dean, G.W, 1966. Two-and three-phase relative permeability studies. RI6826, USBM.

[8] Saraf, D.N. and Fatt, I., 1967. Three-phase relative permeability measurment using a nuclear. magnetic resonance technique for estimating fluid saturations. *SPEJ, Trans AIME* **240**, 235-42.

[9] Schneider, F.N., and Owens, W.W., 1970. Sandstone and carbonate two and three-phase relative permeability characteristics. *Soc.Pet.Eng.J.* Trans *AIME* **249**, 75-184

[10] Van Spronsen. E.,1982. Three-phase relative permeability measurements using the centrifuge method. paper SPE10688 presented at the 1982 SPE/ DOE Symposium on Enhanced Oil Recovery, Tulsa April 4-7.

[11] Saraf. D.N., Botyk, JP., Jackson, C.H., Fisher, D.B., 1982. An experimental investigation of three- phase flow of water/oil/gas mixtures through water wet sandstones. Paper SPE 10761 presented at the 1982 SPE California Regional Meeting, San Francisco, March 24-26.

[12] Oak M.J., Baker. L.E and Thomas, D.C. 1988. Three-phase relative permeability of Berea Sandstone. Paper SPE 17370 presented at the SPE/DOE Enhanced Oil Recovery Symposium, Tulsa, Oklahoma, April 17-20, 1988.

[13] Oak. M.J., 1990. Three-phase relative permeability of water-wet Berea sandstone. Paper SPE/DOE 20183 presented at the Seventh Symposium on Enhanced Oil Recovery, Tulsa Oklahoma, April 22- 25 1990.

[14] Narahara,G.M., Pozzi,A.L. and Blackshear Jr,T.H., 1990. Effect of connate water on gas/oil relative permeability for water-wet and mixed-wet Berea Rock.. Paper SPE 20503 presented at the 65th Annual Technical Conference and Exhibition, New Orleans, LA, Sept 23-26,1990.

[15] Marek, B.F, Hartman, K.J, McDonald, A.E.,1991. Three-phase relative of limestone having bimodel pore-size distribution. Paper SPE 21374 Presented at the SPE Middle East Show, Bahrain, November 16-19, 1991.

[16] Kyte, J.R., Stanclift, R.J.,Stephan.S.C, and Raport, L.A., 1956. Mecahanism of water flooding in the prescence of free gas. *Trans, AIME* **207**,215-221.

[17] Fayers .F.j, Mathews,J.D., 1984. Evaluation of normalized stones methods for estimating three-phase relative permeabilities. *Soc.Pet.Eng.J* April **24**, 225-232.

[18] Dria, D.E. and Pope, G.A. 1990. The three-phase gas/ oil/brine relative permeabilities measured under carbon dioxide flooding conditions . Paper SPE/DOE 20184 presented at the SPE/DOE Seventh Symposium On Enhanced Oil Recovery, Tulsa, Oklahoma, April 22-25,1990.

[19] Naar,J. and Wygal , R.J. 1961. Three-phase imbibition relative permeability , *SPEJ*, Dec, 253-258.

[20] Manjnath, A. and Hanarpour, M.M.,1984. An investigation of three-phase relative permeability." Paper SPE 12915 presented at the 1984 Rocky Mountain Regional Meeting held in Casper ,Wy, May 21-23, 1984.

[21] Owens,W.W. and Archer , D.1., 1971. The effective of rock wettability on oil–water relative permeability relationships , *JPT* , July, 873-878.

[22] Holmgren ,C.R. and Morse, R.A., 1951. Effect of free gas saturation on oil recovery by water flooding. *Trans.,AIME* , **192**, 135-40.

[23] Kalaydjian, F.JM., Moulu, J.C. and Vizika, O., 1993. Three-phase flow in water-wet porous media: determination of gas/oil relative permeabilities under various spreading conditions. Paper SPE 26671 presented at the 1993 SPE Annual Technical Conference and Exhibition, Houston, 3-6 Oct.

[24] Baker, L.E , 1993. Three-phase relative permeability of water-wet, intermediate-wet, and oil-wet sandstone. *Proc.,Seventh European Improved Oil Recovery Symposium*. Moscow [1993].

[25] Skauge, A. *et al.*,1994. Influrence of connate water on oil recovery by gravity drainage. Paper SPE 27817 presented at the 1994 SPE/DOE Iimproved Oil

Recovery Symposium, Tulsa, Oklahoma, 17-20 April.

[26] Eleri, O.O,Graue, A., and Skauge, A., 1995. Steady-state and unsteady-state two-phase relative permeability hysteresis and measurement of three-phase relative permeability using imaging techniques." Paper SPE 30764 presented at the 1995, *SPE Annual Technical Conference and Exhibition*, Dallas, 22-25 october.

[27] Nylor . P. *et al.*, 1995. Gravity drainage during gas injection. *Proceedings of the Eight European Improved Oil Recovery Symposium.* Vienna , Austrtia 15-17 may.

[28] Goodyear, S.G. and Jones, P.I.R., 1995. Relative permeabilities for gravity stabilizes gas injection. *Proc Eight European Improved Oil Recovery Symposium.* Vienna , Austrtia.

[29] Vizika, O. and Lombard, J.M.1996. Wettability and spreading: two key parameters in oil recovery with three-phase gravity drainage. *SPERE*, Feb, 54.

[30] Nordtvedt, J.E. Ebtoft, J.E, Iverson, J.E., Style, A., Urkedal, H.O., 1996. Determination of three-phase relative permeabilities from displacement experiments. Paper SPE 36683 presented at the 1996 SPE *Annual Technical Conference and Exhibition,* Denver, Colorado. 6-9 october.

[31] Sahni, A. Burger, J.E. and Blunt, M.J., 1998. Measurement of three-phase relative permeability during gravity drainag using CT scanning. Paper SPE 39665 presented at the 1998 *SPE/DOE Improved Oil Recovery Symposium*, Tulsa , Oklahoma 19-22 April.

[32] Dicarlo, D.A., Sahni, A. and Blunt, M.j., 2000. Three-phase relative permeability of water-wet, oil-wet and mixed-wet sandpack. *SPEJ* March, 82.

[33] Zhou, D. and Blunt, M.J., 1998. Wettability effects in three-phase gravity drainage. *J.Pet.Sci. Eng.* **20**, 203.

Petroleum Res. J. Vol. 16 (2004); P. 21–36, 20 Figs.

A New Technique for Converting Acid Core Data to Field Application

Nehad ELhemmali* and Mohamed Nasr**

طريقة جديدة لتحويل نتائج تحميض العينات اللبية لتطبيقها عملياً

نهاد الهمالي ومحمد نصر

تعتبر عملية تحميض نسيج الصخر من أكثر عمليات تنشيط الآبار شيوعاً وتستخدم لتحسين النفاذية الأصلية للمكامن الكربونية. تستهدف المعالجة باستخدام الحامض إزالة التضرر في الطبقات الناجم عن عمليات الحفر والإنتاج والضخ. وخلال عملية معالجة نسيج صخور المكمن بالحمض تتكون قنوات عميقة حول قاع البئر تسمى القنوات الدودية، ولإنجاح عملية المعالجة بالحمض لابد من تحديد الحجم والتركيز الأمثلين للحمض المستخدم للحصول على أقصى تحسن في نفاذية المنطقة المعالجة.

لتحقيق أقصى تحسن في النفاذية يجب إجراء تجارب معملية لعينات لبية من الصخور الجيرية يتم من خلالها تحديد كل من الحجم والتركيز الأمثلين للحمض. وقد استخلص من خلال التجارب إمكانية الحصول على منحنى بياني لفعالية الحمض يمثل العلاقة بين حجم الحمض التراكمي لملء المسامات ونسبة التنشيط وذلك لكل مكمن يراد معالجته. وباستخدام هذا المنحنى يمكن تحديد حجم الحمض المراد ضخه داخل مسام المكمن.

تشير نتائج الدراسة إلى أن نفاذية الصخور الكربونية يمكن زيادتها بزيادة كمية الحمض المحقون للعينات الصخرية، وهذه الزيادة في النفاذية تصل إلى حد أقصى عندما تكون كمية الحمض المحقون قد وصلت إلى كميات مناسبة. أي زيادة في حجم الحمض المحقون أكثر من الحجم المثالي منه، سوف ينتج عنها تأثيراً عكسياً يؤدي إلى انخفاض في النفاذية للعينة اللبية المراد تحسين نفاذيتها. تقدم هذه الدراسة طريقة جديدة لتطبيق نتائج معالجة العينات اللبية المعملية في الحقول النفطية تحت الظروف الموجودة بالمكامن النفطية.

Abstract: *Matrix acidizing is commonly used as a well stimulation process for improving the original matrix permeability of carbonate reservoirs. Acid stimulation treatment is also used for removal of formation damage resulting from drilling, injection or production operations. In matrix acidizing, deep penetration of wormholes around the well bore is formed. For successful acid treatment it is necessary to determine the optimum acid volume and concentration needed for obtaining the maximum stimulation permeability for the treated zone.*

Experimental studies should be conducted on actual carbonate cores to estimate the optimum acid concentration and the injection volume of acid to improve the permeability of the damaged area. It was concluded that acid performance curve, which is represented by cumulative acid pore volume versus stimulation ratio could be determined experimentally for each reservoir to be treated.

This curve can be used for the determination of the required acid pore volume to be injected into the reservoir.

*Petroleum Research Centre, P.O. Box 6431, Tripoli, Libya.
**Department of Petroleum Engineering / Al Fatah University.

The results of this study indicate that there is an optimum acid volume to be injected in order to produce maximum rock stimulated permeability. Excessive injected acid volume more than the optimum value will produce an adverse effect of lowering the permeability of the stimulated core. A new correlation technique for converting acid core data to field conditions is presented in this study.

INTRODUCTION

The purpose of any stimulation technique is to increase the permeability near the wellbore for a damaged or low permeability reservoir. Acidizing increases the permeability by reacting with and removing some of the rock materials. When a well is not producing as expected, the formation may be damaged. If a production evaluation indicates the reservoir can deliver more fluid, stimulation may be needed. Typically, damage is associated with a partial plugging of the formation around the wellbore, which results in reducing the original permeability in the damaged zone. In order to restore the original production of the well, it is, therefore, necessary to remove damage or create new bypassing channels, which are called wormholes, in the damaged area. To remove damage, acid is injected into the natural porosity of the reservoir at matrix rates and at injection pressure below the matrix fracturing pressure.

Hydrochloric acid (HCl) is commonly used for acidizing carbonate reservoirs and it is also used for removing formation damage that consists of materials soluble in this type of acid. HCl acid is inexpensive, it reacts rapidly with most rock types, and the reaction by-products of the acid and rock are fairly easily removed from the wellbore and the adjacent formation.

The reaction of HCl with limestone and dolomite is presented by the following chemical formulas respectively:

$2HCl + CaCO_3 \rightarrow CaCl_2 + CO_2 + H_2O$

$4HCl + CaMg(CO_3)_2 \rightarrow CaCl_2 + MgCl_2 + 2CO_2 + 2H_2O$

An acid treatment should be designed to achieve its function at lowest possible cost. The design requires considerations of many physical and chemical interactions taking place between the injected fluids and the reservoir minerals and fluids present in the rocks. The most important of these phenomena are[1]:

- Mass transfer of acid molecules to the mineral surface. Acid reactions with minerals are termed heterogeneous reactions because they occur at the boundary between the solid and liquid rather than in bulk phases.
- The physical change in the pore structure caused by dissolution of some minerals by acid is the mechanism by which matrix acidizing increases permeability. The manner in which the pore structure changes is fundamentally different in carbonates and sandstone, which leads to radically different approaches in modeling the acidizing process.
- Secondary reactions occur in acidizing that can result in precipitation of reaction products from bulk liquid phase. Obviously, precipitated solids may block pore spaces and work against the goal of matrix acidizing.
- A successful acidizing treatment requires contacting all damaged regions around the wellbore with acid. This is usually complicated by variation in the injectivity to acid along the wellbore, which leads to the use of special acidizing techniques to obtain good acid coverage (acid diversion).
- Some other acids such as chemically retarded acids and viscous emulsified acids or hydrochloric acid containing effective fluid loss additives are used in matrix acidizing to increase the stimulation efficiency.

For a successful carbonate matrix stimulation treatment, it is important to acidize under conditions that will lead to the formation of deep penetration wormholes using minimal acid volumes. In order to achieve a successful acid treatment, the acid job should be designed at optimum field injection conditions. It is, therefore, necessary before injecting acid into the treated formation, that the concentration of the acid and the injection volume are determined before acid stimulation process is carried out[2].

Scaling-up the laboratory acid core data to field conditions is the main issue in the application of acid stimulation to field conditions. There are two methods of scaling-up acid laboratory data to field conditions, which are based on wormhole propagation and density (wormhole number per unit surface area)[3]. The simplest method involves scaling-up the reaction rate to maintain the same velocity into the matrix. This method inherently assumes that the wormhole density is the same in the field as in the laboratory experiments. The second method uses the wormhole density and surface area to scale-up the dissolution in the field [3]. If it were possible to predict the number, the diameter and the propagation of the

wormholes, then the increasing permeability around the wellbore could be predicted. Unfortunately, this prediction is not possible experimentally or theoretically [2,3]. Most of the published models claim that wormhole penetration distance is predominantly controlled by formation porosity and acid volume. These methods are currently introducing many simplifications to predict the acid volume injected at optimum acid injection rate for the treated well [4,5]. These oversimplifications fail to take into account the relevant physical mechanisms of wormhole formation and propagation and therefore, the models are not reliable enough for extrapolating laboratory data to the reservoir [5].

The challenge of scaling-up the fundamental mechanics of carbonate dissolution to field conditions is the difficulty in translating the acid efficiency from one geometry and size to a different geometry and size in a manner that leads itself to easy utilization by those requiring a carbonate stimulation model[2].

For a carbonate acidizing model to be useful to the industry, it must correctly capture the fundamental characteristics of the dissolution phenomenon, correctly scale-up the phenomenon to field conditions and require basic input parameters that are readily available. Any acid treatment method or model will first be validated for fundamental consistency using laboratory data before using it in field applications [3].

THE NEW SCALING-UP PROCEDURE

In this study, a new quantitative technique for scaling-up laboratory acid core data (acid pore volume injected) to field applications is set up, based on converting the acid performance curve obtained from the laboratory experiments to field performance curve, from which acid penetration radius and injection volume can be predicted.

The scaling-up procedure is run as follows:

1- Perform acid flooding laboratory experiments on actual core samples collected from the candidate well for acid treatment.

2 - Construct the laboratory acid performance curve for all the core plugs by plotting the cumulative acid pore volume injected versus the stimulation ratio ($\overline{k_s}/k_e$).

3 - The laboratory acid performance curve is converted to field performance curve using the following technique:

a - Assume different radii (r_s) to be acidized.

b - Assume the acid will dissolve different percentage of mineral volume (χ).

c - Calculate the original reservoir rock pore volume invaded by acid including the rock pore volume generated by acid dissolution to an assumed radius (r_s), using the following equation:

$$V_r = V_{pi} + V_{rs} \tag{1}$$

$$V_r = \pi h \phi (r_s^2 - r_w^2)(1 - S_{or}) + \frac{\pi h (1-\phi)\chi (r_s^2 - r_w^2)}{\beta} \tag{2}$$

β (the dissolving power of the acid) is calculated from the following equation:

$$\beta = \frac{\nu_{minral}\, MW_{mineral}}{\nu_{acid}\, MW_{acid}} \tag{3}$$

As was mentioned before, 2 moles of hydrochloric acid (HCl) react with 1 mole of limestone (CaCO3), thus the β_{100} is:

$$\beta_{100} = \frac{(1)(100.1)}{(2)(36.5)} \tag{4}$$

The dissolving power of 28% HCl concentration is:

$$\beta_{28\%} = 0.28 \times \beta_{100} \tag{5}$$

Then, the volumetric dissolving power is:

$$\beta = \beta_{28\%} \frac{\rho_{acid\ solution}}{\rho_{mineral}} \tag{6}$$

4 - Considering the acid injection condition in the laboratory is the same as that of the reservoir, then

$$(P.V.I)_{lab.} = (P.V.I)_{field} \tag{7}$$

5 - Calculate the acid volume (V_s) knowing $(P.V.I)_{field}$ that gives the optimum increase in the stimulation ratio for the considered radius(r_s).

$$(P.V.I)_{field} = \frac{V_s}{V_r} \tag{8}$$

6 - Repeat the previous steps for each assumed acid penetration radius (r_s).

7 - Plot the relation between the acid volumes injected per foot and each acid penetration radius for each assumed, χ.

RESULTS AND DISCUSSION

The data used in this study were taken from the laboratory acid study for core samples collected from wells located in one of the biggest fields in Libya. The reservoir, from which the core samples were taken, consists of a calcareous limestone formation. Very high formation damage has been observed by the production tests on appraisal wells B1, B2, B4 and B6 in this field. An acid stimulation study was conducted on actual core samples collected from C and E layers of well B4. The acid stimulation study (the laboratory acid core tests) was carried out on these selected core samples by injecting different pore volumes of a regular acid and acid mixture at simulated reservoir conditions. The improvement of the permeability of these tested cores was determined after each acid pore volume injected.

HCl was used in this study at 28% concentration as a regular acid and mixed with different acid mixtures. The formulation of the injected acid mixture is described below:

- 28% HCl chemically retarded.
- 28% HCl in emulsion with oil.
- 28% HCl with diverting agent.

The physical properties and the perforated intervals for B1, B2 and B6 wells are illustrated in Table 1.

Experimental acid core data for layers C and E at different acid mixtures are illustrated in Tables 2 and 3 respectively. The laboratory acid performance curves for these layers C and E were constructed by plotting the cumulative acid pore volume injected versus the stimulation ratio ($\overline{k}_s/k_e$) (Figs. 1 and 2).

The acid performance curve for layer C (Fig.1) indicates that emulsified HCl and retarded HCl acids produced higher acid stimulation ratio compared to 28% HCl acid without additives. The figure also shows that 28% HCl concentration with different acid additives reached maximum stimulation ratio approximately at the same acid pore volume injected. From figure 2, the injection of 28% HCl concentration without additives causes damage to the permeability of the core. Each of the emulsified, retarded and diverted HCl acids gives different stimulation ratio improvements at varying acid pore volumes.

From figures 1 and 2, it can be noticed that the stimulation performance of each treated core is dependent on the amount of acid injected through the core. It can also be noticed that maximum stimulation ratio is reached at optimum acid volumes injected. Additional volumes of the injected acid higher than the optimum values will produce decreasing stimulation ratio values.

According to the acid laboratory performance curve for zone C (Fig. 1), the stimulation ratio starts to increase at acid pore volumes of 7.7, 8.2, 8.5 and 8.7 for 28% HCl, 28% HCl emulsified, 28% HCl retarded and 28% HCl diverted respectively. For zone E, the increase in the stimulation ratio (Fig. 2) started at injected acid pore volumes of 5.5, 5.7 and

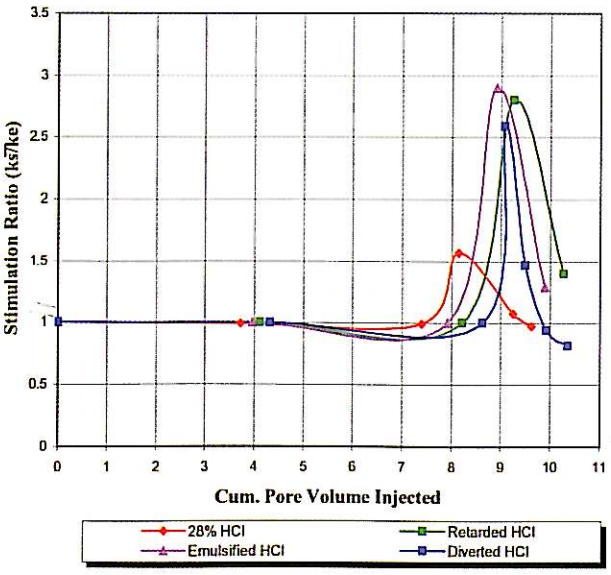


Fig. 1. Laboratory acid performance curve layer(C).

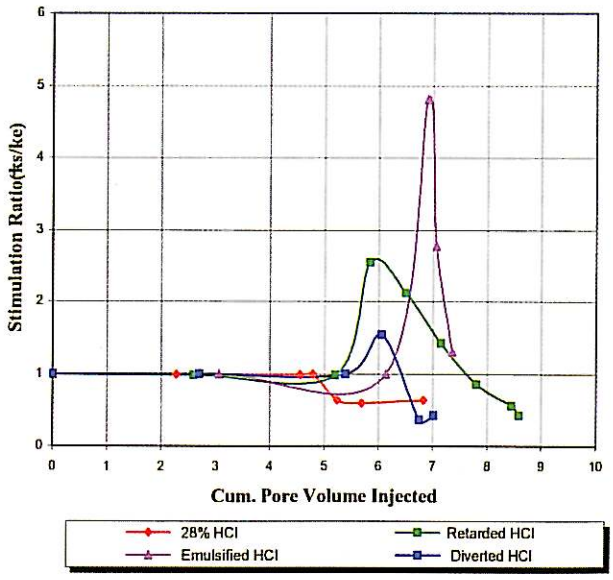


Fig. 2. Laboratory acid performance curve layer (E).

Table 1. Formation damaged intervals of the three wells.

Welll	Interval	Zone	h (ft)	ϕ (%)	S_{or} (%)	r_w (ft)
B1	(8206 – 8222)	C	16	12	10	0.35
B1	(8350 – 8440)	E	90	22	29	0.35
B2	(8525 – 8552)	E	27	28	43	0.35
B2	(8354 – 8420)	C	50	8	25	0.35
B6	(8478 – 8518)	C	40	9	20	0.35

Table 2. The laboratory acid core data for four core samples taken from layer (C) treated with different acid mixtures.

28% HCl		Emulsified 28%HCl		Retarded 28% HCl		Diverted 28% HCl	
Cum. acid pore volume	$\bar{k}_s/k_e$	Cum. acid pore volume	$\bar{k}_s/k_e$	Cum. acid pore volume	$\bar{k}_s/k_e$	Cum. acid pore volume	$\bar{k}_s/k_e$
0	1	0	1	0	1	0	1
3.7	0.99	3.95	1	4.11	1	4.31	1
7.39	0.99	7.91	1	8.22	1	8.62	1
8.13	1.57	8.9	2.9	9.25	2.8	9.06	2.59
9.24	1.07	9.88	1.29	10.27	1.4	9.49	1.47
9.61	0.97					9.92	0.94
						10.35	0.81

Table 3. The laboratory acid core data for four core samples taken from layer (E) treated with different acid mixtures.

28% HCl		Emulsifed 28% HCl		Retarded 28% HCl		Diverted 28%HCl	
Cum. acid P.V.I	$\bar{k}_s/k_e$	Cum. acid P.V.I	$\bar{k}_s/k_e$	Cum. acid P.V.I	$\bar{k}_s/k_e$	Cum. acid	$\bar{k}_s/k_e$
0	1	0	1	0	1	0	1
2.27	0.99	3.06	1	2.6	0.98	2.7	1
4.55	0.99	6.13	1	5.2	0.98	5.39	1
4.78	1	6.89	4.81	5.85	2.55	6.06	1.54
5.23	0.63	7.05	2.78	6.5	2.12	6.74	0.36
5.69	0.59	7.35	1.3	7.15	1.42	7.01	0.42
6.82	0.63			7.8	0.85		
				8.45	0.56		
				8.58	0.42		

6.4 for the 28% HCl, 28% retarded HCl, 28% diverted HCl and 28% emulsified HCl respectively.

Using the above-mentioned scale-up procedure outlined in equations 1 through 8, the laboratory acid performance curves for layers C and E, (Figs.1and 2 respectively), were utilized to calculate the required acid injection volume at radial distances of 1, 1.75, 2 and 3 ft away from the wellbore for different percentages of acid rock dissolution of 2%, 3% and 5% for the studied wells of B1, B2 and B6 from the field. The calculated acid injection volumes (gal/ft) for each acid rock dissolution percentage are presented in Tables 4 through 18. The tables contain acid stimulation ratios from each laboratory acid performance curve for each considered radius at selected acid injection pore volumes for maximum

Table 4. The minimum and maximum acid field volumes and the penetration radius of acid: well B1 zone C for rock dissolution of 2%.

		28%HCl				Emulsified 28%HCl				Retded 28%HCl				Diverted 28%HCl			
r(ft)	Vr (ft^3)	$P.V.I_{field}$ (V_s/V_r)	$\bar{k}_s/k_e$	Vs (bbl)	gal/ft	$P.V.I_{field}$ (V_s/V_r)	$\bar{k}_s/k_e$	Vs (bbl)	gal/ft	$P.V.I_{field}$ (V_s/V_r)	$\bar{k}_s/k_e$	Vs (bbl)	gal/ft	$P.V.I_{field}$ (V_s/V_r)	$\bar{k}_s/k_e$	Vs (bbl)	gal/ft
1	9.58	7.7 7.9 8.13	1.15 1.3 1.56	13 13.5 14	34 35 37	8.3 8.5 8.9	1.3 1.6 2.9	14 14.5 15	37 38 39	8.5 8.9 9.3	1.2 1.7 2.8	14.5 15 16	38 39 42	8.7 8.9 9.06	1.1 1.3 2.59	15 15 15	39 39 39
1.75	32	7.7 7.9 8.13	1.15 1.3 1.56	44 45 46	116 118 121	8.3 8.5 8.9	1.3 1.6 2.9	47 48 51	123 126 134	8.5 8.9 9.3	1.2 1.7 2.8	48 51 53	126 134 139	8.7 8.9 9.06	1.1 1.3 2.59	50 51 52	131 134 136
2	42.3	7.7 7.9 8.13	1.15 1.3 1.56	58 60 61	152 157 160	8.3 8.5 8.9	1.3 1.6 2.9	62 64 67	163 168 176	8.5 8.9 9.3	1.2 1.7 2.8	64 67 70	168 176 184	8.7 8.9 9.06	1.1 1.3 2.59	65 66 68	171 173 178
3	97	7.7 7.9 8.13	1.15 1.3 1.56	133 136 140	349 357 367	8.3 8.5 8.9	1.3 1.6 2.9	143 147 154	375 386 404	8.5 8.9 9.3	1.2 1.7 2.8	147 154 161	386 404 423	8.7 8.9 9.06	1.1 1.3 2.59	150 152 156	394 399 409

Table 5. The minimum and maximum acid field volumes and the penetration radius of acid: well B1 zone C for rock dissolution of 3%.

		28%HCl				Emulsified 28%HCl				Retarded 28%HCl				Diverted 28%HCl			
r(ft)	Vr (ft^3)	$P.V.I_{field}$ (V_s/V_r)	$\bar{k}_s/k_e$	Vs (bbl)	gal/ft	$P.V.I_{field}$ (V_s/V_r)	$\bar{k}_s/k_e$	Vs (bbl)	gal/ft	$P.V.I_{field}$ (V_s/V_r)	$\bar{k}_s/k_e$	Vs (bbl)	gal/ft	$P.V.I_{field}$ (V_s/V_r)	$\bar{k}_s/k_e$	Vs (bbl)	gal/ft
1	12	7.7 7.9 8.13	1.15 1.3 1.56	16 17 17	42 44 45	8.3 8.5 8.9	1.3 1.6 2.9	18 18 19	47 47 50	8.5 8.9 9.3	1.2 1.7 2.8	18 19 20	47 50 52	8.7 8.8 9.06	1.1 1.3 2.59	18 19 19	47 50 50
1.75	40.2	7.7 7.9 8.13	1.15 1.3 1.56	55 56 58	144 147 152	8.3 8.5 8.9	1.3 1.6 2.9	59 61 64	155 160 168	8.5 8.9 9.3	1.2 1.7 2.8	61 64 66	160 168 173	8.7 8.8 9.06	1.1 1.3 2.59	62 63 65	163 165 171
2	52.9	7.7 7.9 8.13	1.15 1.3 1.56	72 74 76	189 194 199	8.3 8.5 8.9	1.3 1.6 2.9	78 80 84	205 210 220	8.2 8.9 9.3	1.2 1.7 2.8	80 84 88	210 220 231	8.7 8.8 9.06	1.1 1.3 2.59	82 83 85	215 218 223
3	121.3	7.7 7.9 8.13	1.15 1.3 1.56	166 171 176	436 449 462	8.3 8.5 8.9	1.3 1.6 2.9	179 184 192	470 483 504	8.5 8.9 9.3	1.2 1.16 2.7	184 192 201	483 504 528	8.7 8.8 9.06	1.1 1.3 2.59	188 190 196	493 500 514

Table 6. The minimum and maximum acid field volumes and the penetration radius of acid: well B1 zone C for rock dissolution of 5%.

		28%HCl				Emulsified 28%HCl				Retarded 28%HCl				Diverted 28%HCl			
r(ft)	Vr (ft^3)	$P.V.I_{field}$ (V_s/V_r)	$\bar{k}_s/k_e$	Vs (bbl)	gal/ft	$P.V.I_{field}$ (V_s/V_r)	$\bar{k}_s/k_e$	Vs (bbl)	gal/ft	$P.V.I_{field}$ (V_s/V_r)	$\bar{k}_s/k_e$	Vs (bbl)	gal/ft	$P.V.I_{field}$ (V_s/V_r)	$\bar{k}_s/k_e$	Vs (bbl)	gal/ft
1	16.8	7.7 7.9 8.13	1.15 1.3 1.56	23 24 24	60 63 63	8.3 8.5 8.9	1.3 1.6 2.9	25 25 27	66 66 71	8.5 8.9 9.3	1.2 1.7 2.8	25 27 28	66 71 73	8.7 8.8 9.06	1.1 1.3 2.59	26 26 27	68 68 71
1.75	56.3	7.7 7.9 8.13	1.15 1.3 1.56	77 79 81	202 207 213	8.3 8.5 8.9	1.3 1.6 2.9	83 85 89	218 223 234	8.5 8.9 9.3	1.2 1.7 2.8	85 89 93	223 234 244	8.7 8.8 9.06	1.1 1.3 2.59	87 88 91	228 231 239
2	74.2	7.7 7.9 8.13	1.15 1.3 1.56	102 104 107	268 273 281	8.3 8.5 8.9	1.3 1.6 2.9	110 112 118	289 294 309	8.5 8.9 9.3	1.2 1.7 2.8	112 118 123	302 309 323	8.7 8.8 9.06	1.1 1.3 2.59	115 116 120	302 304 315
3	170	7.7 7.9 8.13	1.15 1.3 1.56	233 239 246	612 627 645	8.3 8.5 8.9	1.3 1.6 2.9	251 257 269	659 674 706	8.5 8.9 9.3	1.2 1.7 2.8	257 269 281	674 706 737	8.7 8.8 9.06	1.1 1.3 2.59	263 266 274	690 698 719

Table 7. The minimum and maximum acid field volumes and the penetration radius of acid: well B2 zone C for rock dissolution of 2%.

		28% HCl				Emulsified 28%HCl				Retarded 28%HCl				Diverted 28%HCl			
r(ft)	Vr (ft^3)	$P.V.I_{field}$ (Vs/Vr)	$\bar{k}_s/k_e$	Vs (bbl)	gal/ft	$P.V.I_{field}$ (V_s/V_r)	$\bar{k}_s/k_e$	Vs (bbl)	gal/ft	$P.V.I_{field}$ (V_s/V_r)	$\bar{k}_s/k_e$	Vs (bbl)	gal/ft	$P.V.I_{field}$ (V_s/V_r)	$\bar{k}_s/k_e$	Vs (bbl)	gal/ft
1	24	7.7 7.8 8.13	1.15 1.3 1.56	33 34 35	28 28 29	8.3 8.5 8.9	1.3 1.6 2.9	35 36 38	29 30 32	8.5 8.9 9.3	1.2 1.7 2.8	36 38 40	30 32 34	8.7 8.8 9.06	1.1 1.3 2.59	37 38 39	31 32 33
1.75	80.45	7.7 7.8 8.13	1.15 1.3 1.56	110 113 116	92 95 97	8.3 8.5 8.9	1.3 1.6 2.9	119 122 127	100 102 107	8.5 8.9 9.3	1.2 1.7 2.8	122 127 133	102 107 112	8.7 8.8 9.06	1.1 1.3 2.59	125 126 130	105 106 109
2	105	7.7 7.8 8.13	1.15 1.3 1.56	144 148 152	121 124 128	8.3 8.5 8.9	1.3 1.6 2.9	155 159 166	130 133 139	8.5 8.9 9.3	1.2 1.7 2.8	159 166 174	133 139 146	8.7 8.8 9.06	1.1 1.3 2.59	163 164 169	137 138 142
3	242.9	7.7 7.8 8.13	1.15 1.3 1.56	333 342 352	280 287 296	8.3 8.5 8.9	1.3 1.6 2.9	359 368 385	302 309 323	8.5 8.9 9.3	1.2 1.7 2.8	368 385 402	309 323 337	8.7 8.8 9.06	1.1 1.3 2.59	376 381 392	316 320 329

Table 8. The minimum and maximum acid field volumes and the penetration radius of acid: well B2 zone C for rock dissolution of 3%.

		28% HCl				Emulsified 28%HCl				Retarded 28%HCl				Diverted 28%HCl			
r(ft)	Vr (ft^3)	$P.V.I_{field}$ (Vs/Vr)	$\bar{k}_s/k_e$	Vs (bbl)	gal/ft	$P.V.I_{field}$ (V_s/V_r)	$\bar{k}_s/k_e$	Vs (bbl)	gal/ft	$P.V.I_{field}$ (V_s/V_r)	$\bar{k}_s/k_e$	Vs (bbl)	gal/ft	$P.V.I_{field}$ (V_s/V_r)	$\bar{k}_s/k_e$	Vs (bbl)	gal/ft
1	31.9	7.7 7.9 8.13	1.15 1.3 1.56	44 45 46	37 38 39	8.3 8.5 8.9	1.3 1.6 2.9	47 48 50	39 40 42	8.5 8.9 9.3	1.2 1.7 2.8	48 50 53	40 42 44	8.7 8.8 9.06	1.1 1.3 2.59	49 50 51	41 42 43
1.75	106.8	7.7 7.9 8.13	1.15 1.3 1.56	147 150 155	123 126 130	8.3 8.5 8.9	1.3 1.6 2.9	158 162 169	133 136 142	8.5 8.9 9.3	1.2 1.7 2.8	162 169 177	136 142 149	8.7 8.8 9.06	1.1 1.3 2.59	165 167 172	139 140 144
2	139.8	7.7 7.9 8.13	1.15 1.3 1.56	192 197 202	161 165 170	8.3 8.5 8.9	1.3 1.6 2.9	207 212 221	174 178 186	8.5 8.9 9.3	1.2 1.7 2.8	212 221 231	178 186 194	8.7 8.8 9.06	1.1 1.3 2.59	217 219 225	182 184 189
3	322.5	7.7 7.9 8.13	1.15 1.3 1.56	442 454 467	371 381 392	8.3 8.5 8.9	1.3 1.6 2.9	477 488 511	401 410 429	8.5 8.9 9.3	1.2 1.7 2.8	488 511 534	420 429 448	8.7 8.8 9.06	1.1 1.3 2.59	500 505 520	420 424 437

Table 9 . The minimum and maximum acid field volumes and the penetration radius of acid: well B2 zone C for rock dissolution of 5%.

		28% HCl				Emulsified 28%HCl				Retarded 28%HCl				Diverted 28%HCl			
r(ft)	Vr (ft^3)	$P.V.I_{field}$ (Vs/Vr)	$\bar{k}_s/k_e$	Vs (bbl)	gal/ft	$P.V.I_{field}$ (V_s/V_r)	$\bar{k}_s/k_e$	Vs (bbl)	gal/ft	$P.V.I_{field}$ (V_s/V_r)	$\bar{k}_s/k_e$	Vs (bbl)	gal/ft	$P.V.I_{field}$ (V_s/V_r)	$\bar{k}_s/k_e$	Vs (bbl)	gal/ft
1	47.7	7.7 7.9 8.13	1.15 1.3 1.56	65 67 69	55 56 58	8.3 8.5 8.9	1.3 1.6 2.9	70 72 76	59 60 64	8.5 8.9 9.3	1.2 1.7 2.8	72 76 79	60 64 66	8.7 8.8 9.06	1.1 1.3 2.59	74 75 77	62 63 65
1.7 5	159.6	7.7 7.9 8.13	1.15 1.3 1.56	219 224 231	184 188 194	8.3 8.5 8.9	1.3 1.6 2.9	236 242 253	198 203 212	8.5 8.9 9.3	1.2 1.7 2.8	242 253 264	203 212 222	8.7 8.8 9.06	1.1 1.3 2.59	247 250 257	207 210 216
2	209.3	7.7 7.9 8.13	1.15 1.3 1.56	287 294 303	241 247 254	8.3 8.5 8.9	1.3 1.6 2.9	309 317 332	259 266 279	8.5 8.9 9.3	1.2 1.7 2.8	317 332 347	266 279 291	8.7 8.8 9.06	1.1 1.3 2.59	324 328 338	272 275 284
3	481.8	7.7 7.9 8.13	1.15 1.3 1.55	661 678 698	555 569 586	8.3 8.5 8.9	1.3 1.6 2.9	712 729 764	598 612 642	8.5 8.9 9.3	1.2 1.7 2.8	729 764 800	612 642 672	8.7 8.8 9.06	1.1 1.3 2.59	627 755 777	627 634 652

Table 10. The minimum and maximum acid field volumes and the penetration radius of acid: well B6 zone C for rock dissolution 2%.

		28% HCl				Emulsified 28%HCl				Retarded 28%HCl				Diverted 28%HCl			
r(ft)	Vr (ft^3)	$P.V.I_{field}$ (V_s/V_r)	$\bar{k}_s/k_e$	Vs (bbl)	gal/ft	$P.V.I_{field}$ (V_s/V_r)	$\bar{k}_s/k_e$	Vs (bbl)	gal/ft	$P.V.I_{field}$ (V_s/V_r)	$\bar{k}_s/k_e$	Vs (bbl)	gal/ft	$P.V.I_{field}$ (V_s/V_r)	$\bar{k}_s/k_e$	Vs (bbl)	gal/ft
1	20.4	7.7 7.9 8.13	1.15 1.3 1.56	28 29 29	29 30 30	8.3 8.5 8.9	1.4 1.6 2.9	30 31 32	31 33 34	8.5 8.9 9.3	1.2 1.7 2.8	31 32 34	33 34 36	8.7 8.8 9.06	1.1 1.3 2.59	32 32 33	34 34 35
1.75	68.3	7.7 7.9 8.13	1.15 1.3 1.56	94 96 99	99 101 104	8.3 8.5 8.9	1.4 1.6 2.9	101 103 108	106 108 113	8.5 8.9 9.3	1.2 1.7 2.8	103 108 113	108 113 119	8.7 8.8 9.06	1.1 1.3 2.59	106 107 110	111 112 115
2	90.2	7.7 7.9 8.13	1.15 1.3 1.56	124 127 131	130 133 137	8.3 8.5 8.9	1.4 1.6 2.9	133 136 143	140 143 150	8.5 8.9 9.3	1.2 1.7 2.8	136 143 149	143 150 156	8.7 8.8 9.06	1.1 1.3 2.59	140 141 145	147 148 152
3	206.3	7.7 7.9 8.13	1.15 1.3 1.56	283 290 299	297 304 314	8.3 8.5 8.9	1.4 1.6 2.9	305 312 327	320 328 343	8.5 8.9 9.3	1.2 1.7 2.8	312 327 342	328 343 359	8.7 8.8 9.06	1.1 1.3 2.59	320 323 333	336 339 350

Table 11. The minimum and maximum acid field volumes and the penetration radius of acid : well B6 zone C for rock dissolution of 3%.

		28% HCl				Emulsified 28%HCl				Retarded 28%HCl				Diverted 28%HCl			
r(ft)	Vr (ft^3)	$P.V.I_{field}$ (V_s/V_r)	$\bar{k}_s/k_e$	Vs (bbl)	gal/ft	$P.V.I_{field}$ (V_s/V_r)	$\bar{k}_s/k_e$	Vs (bbl)	gal/ft	$P.V.I_{field}$ (V_s/V_r)	$\bar{k}_s/k_e$	Vs (bbl)	gal/ft	$P.V.I_{field}$ (V_s/V_r)	$\bar{k}_s/k_e$	Vs (bbl)	gal/ft
1	26.6	7.7 7.9 8.13	1.15 1.3 1.56	36 37 38	38 39 40	8.3 8.5 8.9	1.3 1.6 2.9	39 40 42	41 42 44	8.5 8.9 9.3	1.2 1.7 2.79	40 42 44	42 44 46	8.7 8.8 9.06	1.1 1.3 2.59	41 42 43	43 44 45
1.75	89.2	7.7 7.9 8.13	1.15 1.3 1.56	122 125 129	128 130 135	8.3 8.5 8.9	1.3 1.6 2.85	132 135 141	139 142 148	8.5 8.9 9.3	1.2 1.7 2.75	135 141 148	142 148 155	8.7 8.8 9.06	1.1 1.3 2.59	138 140 144	145 147 151
2	117.7	7.7 7.9 8.13	1.15 1.3 1.56	161 165 170	169 171 178	8.3 8.5 8.9	1.3 1.6 2.85	174 178 186	183 187 195	8.5 8.9 9.3	1.2 1.7 2.8	178 186 195	187 195 205	8.7 8.8 9.06	1.1 1.3 2.59	182 184 190	191 193 199
3	269.3	7.7 7.9 8.13	1.15 1.3 1.55	369 378 390	387 393 409	8.3 8.5 8.9	1.3 1.6 2.9	398 408 427	418 428 448	8.5 8.9 9.3	1.2 1.7 2.7	408 427 446	428 448 468	8.7 8.8 9.06	1.1 1.3 2.59	417 422 434	438 443 456

Table 12. The minimum and maximum acid field volumes and the penetration radius of acid: well B6 zone C for rock dissolution of 5%.

		28% HCl				Emulsified 28%HCl				Retarded 28%HCl				Diverted 28%HCl			
r(ft)	Vr (ft^3)	$P.V.I_{field}$ (V_s/V_r)	$\bar{k}_s/k_e$	Vs (bbl)	gal/ft	$P.V.I_{field}$ (V_s/V_r)	$\bar{k}_s/k_e$	Vs (bbl)	gal/ft	$P.V.I_{field}$ (V_s/V_r)	$\bar{k}_s/k_e$	Vs (bbl)	gal/ft	$P.V.I_{field}$ (V_s/V_r)	$\bar{k}_s/k_e$	Vs (bbl)	gal/ft
1	39	7.7 7.9 8.13	1.15 1.3 1.56	53 55 56	56 58 59	8.3 8.5 8.9	1.3 1.6 2.9	58 59 62	61 62 65	8.5 8.9 9.3	1.2 1.7 2.8	59 62 64	62 65 67	8.7 8.8 9.06	1.1 1.3 2.59	60 61 63	63 64 66
1.75	131	7.7 7.9 8.13	1.15 1.3 1.56	180 184 190	189 193 199	8.3 8.5 8.9	1.3 1.6 2.85	194 198 208	204 208 218	8.5 8.9 9.3	1.2 1.7 2.8	198 208 217	208 218 228	8.7 8.8 9.06	1.1 1.3 2.59	203 205 211	213 215 221
2	172. 7	7.7 7.9 8.13	1.15 1.3 1.56	237 243 250	249 255 262	8.3 8.5 8.9	1.3 1.6 2.85	255 261 274	268 274 288	8.5 8.9 9.3	1.2 1.7 2.8	261 274 286	274 288 300	8.7 8.8 9.06	1.1 1.3 2.59	267 271 279	280 284 293
3	395. 4	7.7 7.9 8.13	1.15 1.3 1.55	542 556 572	569 584 601	8.3 8.5 8.9	1.3 1.6 2.8	584 598 627	613 628 658	8.5 8.9 9.3	1.2 1.7 2.8	598 627 655	628 658 688	8.7 8.8 9.06	1.1 1.3 2.59	613 620 638	644 651 670

Table 13. The minimum and maximum acid field volumes and the penetration radius of acid : well B1 zone E for rock dissolution of 2%.

		28% HCl				Emulsified 28%HCl				Retarded 28%HCl				Diverted 28%HCl			
r(ft)	Vr (ft^3)	$P.V.I_{field}$ (V_s/V_r)	$\bar{k}_s/k_e$	Vs (bbl)	gal/ft	$P.V.I_{field}$ (V_s/V_r)	$\bar{k}_s/k_e$	Vs (bbl)	gal/ft	$P.V.I_{field}$ (V_s/V_r)	$\bar{k}_s/k_e$	Vs (bbl)	gal/ft	$P.V.I_{field}$ (V_s/V_r)	$\bar{k}_s/k_e$	Vs (bbl)	gal/ft
1	62.8	–	–	–	–	6.4 6.6 6.89	1.25 2 4.81	72 74 77	34 35 36	5.5 5.6 5.85	1.18 1.6 2.55	61 63 65	28 29 30	5.7 5.8 6.06	1.1 1.3 1.54	64 65 68	30 30 32
1.75	210.3	–	–	–	–	6.4 6.6 6.89	1.25 2 4.81	240 247 258	112 115 120	5.5 5.6 5.85	1.18 1.6 2.55	206 210 219	96 98 102	5.7 5.8 6.06	1.1 1.3 1.54	213 217 227	99 101 106
2	277.3	–	–	–	–	6.4 6.6 6.89	1.25 2 4.81	316 326 340	147 152 159	5.5 5.6 5.85	1.18 1.6 2.55	272 276 289	127 129 135	5.7 5.8 6.06	1.1 1.3 1.54	281 286 299	131 133 135
3	635	–	–	–	–	6.4 6.6 6.89	1.25 2 4.81	724 746 779	338 348 363	5.5 5.6 5.85	1.18 1.6 2.55	622 633 661	290 295 308	5.7 5.8 6.06	1.1 1.3 1.54	645 656 685	301 306 320

Table 14. The minimum and maximum acid field volumes and the penetration radius of acid: well B1 zone E for rock dissolution of 3%.

		28% HCl				Emulsified 28%HCl				Retarded 28%HCl				Diverted 28%HCl			
r(ft)	Vr (ft^3)	$P.V.I_{field}$ (V_s/V_r)	$\bar{k}_s/k_e$	Vs (bbl)	gal/ft	$P.V.I_{field}$ (V_s/V_r)	$\bar{k}_s/k_e$	Vs (bbl)	gal/ft	$P.V.I_{field}$ (V_s/V_r)	$\bar{k}_s/k_e$	Vs (bbl)	gal/ft	$P.V.I_{field}$ (V_s/V_r)	$\bar{k}_s/k_e$	Vs (bbl)	gal/ft
1	74.8	–	–	–	–	6.4 6.6 6.89	1.25 2 4.81	85 88 92	40 41 43	5.5 5.6 5.85	1.18 1.6 2.55	73 75 78	34 35 36	5.7 5.8 6.06	1.1 1.3 1.54	76 77 81	35 36 38
1.75	250.5	–	–	–	–	6.4 6.6 6.89	1.25 2 4.81	285 294 307	133 137 143	5.5 5.6 5.85	1.18 1.6 2.55	245 250 261	114 117 122	5.7 5.8 6.06	1.1 1.3 1.54	254 259 270	118 121 126
2	330.4	–	–	–	–	6.4 6.6 6.89	1.25 2 4.81	376 388 405	175 181 189	5.5 5.6 5.85	1.18 1.6 2.55	324 329 344	151 153 160	5.7 5.8 6.06	1.1 1.3 1.54	335 341 357	156 159 167
3	756.5	–	–	–	–	6.4 6.6 6.89	1.25 2 4.81	862 889 926	402 415 432	5.5 5.6 5.85	1.18 1.6 2.55	751 754 788	350 352 368	5.7 5.8 6.06	1.1 1.3 1.54	768 781 816	358 364 381

Table 15. The minimum and maximum acid field volumes and the penetration radius of acid : well B1 zone E for rock dissolution of 5%.

		28% HCl				Emulsified 28%HCl				Retarded 28%HCl				Diverted 28%HCl			
r(ft)	Vr (ft^3)	$P.V.I_{field}$ (V_s/V_r)	$\bar{k}_s/k_e$	Vs (bbl)	gal/ft	$P.V.I_{field}$ (V_s/V_r)	$\bar{k}_s/k_e$	Vs (bbl)	gal/ft	$P.V.I_{field}$ (V_s/V_r)	$\bar{k}_s/k_e$	Vs (bbl)	gal/ft	$P.V.I_{field}$ (V_s/V_r)	$\bar{k}_s/k_e$	Vs (bbl)	gal/ft
1	98..8	–	–	–	–	6.4 6.6 6.89	1.25 2 4.81	113 116 121	53 54 56	5.5 5.6 5.85	1.18 1.6 2.55	97 98 103	45 46 48	5.7 5.8 6.06	1.1 1.3 1.54	100 102 107	47 48 50
1.75	331	–	–	–	–	6.4 6.6 6.89	1.25 2 4.81	377 389 406	176 181 189	5.5 5.6 5.85	1.18 1.6 2.55	324 330 345	151 154 161	5.7 5.8 6.06	1.1 1.3 1.54	336 342 357	157 160 167
2	436..6	–	–	–	–	6.4 6.6 6.89	1.25 2 4.81	498 513 536	232 239 250	5.5 5.6 5.85	1.18 1.6 2.55	428 435 456	200 203 213	5.7 5.8 6.06	1.1 1.3 1.54	443 451 471	207 210 220
3	999..6	–	–	–	–	6.4 6.6 6.89	1.25 2 4.81	1139 1174 1226	531 547 572	5.5 5.6 5.85	1.18 1.6 2.55	979 997 1041	457 465 486	5.7 5.8 6.06	1.1 1.3 1.54	1015 1032 1079	474 482 503

Table 16. The minimum and maximum acid field volumes and the penetration radius of acid: well B2 zone E for rock dissolution of 2%.

		28% HCl				Emulsified28%HCl				Retarded 28%HCl				Diverted 28%HCl			
r(ft)	Vr (ft^3)	$P.V.I_{field}$ (Vs/Vr)	$\bar{k}_s/k_e$	Vs (bbl)	gal/ft	$P.V.I_{field}$ (V_s/V_r)	$\bar{k}_s/k_e$	Vs (bbl)	gal/ft	$P.V.I_{field}$ (V_s/V_r)	$\bar{k}_s/k_e$	Vs (bbl)	gal/ft	$P.V.I_{field}$ (V_s/V_r)	$\bar{k}_s/k_e$	Vs (bbl)	gal/ft
1	18.5	–	–	–	–	6.4 6.6 6.89	1.25 2 4.81	21 22 23	33 34 36	5.5 5.6 5.85	1.18 1.6 2.55	18 18 19	28 28 30	5.7 5.8 6.06	1.1 1.3 1.54	19 19 20	29 29 31
1.75	63.7	–	–	–	–	6.4 6.6 6.89	1.25 2 4.81	73 75 78	114 117 121	5.5 5.6 5.85	1.18 1.6 2.55	62 63 66	96 98 103	5.7 5.8 6.06	1.1 1.3 1.54	65 66 69	101 103 107
2	81.9	–	–	–	–	6.4 6.6 6.89	1.25 2 4.81	93 96 100	145 149 155	5.5 5.6 5.85	1.18 1.6 2.55	80 82 85	124 127 132	5.7 5.8 6.06	1.1 1.3 1.54	83 84 88	129 131 137
3	187.4	–	–	–	–	6.4 6.6 6.89	1.25 2 4.81	214 220 230	333 342 358	5.5 5.6 5.85	1.18 1.6 2.55	184 187 195	286 291 303	5.7 5.8 6.06	1.1 1.3 1.54	190 193 202	295 300 314

Table 17. The minimum and maximum acid field volumes and the penetration radius of acid : well B2 zone E for rock dissolution of 3%.

		28% HCl				Emulsified 28%HCl				Retarded 28%HCl				Diverted 28%HCl			
r(ft)	Vr (ft^3)	$P.V.I_{field}$ (Vs/Vr)	$\bar{k}_s/k_e$	Vs (bbl)	gal/ft	$P.V.I_{field}$ (V_s/V_r)	$\bar{k}_s/k_e$	Vs (bbl)	gal/ft	$P.V.I_{field}$ (V_s/V_r)	$\bar{k}_s/k_e$	Vs (bbl)	gal/ft	$P.V.I_{field}$ (V_s/V_r)	$\bar{k}_s/k_e$	Vs (bbl)	gal/ft
1	21.9	–	–	–	–	6.4 6.6 6.89	1.25 2 4.81	25 26 27	39 40 42	5.5 5.6 5.85	1.18 1.6 2.55	21 22 23	33 34 36	5.7 5.8 6.06	1.1 1.3 1.54	22 23 24	34 36 37
1.75	74.9	–	–	–	–	6.4 6.6 6.89	1.25 2 4.81	85 88 92	132 137 143	5.5 5.6 5.85	1.18 1.6 2.55	73 75 78	114 117 121	5.7 5.8 6.06	1.1 1.3 1.54	76 77 81	118 120 126
2	96.6	–	–	–	–	6.4 6.6 6.89	1.25 2 4.81	110 113 118	171 176 183	5.5 5.6 5.85	1.18 1.6 2.55	95 96 101	148 149 157	5.7 5.8 6.06	1.1 1.3 1.54	98 100 104	152 155 162
3	221	–	–	–	–	6.4 6.6 6.89	1.25 2 4.81	252 260 271	392 404 421	5.5 5.6 5.85	1.18 1.6 2.55	216 220 230	336 342 358	5.7 5.8 6.06	1.1 1.3 1.54	224 228 238	348 355 370

Table 18. The minimum and maximum acid field volumes and the penetration radius of acid: well B2 zone E for rock dissolution of 5%.

		28% HCl				Emulsified 28%HCl				Retarded 28%HCl				Diverted 28%HCl			
r(ft)	Vr (ft^3)	$P.V.I_{field}$ (Vs/Vr)	$\bar{k}_s/k_e$	Vs (bbl)	gal/ft	$P.V.I_{field}$ (V_s/V_r)	$\bar{k}_s/k_e$	Vs (bbl)	gal/ft	$P.V.I_{field}$ (V_s/V_r)	$\bar{k}_s/k_e$	Vs (bbl)	gal/ft	$P.V.I_{field}$ (V_s/V_r)	$\bar{k}_s/k_e$	Vs (bbl)	gal/ft
1	28.5	–	–	–	–	6.4 6.6 6.89	1.25 2 4.81	32 33 35	50 51 54	5.5 5.6 5.85	1.18 1.6 2.55	28 28 30	43 43 47	5.7 5.8 6.06	1.1 1.3 1.54	29 29 31	45 45 48
1.75	97.2	–	–	–	–	6.4 6.6 6.89	1.25 2 4.81	111 114 119	173 177 185	5.5 5.6 5.85	1.18 1.6 2.55	95 97 101	148 151 157	5.7 5.8 6.06	1.1 1.3 1.54	99 100 105	154 155 163
2	126	–	–	–	–	6.4 6.6 6.89	1.25 2 4.81	144 148 155	224 230 241	5.5 5.6 5.85	1.18 1.6 2.55	123 126 131	191 196 204	5.7 5.8 6.06	1.1 1.3 1.54	128 130 136	199 202 211
3	288.4	–	–	–	–	6.4 6.6 6.89	1.25 2 4.81	329 339 354	512 527 551	5.5 5.6 5.85	1.18 1.6 2.55	282 288 300	439 448 467	5.7 5.8 6.06	1.1 1.3 1.54	293 298 311	456 463 484

value of the stimulation ratio and other values lower than the maximum value.

The calculations were done for three wells in the field in order to show the variation in acid performance treatment from one well to another in the same field. The difference in rock response to acid between layers C and E from one well to another is mainly related to the heterogeneity of formation rock pore structure and the variation of rock mineral composition.

The stimulation acid injection volumes corresponding to the maximum acid stimulation ratios for each treated core were plotted versus the assumed acid injection radii. Figures 3 to 20 illustrate the relationship between the acid stimulation radius and the acid injection volume required for the treatment. The figures were prepared for all types of acid used for the treatment at selected acid rock dissolution percentages, and were constructed for both the productive layers C and E in the three studied wells. These figures indicate that the acid stimulation radius is dependent on the type of acid additive used and also on the mineral composition at the matrix pore structure of the rock. The curves in these can be used to determine the volume of the treated acid required to obtain the maximum permeability improvement for selected acid radii near the wellbore.

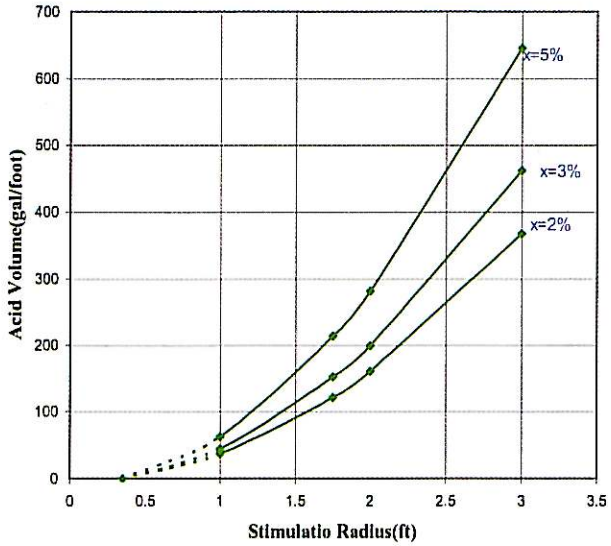


Fig. 3. The relation between stimulation radius and the acid volume for 28%HCl, well B1 zone C.

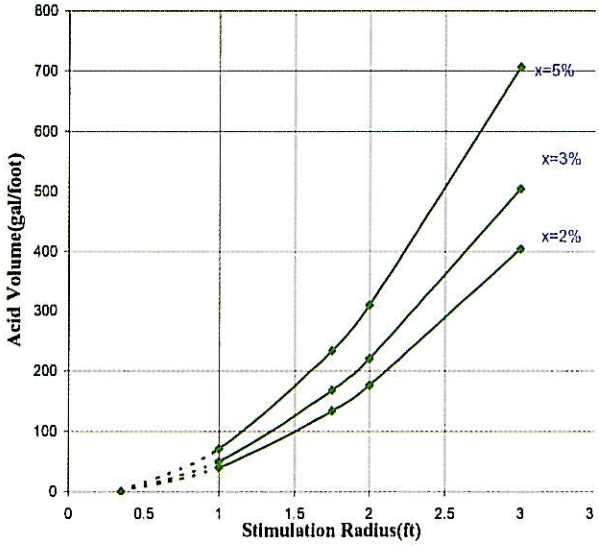


Fig. 4. The relation between stimulation radius and the acid volume for emulsified HCl, well B1 zone C.

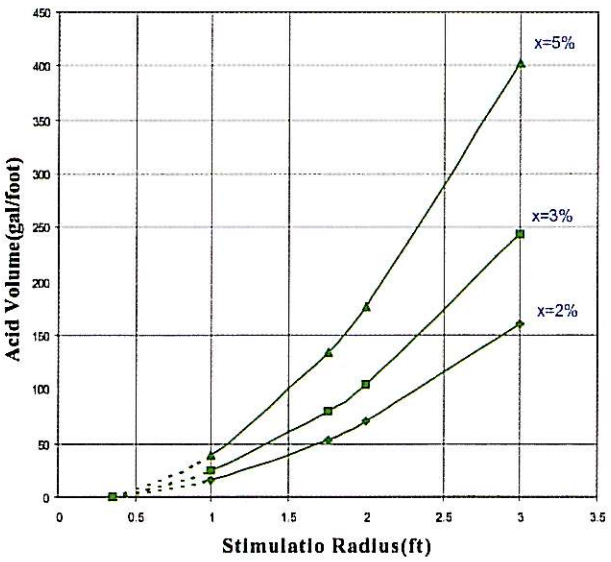


Fig. 5. The relation between stimulation radius and the acid volume for retarded HCl, well B1 zone C.

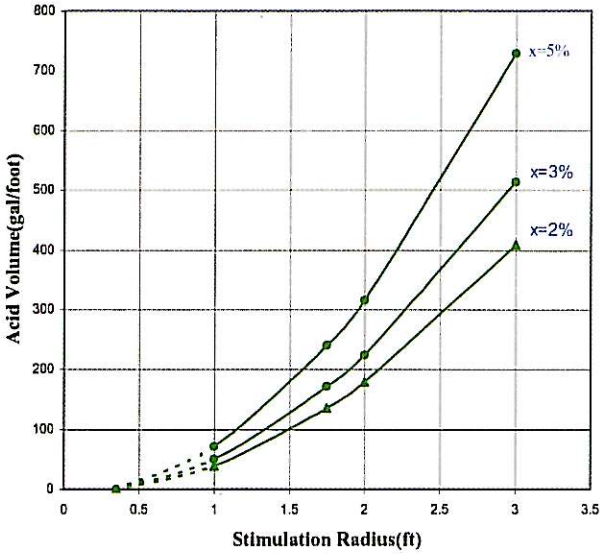


Fig. 6. The relation between stimulation radius and the acid volume for diverted HCl, well B1 zone C.

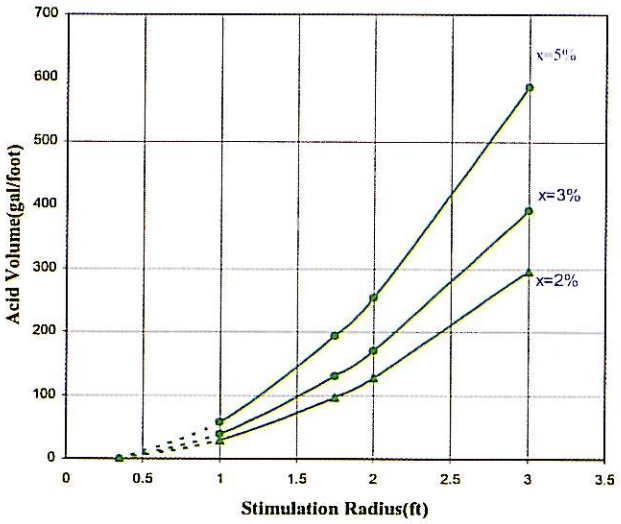


Fig. 7. The relation between stimulation radius and the acid volume for 28%HCl, well B2 zone C.

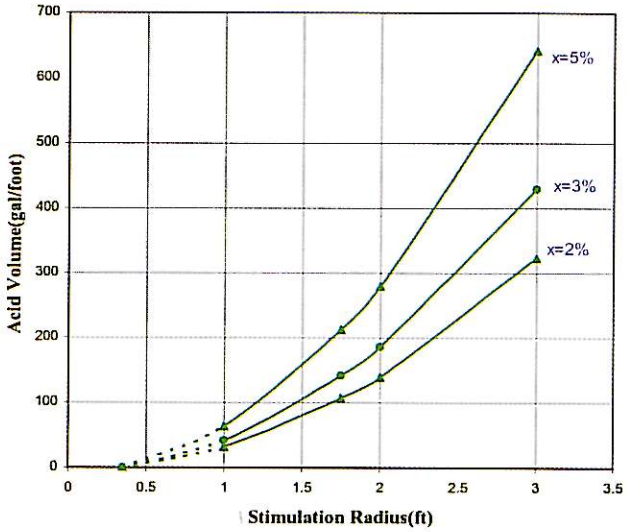


Fig. 8. The relation between stimulation radius and the acid volume for emulsified HCl, well B2 zone C.

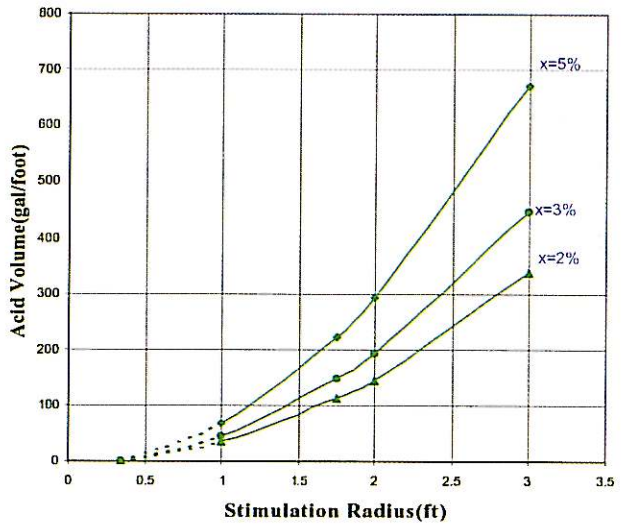


Fig. 9. The relation between stimulation radius and the acid volume for retarded HCl, well B2 zone C.

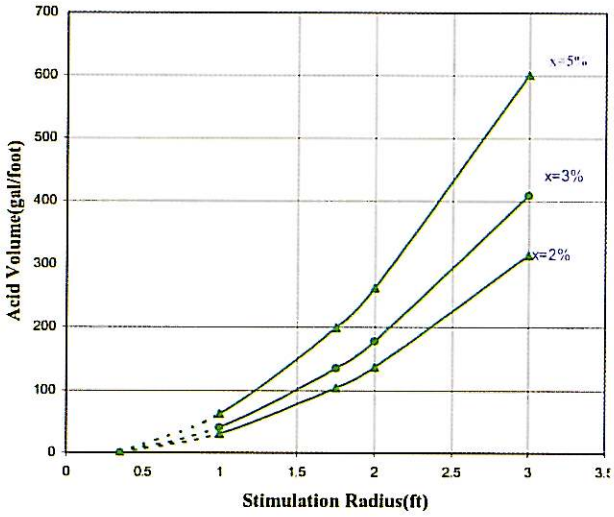


Fig. 10. The relation between stimulation radius and the acid volume for diverted HCl, well B2 zone C.

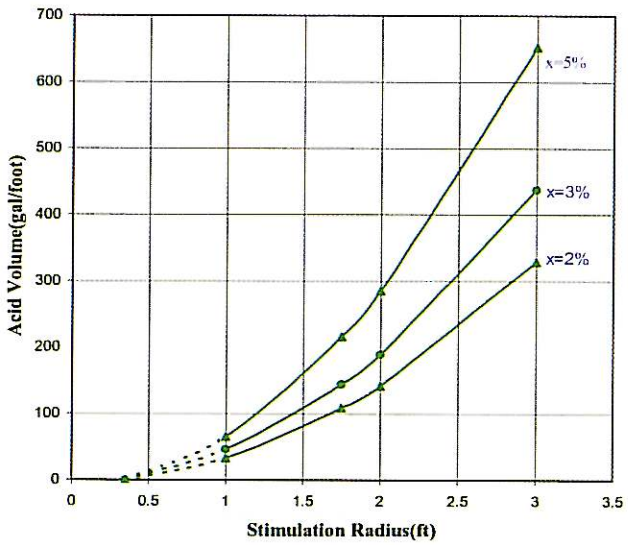


Fig. 11. The relation between stimulation radius and the acid volume for 28%HCl, well B6 zone C.

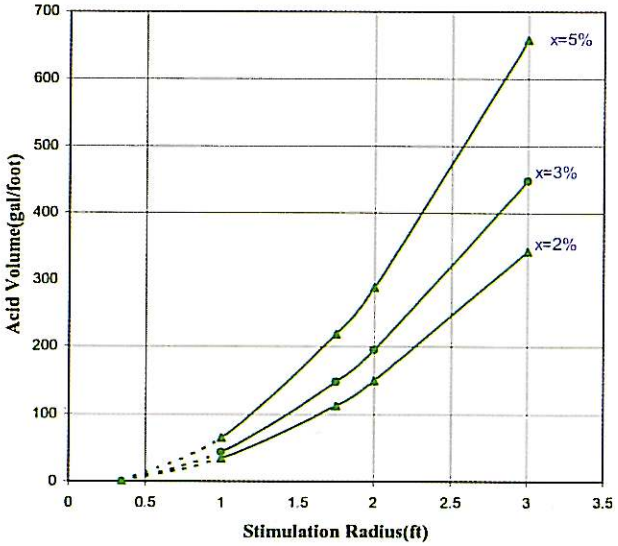


Fig. 12. The relation between stimulation radius and the acid volume for emulsified HCl, well B6 zone C.

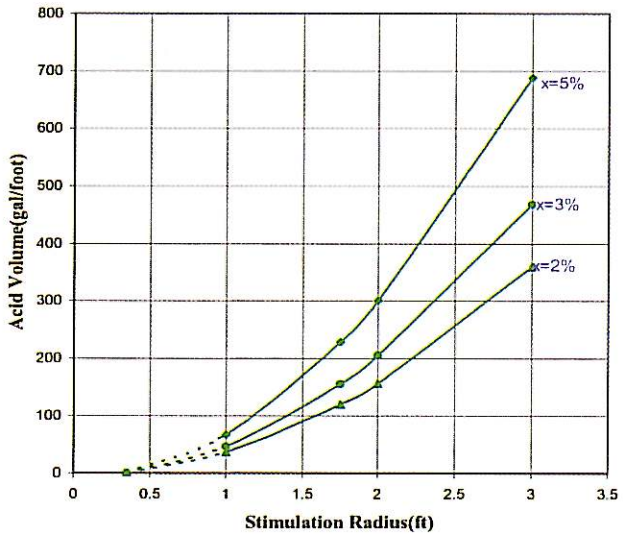


Fig. 13. The relation between stimulation radius and the acid volume for retarded HCl, well B6 zone C.

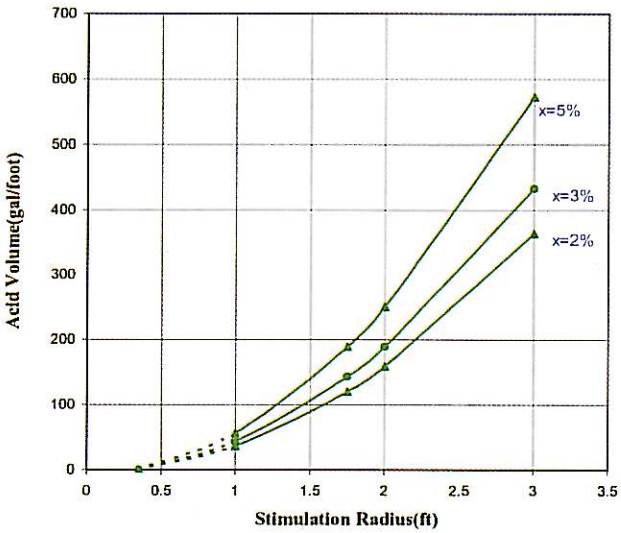


Fig. 14. The relation between stimulation radius and the acid volume for emulsified HCl, well B1 zone E.

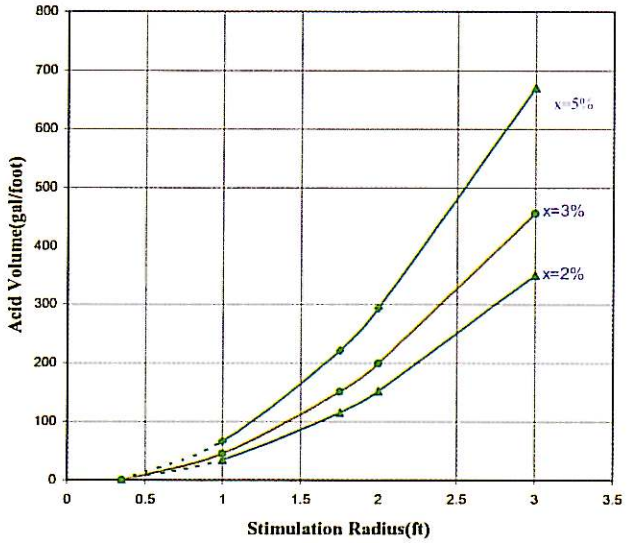


Fig. 15. The relation between stimulation radius and the acid volume for diverted HCl, well B6 zone C.

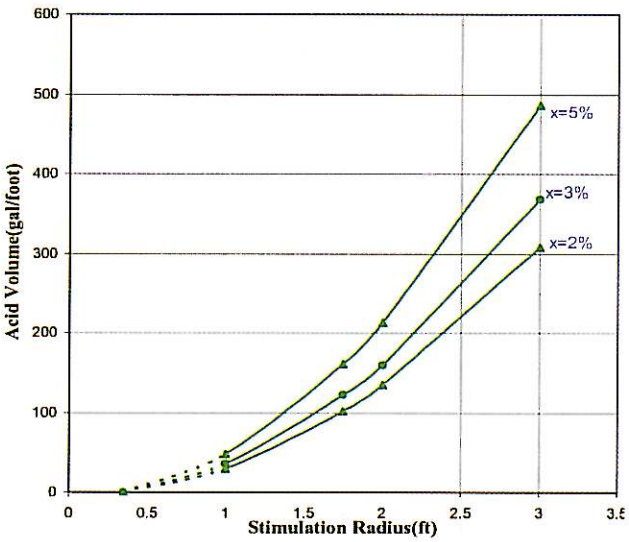


Fig. 16. The relation between stimulation radius and the acid volume for retarded HCl, well B1 zone E.

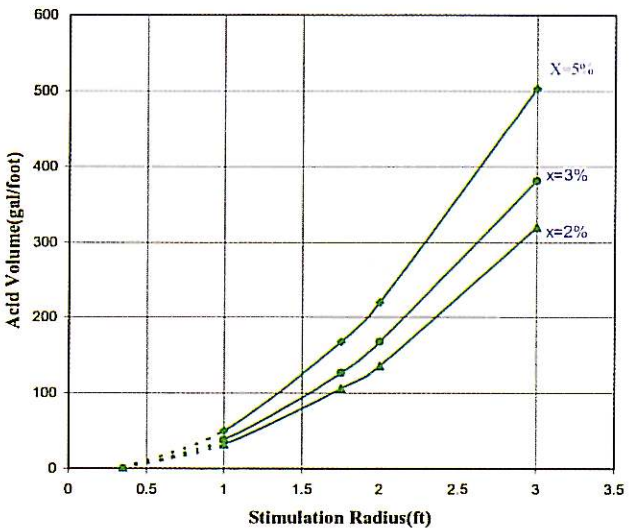


Fig. 17. The relation between stimulation radius and the acid volume for diverted HCl, well B1 zone E.

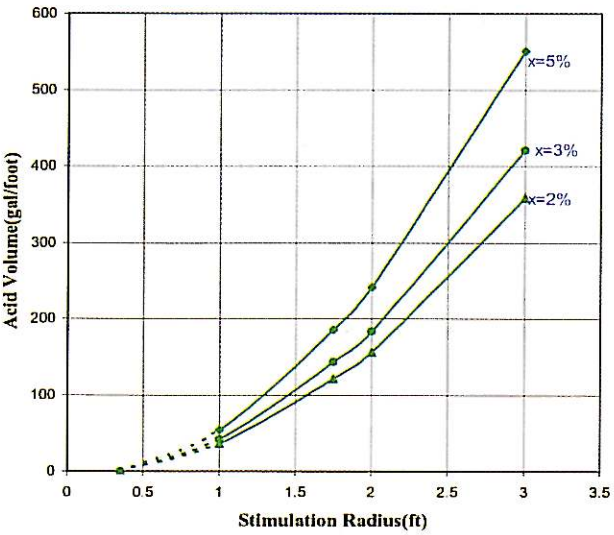


Fig. 18. The relation between stimulation radius and the acid volume for emulsified HCl, well B2 zone E.

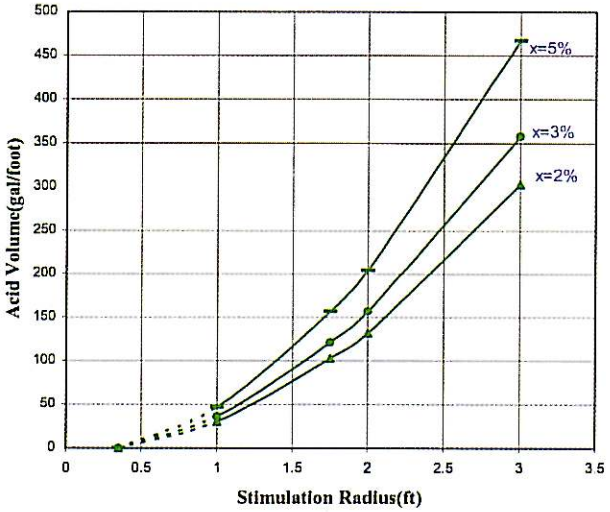


Fig. 19. The relation between stimulation radius and the acid volume for retarded HCl, well B2 zone E.

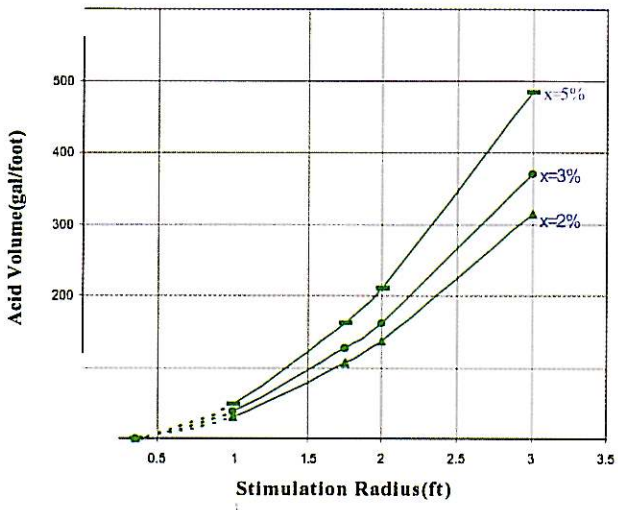


Fig. 20. The relation between stimulation radius and the acid volume for diverted HCl, well B2 zone E.

It is observed from Tables 4 to 18 that the acid stimulation ratio ($\overline{k}_s/k_e$) increases with increasing the acid pore volume injected. This increase continues until it reaches a maximum value after which any further increase in the injected pore volume will produce decreasing values of acid stimulation ratios. It is, therefore, recommended to determine experimentally the optimum required acid volume needed for any acidizing treatment.

Injecting higher acid volumes than required dissolves excessive rock minerals which the acid cannot suspend and carry, and re-precipitation of these minerals occurs which causes a damaging effect to the treated formation. In a radial geometry acid treatment, the volume of the acid needed to increase the porosity by dissolving a given percentage of the rock mineral varies with the square of the treatment radius. It is noted from Tables 4 to 18 that the acid volume needed to stimulate a reservoir should be designed according to the required percentage of the dissolution of the rock mineral and also according to the required acid penetration radius.

For reservoirs that have high residual oil saturation as is the case in well B2 zone E, it is recommended to use organic solvents and mutual solvents, along with the injected HCl acid in order to increase the contact between the acid and the rock surface which will result in decreasing the residual oil saturation of the reservoir.

CONCLUSIONS

1 - A new correlation technique for converting laboratory acid core data to field conditions is presented in this study.

2 - During any acid stimulation process, there is an optimum acid volume to be injected in order to produce the maximum stimulation ratio. Increasing the acid volume more than the optimum value causes a reduction in stimulation ratio.

3 - The designed acid volume is dependant on the required increase in the porosity as well as on the possible stimulation radius.

4 - The acid volume needed to stimulate the reservoir depends on acid type, acid additives and also on the physical properties and mineral composition of the rock.

5 - The volume of the injected acid for any acid treatment should be determined properly in order to achieve a successful acid treatment.

6 - Acid field curves that illustrate the relation between the acid stimulation radii and the required acid volumes were constructed for zones C and E.

Nomenclature

V_r	=	reservoir volume invaded by acid, ft^3.
V_{rs}	=	volume of the dissolved rock by acid, ft^3.
V_s	=	acid volume, ft^3.
V_{pi}	=	original pore volume invaded by acid, ft^3.
P.V.I	=	pore volume injected.
h	=	formation thickness, ft.
ϕ	=	reservoir porosity, fraction.
r_s	=	acid penetration radius, ft.
r_w	=	wellbore radius, ft.
S_{or}	=	residual oil saturation, fraction.

χ_2 = rock dissolution, fraction.
= acid dissolving power.
ν_{acid} = stoichiometric coefficient of the acid(2HCl).
$\nu_{mineral}$ = stoichiometric coefficient of the mineral($1CaCO_3$).
$\overline{k_s/k_e}$ = acid stimulation ratio.
k_s = stimulated zone permeability, darcy.
k_e = original zone permeability prior to acidizing, darcy.
$\overline{MW}_{mineral}$ = molecular weight of the mineral.
MW_{acid} = molecular weight of the acid.
$\rho_{acid\ solution}$ = density of the acid solution, lb/gal.
$\rho_{mineral}$ = density of the rock, lb/gal.

ACKNOWLEDGEMENTS

The authors express their appreciation to the management of the Petroleum Research Centre and the Department of Exploration and Reservoir Exploitation for their continuous support and encouragement and for providing all the necessary requirements to achieve this work.

REFERENCES

[1] Nasr M. and Elhemmali N., 1996(Jun.). Application of acid optimization technique to carbonate reservoirs. *The 6th international energy conference,* Beijing, China (890-893).

[2] Economides M. & Nolte K.G., 2000. *Reservoir Stimulation*. Third edition. Schlumberger.

[3] Fredd.C.N., 2000(Mar.). Dynamic model of wormhole formation demonstrates conditions for effective skin reduction during carbonate matrix acidizing. *SPE Permian Basin Oil and Gas Recovery Conference,* Texas.

[4] Ferdd C.N. and Miller. M. J., 2000(Feb.). Validation of carbonate matrix stimulation models. *SPE International Symposium*, Louisiana.

[5] Bazin.B., 2001(Feb.).From matrix acidizing to acid fracturing: a laboratory evaluation of acid/rock interactions. *SPE production & Facilities*, 22-29.

Petroleum Res. J. Vol. 16 (2004); P. 37–42, 2 Figs.

Estimation of the Error Range of True Vertical Depth Determination

G. Szigeti

تقدير مدى الخطأ في تحديد العمق العمودي الحقيقي

غابور سيغاتي

تقدم هذه الورقة نموذجاً لمنحنى من النوع الحلزوني ببارمترين، لوصف الوضع الهندسي المحتمل لعملية الحفر الدوار العميق، حيث تم التعرف على الأسباب التي تحول دون اتخاذ ثقب البئر لشكل الخط المستقيم وتصنيفها، وفي هذا الإطار تم استخدام طرق الهندسة التفاضلية لتحليل الطول، والانحراف الزاوي للمنحنى عن العمودي، والانحناء الجاوسي للنموذج، كما تم تفسير الانحناء بطريقة تخص ثقوب الآبار المبطنة، وقد أعطى التحليل العددي تقديراً لخطأ العمق العمودي عبارة عن دالة في بارمترين مستقلين أو دالة في الانحراف الزاوي للثقب. أهمية هذا التقدير تتعلق بالوضع الهندسي لتماس النفط بالماء الذي يمثل بدوره مؤشراً على نوعية الخزان النفطي.

Abstract: *The present paper suggests a spiral type curve model with two parameters for potential description of the geometry of deep rotary drilling. The reasons that borehole geometry never coincides with a straight line are enumerated and classified. The length, the angular deviation of the curve from vertical, and the Gaussian curvature of the model are analyzed with the methods of differential geometry. The curvature is interpreted in a way specific to a cased hole. Numerical analysis gives an estimation of true vertical depth error as a function of the two independent parameters and as a function of angular deviation of the hole. The importance of this estimation is related to knowledge of the geometry of the oil-water contact that also serves as reservoir quality indicator.*

INTRODUCTION

Causes of Tilted Hole at Deep Rotary Drilling and their Classifications

Even when borehole design (construction) describes vertical deep well for oil or other industry, the actual borehole shaft will differ from the perfect vertical. Full scale modeling of the hole can be considered as a curve, starting at the point of the collar (mouth) of the well and finishing at the point of the bottom of the hole (shaft). A perfect vertical hole would mean a vertical straight line from the mouth of the well to the bottom of the well. In this case, the true vertical depth (TVD) and the length of the hole are in exact coincidence. In general, the TVD is the distance between two horizontal planes each of them intersecting one of the mentioned points. The actual hole is a real, three dimensional curve between the two points. The deviation of this curve from a straight line is the result of a number of technical, technological causes, on one hand, and of geological causes on the other hand.

The first group of causes are described[1]. Geological causes occur when the boring tool pierces rocks of changing hardness or tectonic dislocations. Among other important causes are fault zones, layer

* Petroleum Research Centre, P. O. Box 6431, Tripoli, Libya.

boundaries, boundaries of concretions, voids, karts and brachiated zones. In these cases, the tool tends to traverse along lines of least resistance. Accordingly, at layer boundaries there is a tendency for the borehole to tilt towards the normal direction of the bedding plane. As another example, there is an increased chance for having stronger deviations when the hole axis forms a relatively small angle (5^0 - 30^0) with a steeple dipping hard rock. In these cases, both the azimuth and the zenith angles of the borehole inclination may change.

Rich enough material can be found to prove that by time and by development of drilling technology, the technical-technological causes of unwanted deviations have sharply decreased[2]. In contrast, some of the geological causes of deviations are difficult to compensate by any sophisticated technology.

The geological causes can be examined in terms of their random or systematic character. This can be done from the perspective of whether or not deviation of two neighboring holes will be similar. The general gentle slope of the basin can be expected to cause systematic deviation, while voids and karts zones are likely to cause random deviations. However, the presence of faults is likely to affect the variation in such a way that the deviations obtained may have both random and systematic elements at the same time.

Importance of the Problem and Possible Different Approaches to the Solution

The problem of an improved knowledge about borehole geometry becomes important in some cases. One such case is when we have a number of wells crossing hydrocarbon (HC) reservoir and reaching the water body below the reservoir. In this case, the exact spatial position of the oil water contact (OWC) and the capillary transition zone (CTZ) has a high importance as reservoir rock quality indicator.

Indeed, the closer this surface is to a horizontal plane , the better the quality of the reservoir rock. This reservoir rock quality indicator expresses the global, overall quality of the reservoir rock in contrast to core samples having only local validity. Core drilled rock material represents always only a tiny fraction of the total reservoir volume.

When an inclination survey has been done in the hole, the spatial position of the hole can be restored exactly. Frequently, this survey data is not available. In this case, knowledge of the magnitude of the potential true vertical depth error, as a function of the deviations is of interest. Such relations can be obtained only by modeling the global geometry of the hole.

MODEL OF THE DRILLED HOLE ABD ITS MAJOR PARAMETERS

Spiral Type Curve Model of the Hole Geometry

As the drill bit moves downward, the probability that the projection of the actual bottom of the hole to the horizontal surface deviates from the mouth of the well increases. Here, the geometry of the hole is modeled in a deterministic, rather then in a stochastic way. From this, a model is suggested, whereby the side distance increases linearly with depth. This requirement prescribes that the hole model curve runs on the surface of a (narrow) cone. Also, from the point of view of this deterministic behavior, a continuous, analytical type of changes in the shape of the model curve is considered. In this way, the following definition for the hole model curve is obtained.

To define a three-dimensional curve in Cartesian coordinates is to define the $r(t) = (x(t);y(t);z(t))$ vector-scalar function.

For the spiral-type model curve of the hole, $r(t)$ is given by the following equations:

$$\begin{aligned} x(t) &= at \cdot \cos(bt) \\ y(t) &= at \cdot \sin(bt) \\ z(t) &= t \end{aligned} \qquad (1)$$

In this curve definition, a special three-dimensional spiral-type of curve is described, which contains two parameters a and b. Parameter a describes the cone, the surface of which contains the curve. Indeed, for any point of the curve, for any t value,

$$\mathbf{r}_{xy}^2(t) = x^2(t) + y^2(t) = (a \cdot t)^2$$

i.e. the distance of the curve from the z-axis is increasing by t linearly and the coefficient of the grow (speed) of radius r_{xy} is given by parameter a. This cone is refered to as the supporting cone of curve (1). The curve is somewhat similar to a helix curve but the helix curve is contained by a cylinder, rather than by a cone[3].

The geometry of the model curve is normalized, by selecting for the independent t variable of the curve the limits.

$$0 \le t \le 1 \qquad (2)$$

This places the top of the hole at the beginning of the coordinate system and the bottom of the hole to the a radius circle around the point (0,0,1) with a z-direction axis. This means from the borehole application problem point of view that TVD = 1, therefore the length unit is TVD itself. One of the major tasks is to calculate the length of the curve. The starting and finishing points of the curve given by (2), give the parameter b a clear meaning. Measuring the angle in radians and introducing the definition $b = 2\pi \cdot f$, f describes the number of rotations of the curve until it reaches the bottom level. This number is not necessarily large, and values below $^1/_2$ for f ($f \le .5$) allow the examination of a hole that has a systematic deviation direction in terms of geography (*e.g.* to the North). Figure 1 is used to demonstrate the suggested geometrical model of the hole. Here, the Cartesian coordinate system is introduced in an unusual position, but it keeps the right hand rule. This is to avoid a well sketch 'deepening' upward while using vector products of vectors, as below, without changing the right hand rule. In figure 1, both parameters a and b are exaggerated from values that are relevant for the borehole model for the purpose of representing their graphical meanings clearly.

Length, Deviation Values and Curvature of the Spiral Type Model of the Hole

To calculate the length $L_{ab}(0,1)$ of curve (1) of variable t, one needs to know the $\left\|\frac{d\mathbf{r}}{dt}\right\|$ length element, for which

$$\left\|\frac{d\mathbf{r}}{dt}\right\|^2 = \left(\frac{dx}{dt}\right)^2 + \left(\frac{dy}{dt}\right)^2 + \left(\frac{dz}{dt}\right)^2 \qquad (3)$$

relation is valid. After applying equation (3) to curve (1) *i.e.* making the calculations for the derivatives and using the basic properties of the trigonometric functions; the elementary lengths are integrated in

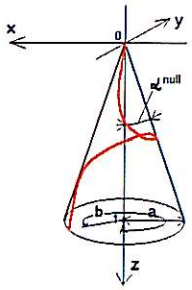


Fig. 1. Curve model for the geometery of the drilled hole.

interval (2). In this way, the length of the curve (1), $L_{ab}(0,1)$ is obtained as

$$L_{a,b}(0,1) = \int_0^1 \sqrt{(1+a^2) + a^2b^2 \cdot t^2}\, dt \qquad (4)$$

integral in equation (4) for any a, b parameters can be expressed in a closed form by primitive function only in a complex way and its numerical calculation is more feasible.

The borehole inclination angle, α in the $\mathbf{r}(t)$ point of the curve can be calculated from the scalar products of vector $\frac{d\mathbf{r}}{dt}$ and z-direction unit vector (0,0,1). On this basis, the cosine of the inclination (zenith) angle α, is calculated from equation (5).

$$\cos(\alpha) = \frac{1}{\left\|\frac{d\mathbf{r}}{dt}\right\|} = \frac{1}{\sqrt{(1+a^2) + a^2b^2 \cdot t^2}} \qquad (5)$$

α is a monotone increasing function of t. Consequently, the smallest inclination angle α is at $t = 0$, where this angle is the basic (half) angle of the supporting cone (see Fig 1.). The angle of the supporting cone can be denoted as α^{null}. For this angle, $tg(\alpha^{null}) = a$ and this equation is equivalent to that of equation (5) for the case $t = 0$. For any other $t > 0$ the $\alpha > \alpha^{null}$ relation is valid, and $\alpha^{\max}$ is reached in equation (5) at $t = 1$.

From the point of view of hole geometry, a further property of curve given by equations (1) is its Gaussian curvature, which is the local limit of angular (directional) change of the tangent vector of the curve with respect to the length of the arc. For the spatial curve $\mathbf{r}(t)$ the Gaussian scalar curvature, $\kappa(t)$ can be calculated on the basis of the formula [4]

$$\kappa(t) = \frac{\left\|[\mathbf{r}'(t), \mathbf{r}''(t)]\right\|}{\left\|\mathbf{r}'(t)\right\|^3} \qquad (6)$$

where [,] denotes the vector products of the two vectors in brackets.

For our curve, on the basis of the rule for the derivation of multiplication of functions, the first and second derivatives are

$$\mathbf{r}'(t) = \big(a \cdot \cos(bt) - t \cdot ab \cdot \sin(bt);\ a \cdot \sin(bt) + t \cdot ab \cdot \cos(bt);\ 1\big) \qquad (7)$$

$$\mathbf{r}''(t) = \big(-2ab \cdot \sin(bt) - t \cdot ab^2 \cdot \cos(bt);\ 2ab \cdot \cos(bt) - t \cdot ab^2 \cdot \sin(bt);\ 0\big) \qquad (8)$$

Substituting equations (7) and (8) into equation (6) and after tedious but elementary calculations the curvature of spiral –type hole model is given as:

$$\kappa(t)=ab\cdot\frac{\sqrt{(4+4a^2)+(1+4a^2)\cdot b^2t^2+a^2b^4\cdot t^4}}{[(1+a^2)+a^2b^2.t^2]^{3}/_{2}} \quad (9)$$

ANALYSIS OF THE CHARACTERISTICS OF THE HOLE MODEL CURVE

The importance of the curvature described by equation (9) is that while the hole inclination relates the actual direction of the hole to an external, vertical direction, the curvature describes the rate of directional change from a previous section of the hole.

In our situation for the cased hole, a special interpretation of this curvature is suggested, which corresponds to real drilling activity, as follows. Consider that the hole consists of short, exact straight sections (intervals) of uniform length jointed to each other. This arises from the assumption, that the casing tubes remain straight in the hole, and that the casing string adjusts its shape to the changing hole geometry by inclinations at the jointing of the casing tubes. Figure 2 shows the situation as described. The common length of the casing tube is denoted by p. The hole geometry is locally approximated by a tangent to the curve circle, in the plane of vectors $\mathbf{r}'(t),\mathbf{r}''(t)$, and of radius $\frac{1}{\kappa(t)}$. Here, the fact that the curvature of a section of a circle is the reciprocal of the radius of this circle is used[5]. The end points of the p length intervals are supposed to lie on this approximating circle. For the angle b what is the angle of inclination of two jointing casing tubes, using the regular polygon geometry on Fig. 2, the tangent of β/2 can be expressed as a ratio of β/2 and $\frac{1}{\kappa(t)}$. For real holes, one can not expect sharp directional changes, consequently the curvature is small and therefore; $p<<\frac{1}{\kappa(t)}$(unlike that shown from the exaggerated Fig. 2) and tg (β/2) is close to β/2 .

In this way one derives, as a special interpretation of the curvature to the cased hole, the relation:

$$\beta = p\cdot\kappa(t) \quad (10)$$

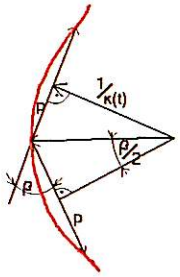


Fig. 2. Interpretation for curvature for cased hole.

As a starting point for analysis of formula (9) for the curvature, it is worthwhile to study it without the limits in equation (2). For large t tending to infinity, $k(t)$ tends to $\frac{1}{a\cdot t}$. This means that the larger the variable t, the smaller the effect of parameter b, and finally, the limit of the curvature is determined by the horizontal cross section of the supporting cone. For the case $t=0$ however, as direct calculation shows, parameter b has a large effect on the curvature, because here $\kappa(0)=\frac{2ab}{1+a^2}$.

For the case with the limits given by equation (2) for the model of the hole, the major feature of the curvature derives from the fact that for a vertical hole the deviation of the bottom of the hole from the top of the well is much smaller than the depth of the well. Expressing it with the introduced quantities, $a<<1$. Because t is limited and also b is not large in equation (9), all the terms with the multiplier a are negligible. Therefore, the denominator of equation (9) becomes 1 and one obtains for $a<<1$:

$$\kappa(t)=ab\cdot\sqrt{4+b^2t^2} \quad (11)$$

The largest curvature, and therefore according to equation (10), the largest joint deviation angle β is given by formula (11) at $t=1$.

For a real borehole A1-52 well of the Ghadames Basin of Libya where complete borehole deviation survey is available, the following data are known. The logging depth of the bottom of the hole (BHT) is 9567 feet, while side deviation of BHT is found to be 158 feet to the direction given by the azimuth angle 157° of SSE. This corresponds to a $\alpha^{mill}=.94^0$.

It should be noted that this direction is almost perpendicular to the direction of the closure of outcrop on the geological map of Libya, proving that in the Ghadames Basin which has a quiet and regular

structure of sedimentation the borehole is apt to deviate towards the normal of the bedding planes.

On the basis of the presented model and formulas, calculations can be made, whereby the possible length and borehole deviation parameters are calculated. They are calculated as a function of known or assumed major, independent parameters of the model curve of borehole a and b or what is almost the same a and f ($b = 2\pi \cdot f$). The integral in equation (4) is calculated by eight point Gaussian quadrature process, with automated selection of subintervals for integration, which provides the necessary high accuracy[6] in the range of 10^{-6}. The calculations are made by appropriate source code developed by the author and named Hole Geometry for using Fortran language[7] .

Table 1 contains the results of the calculations for the independent parameter set of a and f, which are in the range of a typical successfully drilled vertical hole. The exact meaning of the two input columns (Ic1, Ic2) as well as that of the four output columns (Oc1, Oc2, Oc3, Oc4) are written in the nomenclature type attachment belonging to the Table. In the Table all the angles are expressed in degrees (while in all the formulas of this paper angles should be used in radians), and angle β is calculated with the parameter $p = 1/50$.

The main column Oc1 is calculated from formula (4) in the above mentioned way and gives the length of the hole, which can be identified by the logging depth expressed in the introduced length unit (TVD = 1) rather than in the more regular unit feet. For the parameter range $a << 1$ in the case of the absence of the Fortran program, the following useful approximations can be derived. From formula (5) for $t = 1$, expressing $tg(\alpha)$ by $\cos(\alpha)$ one gets, . For $t = 0$, $\alpha^{max} = a \cdot \sqrt{1 + b^2}$, while from formulas (10) and (11) $\alpha^{null} = arc\ tg(\alpha^{null}) = a$ $\beta_{loc}^{max} = p \cdot ab \cdot \sqrt{4 + b^2}$.

Column Oc4 accounts for the TVD error of a well of 10000 feet TVD. The calculated TVD errors are small for the hole of a slight deviation of $1^0, 2^0, 3^0$ degree compared to the TVD of the hole. For example for $\alpha^{null} = 2^0$ and $f = .5$, i.e. for a hole that still has a general, oriented deviation, the error is 26 feet, which is small. This error is far from being negligible when the much more delicate task to determine the geometry of OWC is considered.

CONCLUSIONS

1. Assuming small angular deviation of the hole, the true vertical depth determination error is not negligible from the point of view of such a

Table 1. Calculated values of the hole model and description of their meaning

Ic1	Ic2	Oc1	Oc2	Oc3	Oc4
1.0	0.00	1.00015	1.0	0.0	2
1.0	0.25	1.00028	1.9	0.1	3
1.0	0.50	1.00065	3.3	0.2	7
1.0	0.75	1.000128	4.8	0.5	13
1.0	1.00	1.00215	6.3	0.8	22
1.0	2.00	1.00811	12.3	3.2	81
2.0	0.00	1.00061	2.0	0.0	6
2.0	0.25	1.00111	3.7	0.2	11
2.0	0.50	1.00261	6.6	0.5	26
2.0	0.75	0.00510	9.5	1.0	51
2.0	1.00	1.00857	12.4	1.7	86
3.0	0.00	1.00137	3.0	0.0	14
3.0	0.25	1.00250	506	0.2	25
3.0	0.50	1.00587	9.8	0.7	59
3.0	0.75	1.01143	14.0	1.4	114

Ic = Input column
Oc = Output column

Ic1	angle	α^{null}	°, degree	Angle of the supporting cone. $tg(\alpha^{null}) = a$
Ic2	number	f	rotation hole	Rotation number of the around its axes. $b = 2\pi \cdot f$
Oc1	length	$L_{ab}(0,1)$	unit	Length of the hole, while true vertical depth of the bottom of the hole is 1 length unit (formula (4))
Oc2	angle		α^{max}	°, degree Maximum deviation of the hole from vertical (formula (5) at $t = 1$)
Oc3	angle		β_{loc}^{max}	°, degree Maximum angle of casing joints. calculated from the maximum hole curvature with the casing length parameter, $p = 1/50$ (formula (9) and (10) at $t = 1$)
Oc4	abs.err.	Δz	feet	Absolute error of true vertical depth determination for a well of 10.000 feet

demanding task like OWC determination and reservoir scale reservoir rock characterization.
2. True vertical depth determination can be fully established only by using borehole deviation survey.
3. In case of having well established geological, petrophysical criteria, this criteria should be enhanced over seemingly exact depth data.

REFERENCES

[1] Maximov A., Miloserdina G., Ermin N., 1973. Short Course of Geological Prospecting and Exploration. Mir Publisher, Moscow (in English)

[2] Brantly J. E., 1971. *History of Oil Well Drilling*. Gulf Publishing Company.

[3] Gray A., 1997. The Helix and its Generalization, par. 8.5, pp. 198-200 in *Modern Differential Geometry*. CRC Press, Boca Roton, FL.

[4] Prohorov J.V., 1988. Mathematical Encyclopedia. Soviet Encyclopedia, Moscow (in Russian)

[5] Borowski E. J., J.M., Borwein J.M., 1989. *Dictionary of Mathematics*. Harper Collins Publishers.

[6] Dmitriev V. I., 1982. *Numerical Mathematics and Computers in Geophysical Exploration*. Paragraph 20. Publisher 'Nedra', Moscow. (in Russian)

[7] Microsoft Corporation, 1993. Fortran Power Station, Language Guide.

Petroleum Res. J. Vol. 16 (2004); P. 43–52, 15 Figs.

Validation of Theoretical Coning Models Using Numerical Single-Well Simulation

Salem M. Alakhdar*, Abdelhameed A. Urayet** and Mabrouk A. Benrewin**

صلاحية النموذج النظري لتشكل مخروط الماء باستخدام تشبيه رقمي لبئر فردية

سالم الأخضر وعبد الحميد وريث والمبروك بن روين

يعتبر تشكل مخروط الماء من المشاكل التشغيلية الحادة في المكامن النفطية المنتجة بقوة دفع الماء التحتي. وفي ليبيا، يوجد عدد كبير من الحقول النفطية التي تعاني من ظاهرة تشكل مخروط الماء. ويراعي عند الانتاج، من هذه الحقول، الحد الأدنى (الحد الحرج) لمنع فرصة تشكل مخروط الماء من الحدوث. ونظراً لأن مثل هذه المعدلات تعتبر ضئيلة (وغير إقتصادية)، فإن الشركات عادة، لتفادي مثل هذه الظاهرة، ما تبقى على معدلات الانتاج العادية، وفي هذه الحالة يصبح من الضروري تقدير زمن وصول المخروط المائي لخرم الانتاج السفلية (زمن الاختراق) وذلك من خلال إعداد تصور لسلوك الماء المستقبلي الكفيل بإعداد التصاميم المناسبة لتجهيزات الانتاج السطحية.

لقد تم تطبيق بعض المقارنات المنشورة في المسائل التي تناولت توقعات الحد الحرج للإنتاج وزمن الاختراق وسلوك نسبة الماء، وذلك لمعلومات فعلية من ثلاثة آبار ليبية.

كما تم إنشاء نموذج لبئر ثنائي الأبعاد (2D) وبشكل شعاعي لآبار مختارة، وقورنت معلومات هذا النموذج مع معلومات الأداء الفعلية ونتائج المقارنات.

وبالتأكيد، فإن هذه الدراسة أوضحت أن بعض المقارنات الرقمية لها مصداقية أكثر من البعض الآخر. كما أن الدراسة تقر بإمكانية وضع سلوك تشبيهي لتشكل المخروط المائي لإعطاء نتائج أفضل، إلا أن قلة وقصور المعلومات المتعلقة بوصف المكمن والنفاذية العمومية، وعموماً قصور معلومات تحاليل العينات اللبية الخاصة وكذلك التوثيق، تساهم في تدني كفاءة النتائج المقتبسة من النماذج الرقمية، وعلى الأخص في الأحيان المتأخرة.

وأخيراً، تستهدف هذه الدراسة وضع إجراءات مناسبة لتحليل ظاهرة تشكل مخروط الماء في المكامن. وبالرغم من أن الدراسة اعتمدت على معلومات فعلية لثلاثة آبار، إلا أن فكرة توسيعها لعدد أكبر من الآبار والطبقات مازال قائماً، وذلك بهدف إثبات صحة نتائج النماذج من عدمه.

Abstract: *Water coning is often a serious operational problem in oil reservoirs producing with strong bottom water drive. In Libya, many of the oil fields have water coning problem. The production from such fields would normally consider limitation of the production rate to a certain minimum (critical rate) to prevent water cone from happening. However, since such a rate is normally very small (i.e. not economical), the company will be producing at a higher rate, and it becomes essential to estimate the time required for the water cone to reach the lower perforations (i.e. breakthrough time), and to predict the water*

* Petroleum Research Centre, P.O. Box 6431, Tripoli, Libya.
** Petroleum Engineering Dept., Al Fateh University, Tripoli, Libya.

performance afterwards to make the proper design for the surface facilities.

Some of the published correlations for predicting the critical oil rate, breakthrough time, and water cut performance were applied to actual well data from three Libyan wells. Also, a single well 2D radial model was constructed on selected wells. The model results were compared to the actual field performance as well as to the correlations results.

This study shows clearly that some of the empirical correlations can be considered more reliable than the others. It also, shows that even though simulation of water coning is possible, and give more reliable results, however, the lack of data (i.e.good reservoir description, lack of vertical permeability data on a layer basis, lack of a reliable special core analysis, and improper documentation of work-overs) will always limit the validity of the coning results obtained by the numerical models especially at late times.

Finally, this study is mainly aimed to set up the proper procedure of analyzing the water coning phenomena. Since the study considers the actual field data of only three wells, it should be expanded to a larger number of wells producing from different formations to confirm (or disconfirm) the results and conclusions of this study.

INTRODUCTION

Water coning is a serious problem in many oil field applications. It is the mechanism responsible for the rise of bottom water through the oil zone to the producing interval. The production of coned water will reduce oil production significantly. Therefore, accurate estimate of the break-through time and the water cut performance afterwards is of extreme importance in reservoir development and management.

Theoretical and Experimental Literature Review:

Many authèrs have offered solutions for the steady state watèr coning problem. The first of these was presented by Muskat[1], in 1937. He presented an approximate solution based on many assumptions such as, single-phase (oil) potential distribution around the well at a steady-state conditions which is described by the solution of Laplace's equation for incompressible fluid; uniform flux boundary condition at the well, and the potential distribution in the oil phase is not influenced by the cone shape.

Arthur[2] developed a set of charts to solve the water coning problem, based upon Muskat's treatment. He showed that the vertical thickness of the two fluids below the wellbore is very important, with coning occuring with decreasingly smaller drawdowns, as the distance between the well and the coning fluid shortens. Analysis of his charts lead to the conclusion that coning is greatly restricted by small lenses of reatively low permeability directly below the bottom of the well, since they greatly distort the potential gradients in the sand.

Chaney *et al.*[3] developed a set of curves from which critical flow rates can be determined at various lengths of perforations. This method is an extension of Muskat's work and based upon the results of mathematical and potentiometric analysis of water coning.

Chierici *et al.*[4] utilized a large potentiometric model of the electrolyte tank type, which was used to determine the maximum water-free oil production rate for a given perforated interval.

Meyer and Garder[5] analytically determined the maximum allowable flow rate of oil into a well without water zone coning into the production section of the well.

Schols[6] presented an emperical critical rate correlation for partially penetrating wells. This relation is based on laboratory experiments and supplemented by a number of mathematical simulations. In Hele-shaw model, the steady state flow of segregated fluids in porous media in a two dimensional, radial flow configuration is simulated.

Chaperon[7] provided a simple and practical estimate of the critical rate to be expected without water zone coning into the production section of the well. This estimate is based on a numerical model results.

Sobocinki and Cornelius[8] give an emperical correlation for predicting water coning breakthrough time based on laboratory data and computer program results. Their experimental laboratory studies were conducted with a pie-shaped, sand-packed plexiglass model. The correlation involves dimensionless groups of reservoir and fluid properties, production rate, and well characteristics.

Bournazel and Jeanson[9] developed a new method combining experimental correlations using dimensionless numbers for estimating breakthrough

time with a simplified analytical approach based on the assumptions that the front shape behaves like a current line, in an equivalent model of different shape. Conversely, this method can be used for approximately determining the optimum completion and withdrawal rate.

Kuo and DesBriasy[10] presented a correlation for the prediction of water cut performance in a bottom water drive reservoir. Numerical simulation was used to determine the sensitivity of water coning behaviour to various reservoir parameters. They published an equation that accurately reproduces the graphical water coning breakthrough time results of Sobocinki and Cornelius[8]. It is important to note that this correlation was developed using straight line relative permeability curves.

MODEL DESCRIPTION

The data used in the analysis included actual field data from three Libyan oil wells (wells A-06 and A-21/ Bahi Field-Courtesy of Waha Oil Company, Tripoli, Libya, and well B-15/ Sharara Field-Courtesy of REPSOL, Tripoli, Libya).

Average horizontal permeability was obtained from pressure build-up and productivity index tests. The horizontal permeability distribution for each layer in the model was determined from core data.

As a starting point, the initial vertical permeability values were obtained from plots of horizontal versus vertical permeability from core data.

Individual well production rates (oil and water) were collected. Whenever the production rates were realtively constant, the model used an average rate over these time periods to minimize calculation times.

Since there was no data provided for the aquifer thickness except that it is a very thick aquifer, consequently, the single well models used an aquifer thickness of 1000 feet.

All the required well data, rock properties per layer, fluid properties, and special core analysis data for the three different wells are shown in Tables A3-A6 in appendix-A.

Model-1 (Well A-06)

This model consists of 10x1x21 homogeneously parameterized radial gridblocks. This well is in the south-central part of Bahi Field. The well was put on production in April 1970. The pay zone is relatively thick (95 ft). The present water cut has reached 60%. Thickness of the vertical layers for the model and the initial oil-water contact were obtained from well logs.

Model-2 (Well A-21)

This model consists of 10x1x15 homogeneously parameterized radial gridblocks. This well is in the western area of Bahi Field. The well was put on production in February 1970. The water cut rose very sharply from 0 to 35% during the first year of production. The pay zone is reatively thick (95 ft).

Model-3 (Well B-15)

This model consists of 10x1x15 homogeneously parameterized radial gridblocks. This well is in the east-central part of Elsharara Field. The well was put on production in April 1998. The water cut increase was very slow during the first year of production. Then, the water cut had a sharp increase from 0.07 to 36% afterwards.

RESULTS

1. Theoretical Correlations:

Critical Rate Correlations

The results obtained for wells A-06, A-21, and B-15 using Meyer and Garder[6], Chaney *et al.*[3], Schols[6], and Chaperon[7] correlations are shown in Table 1. The results show that the critical rates vary widely for each well. However, in all cases, the calculated critical rates are very low and would be un-economical for Libyan fields.

Table 1. Critical oil flow rates

Theoretical Correlations	Critical Oil Rate, BPD		
	Well: A-06	Well: A-21	Well: B-15
Meyer and Garder	12	2	26
Chaney, Nable, Henson and Rice	44	6	83
Schols	23	3	49
Chaperon	5	0	51

Breakthrough Time Correlations

The two correlations used are the Sobocinki and Cornelius[8], and Bournazel and Jeanson[9] . The results are shown in Table 2.

Table 2. Breakthrough time

Theoretical Correlations	Breakthrough time (Days)		
	Well: A-06	Well: A-21	Well: B-15
Sobocinki and Cornelius	1697	305	1458
Bournazel and Jeanson	750	150	600

The Breakthrough time plots representing well A-06, A-21, and B-15 are shown in figures 1, 2, and 3 in appendix-B.

Two major conclusions can be easily drawn from these plots; first that Bournazel and Jeanson[9] correlation give normally a good estimate for the actual Breakthrough time as can seen from figures 1 and 3. Second, that the breakthrough time estimated by Sobocinki and Cornelius[8] correlation is very optimistic (at least twice the actual time) and consequently should not be depended on in production forecasts.

Water Cut Correlation

Kuo and DesBrisay[10] developed simple equation for water cut performance prediction, and simple material balance equations were used to predict the location of the oil-water contact. This correlation was compared to the numerical results of water cut performance after breakthrough for the three wells as shown in figures 4, 5, and 6 in appendix-B.

Kuo and DesBrisay[10] gives a good water cut performance prediction for well A-06 from the time of breakthrough (2 years) to more than 10 years. Afterwards, the correlation would be inaccurate due to systematic shut-downs (causing water cone to move down), lowering of production rates, and workovers which prohibit the use of the correlation effectively.

The correlation also gives a good water cut prediction for well A-21 for the first

three years of production, Afterwards, long periods of shut-downs and reduced rates prohibit the effective used of the correlation.

Finally, the corrrelation also gives a good water cut performance prediction for well B-15 throughout the short history of the well. The water cut increase trend is maintained by the correlation inspit of the average difference of < 20% between the actual data and the correlation estimates.

Consequently, it can be concluded that Kuo and DesBrisay[10] give in general a good prediction of the water cut performance after breakthrough provided that minimum human interference in the form of reducing rates, prolonged shut-in periods, or re-preforating is applied to the oil well.

2. Single Well Model:

The 2D radial numerical model was constructed using Eclipse-100 black-oil simulator. Every well has different grid system depending on the geologic layers. Also, in the Z-direction, the number of cells for each well was varied with the objective of keep ΔZ as small as possible in order to minimize the effect of numerical dispersion if any.

Since the problem here is to study the vertical water movement (*i.e.* water coning), history matching was achieved by changing two main influencing parameters which are the Relative Permeability Curves, and the Absolute Permeability Values. Since Bournazel and Jeanson[9] correlation gave a good estimate for the actual breakthrough time, it was decided to maintain the end points of the relative permeability curves, and to restrict the changes to the shape of the curves for the three different wells. The horizontal permeabilities were first modified in order to obtain the actual flow rates reported for each well, then the vertical permeabilities for each layer were modified based on values calculated from core data.

Model-1 (well A-06)

Several history match runs were made. The water cut history calculated by the model is compared to the actual water cut history. As can be seen from figures 7 and 8 in appendix-B, there is excellent agreement between the observed and simulated water cuts for the first 10 years. Afterwards, it was not possible to obtain a good history match (Fig. 8). Many factors could be causing such divergence: either the changes incorporated in the relative permeability curves are not accurate at high water saturations since the water curve increases exponentially in most cases, or because the input of the workovers was not accurate, or because the reducing and shutting of the well for a prolonged periods of time affects the wettability (and consequently the relative permeability curves) which can not be included in the model.

Model-2 (well A-21)

Similar to the performance of well A-06, there is excellent agreement between the observed and

simulated water cuts for the first three years as shown in figure 9 in appendix-B. Afterwards, it was not possible to obtain a good history match (Fig. 10 in appendix-B). Same factors mentioned earlier for well A-06 could be causing divergence at late times. These factors include incorrect changes incorporated in the relative permeability curves, improper input of workovers, or the shutting of the well for a prolonged periods of time creating wettability changes which can not be included in the model.

Model-3 (well B-15)

After several history match runs, a good agreement between observed and simulated water cuts as shown in figures 11 and 12 in appendix-B. The average deviation of 20% in the calculated values is most properly due to incorrect changes in the end points of the relative permeability curves.

Final Comparison

A final comparison of the actual breakthrough time and water cut performance to the results calculated using the theoretical correlations and the simulated coning model is shown in figures 13, 14, and 15 in appendix-B for the three wells respectively.

The comparison clearly indicates the following:

- The single well numerical model would always give more reliable matching for water cut performance than the emperical correlations available in the literature.
- Some emperical correlations can be considered more reliable than the others. For example, good identification for the time of breakthrough can be obtained using Bournazel & Jeanson[9] correlation, whereas a good identification of the general trend of the water cut increase can be obtained using Kuo and DesBriasy[10] correlation.
- Production at very high oil rates with high water production rates can be problematic in predicting water cut performance by theoretical correlations as well as by single well simulation modeling.

CONCLUSIONS AND RECOMMENDATIONS

1. Coning Correlations

The theoretical correlations discussed in this study were applied to three Libyan oil wells in order to rapidly evaluate the water coning performance parameters (*i.e.* critical rate, breakthrough time, and water cut performance after B.T). The main conclusions are:

Critical Rate

- The different mathematical correlations available in literature vary widely in their estimate of the critical rate value.
- The Chaney et al[3] correlation gives always the highest estimate for the critical rate.
- In all studied wells, and using any of the available mathematical correlations, the calculated critical rates will be very low and would be uneconomical for Libyan fields.

Breakthrough Time

- The Bournazel and Jeanson[9] correlation gives normally a good estimate for the actual breakthrough time, whereas, the Sobocinki and Cornelius[8] correlation would always give very optimistic results (at least twice the actual time) and consequently should not be applied in production forecasts.

Water cut Performance

- The Kuo and DesBrisay[10] correlation give, in general, good prediction of the water cut performance after breakthrough provided that minimum human interference in the form of reducing rates, prolonged shut-in periods, or re-perforating is applied to the oil well.

In general, the study clearly indicates that the use of the mathematical correlations should be limited to rough estimates of breakthrough time or water cut performance, in case of project costs or limited well data do not allow the more reliable single well modeling.

2. Coning Numerical Model

The main conclusions obtained from the single well simulation are:

- The history matching indicates a good match for the first period of production (until few years after breakthrough time or as long as the water cut is relatively small, *i.e.* > 50%).
- The single well simulation model was not able to give a good match for the water cut performance

at late times, in spite of all the changes made in the petrophysical properties (horizontal and vertical permeabilities), and in the shape and end points of the relative permeability curves.

• Most probably, the inability to obtain a good history match at late times was due to:

1 - Using a single set of relative permeability curves to represent the whole thickness of the oil zone. It is clear that to obtain a good match, it is necessary to have a set of relative permeability curves for each layer in the oil zone. Normally, this is not available for any one single well.

2 - The frequent shut-in of the wells for prolonged periods might have created changes in the wettability characteristics of the rock and most certainly have changed the shape of the relative permeability curve with time for each single layer.

In general, the single well numerical model would always give more reliable matching for the water cut performance than the empirical correlations available in the literature. However, reliability of the model will be highly dependent on quantity of data available (especially, good layer-by-layer description in terms of vertical and horizontal permeabilities and relative permeability curves). Also, even when a good history match is obtained, the validity of the model will be declining with time with continuing fluctuations in the production and frequent shutting down of the well.

ACKNOWLEDGEMENTS

The authors of this study are very grateful to Dr Bourima Belgasem, the General Manager of Petroleum Research Centre for his unlimited support. Also thanks goes to Waha Oil Company and REPSOL Oil Operations for their great helpful and permission to publish this paper.

REFERENCES

[1] Muskat, M., 1937. The flow of homogeneous fluid through porous media. Boston, Massachusetts: *International Human Resources Development Corporation.*

[2] Arthur, M. G., 1944-1945. Fingering and coning of water and gas in homogeneous oil sand. *Transactions of the AIME.*

[3] Chaney, P. E., Noble, M. D., Henson, W. L. and Rice, T. D., 1956 (May). How to perforate your well to prevent water coning , *OGI*, p. 108.

[4] Chieirici, G. L. and Ciucci, G. M., 1964 (August). A systematic study of water coning by potentiometric models. *JPT*, 923-929.

[5] Meyer, H. I. and Garder, A. O., 1954 (November). Mechanics of two immicible fluid in porous mdeia. *Journal Applied Physics*, **25**. No. **11**, 1400.

[6] Schols, R. S., 1972(January). An emperical formula for the critical oil production rate. *Erdoel Erdgas*, Z., **88**, No. **1**, 6-11.

[7] Chaperon, I., 1980. Theoretical study of coning toward horizontal and vertical wells in anisotropic formation, subcritical and critical rates", SPE 15377, *SPE Annual San Orleans.*

[8] Sobocinski, D. P. and Cornelius, A. J., 1965 (May). A correlation of predicting water coning time. *JPT*, 594-600.

[9] Bournazel, C. and Jeanson, B., 1971 (October). Fast water coning evaluation method. SPE 3628, 46th *SPE* Annual New Orleans.

[10] Kuo M.C.T. and DesBrisay C.L., 1983(October). A simplified method for water coning predictions. *SPE* 12067, 58th SPE Annual San Fransisco.

Appendix-A

Table A 3. Rock properties

	Well A-06	Well A-21	Well B-15
Rock compressibility, psi^{-1}	$5.1x10^{-6}$	$5.1x10^{-6}$	$4.3x10^{-6}$
Porosity, fraction	0.26	0.26	0.11

Average porosity and permeability for individual layers:

Well A-06

Layer	Top s.s.	Base s.s.	Average porosity fraction	K md	h ft	md Kv
1	2590	2615	0.260	6	25	4
2	2615	2639	0.263	16	24	6
3	2639	2663	0.278	44	24	11
4	2663	2705	0.267	62	22	10

Well A-21

Layer	Top s.s.	Base s.s.	Average porosity fraction	K md	h ft	md Kv
1	2625	2664	0.200	187	39	79
2	2664	2701	0.260	204	37	81
3	2701	2716	0.268	349	15	83

Well B-15

Layer	Top s.s.	Base s.s.	Average porosity fraction	K md	h ft	md Kv
1	2971	3031	0.11	1152	60	205

Table A 4. Reservoir fluid properties

Oil properties:

Well: A-06 and A-21

P(psia)	Bo (RB/STB)	Rs(SCF/STB)	m_o(cp)
2015	1.176	221	1.12
1315	1.182	221	1.06
1015	1.184	221	1.03
715	1.187	221	1.00
515	1.189	221	0.99
315	1.190	221	0.986
267	1.1909	221	0.98
231	1.191	213	1.00
189	1.183	202	1.02
141	1.177	189	1.05
97	1.166	170	1.07
72	1.159	155	1.09
58	1.151	142	1.12
49	1.144	130	1.42
15	1.051	0	1.86

Well: B-15

P(psia)	Bo (RB/STB)	Rs(SCF/STB)	m_o(cp)
1996	1.084	30	0.82
1570	1.088	30	0.79
1059	1.093	30	0.75
730	1.113	30	0.72
605	1.098	30	0.71
354	1.101	30	0.69
280	1.118	30	0.68
220	1.118	30	0.68
154	1.103	30	0.68
143	1.19	30	0.68

Water properties:

	Well A-06 and A-21	Well B-15
Viscosity, cp	0.54	0.54
Compressibity, psi^{-1}	$2.77x10^{-6}$	$3.4x10^{-6}$
Density, g/cc	1.0284	1.0284

Table A 5. Well data

	Well A-06	Well A-21	Well B-15
Well type	Pumping	Pumping	Pumping
Total depth, ft (s.s.)	5051	2716	5000
Completed in layer	1,2,3,4	1,2	1
Driving mechanism	Bottom water	Bottom water	Bottom water
Skin	0.0	0.0	0.0
Starting production	1/4/1970	1/2/1970	12/4/1998
OBHP, psia	1188	1188	1996
OOWC, ft (s.s.)	2699	2701	3048

Table A 6. Saturation functions

Well: A-06

S_w	K_{rw}	K_{ro}	P_{cow}
0.29	0.000	0.780	0
0.40	0.050	0.260	0
0.50	0.108	0.085	0
0.60	0.199	0.015	0
0.70	0.337	0.000	0
0.80	0.529	0.000	0
0.90	0.789	0.000	0
1	1.000	0.000	0

Appendix-A (*Cont.*)

Well: A-21

S_w	K_{rw}	K_{ro}	P_{cow}
0.36	0.000	0.800	0
0.46	0.040	0.38	0
0.50	0.065	0.250	0
0.55	0.090	0.165	0
0.60	0.120	0.100	0
0.65	0.165	0.065	0
0.70	0.210	0.030	0
0.80	0.350	0.005	0
0.9	0.620	0.000	0
1	1	0.000	0

Well: B-15

S_w	K_{rw}	K_{ro}	P_{cow}
0.110	0.000	1.000	0
0.125	0.000	1.000	0
0.140	0.000	1.000	0
0.188	0.008	0.467	0
0.261	0.018	0.265	0
0.356	0.042	0.120	0
0.453	0.080	0.048	0
0.548	0.132	0.016	0
0596	0.166	0.010	0
0.645	0.200	0.004	0
0.740	0.287	0.000	0
0.870	0.644	0.000	0
1.000	1.000	0.000	0

Appendix-B

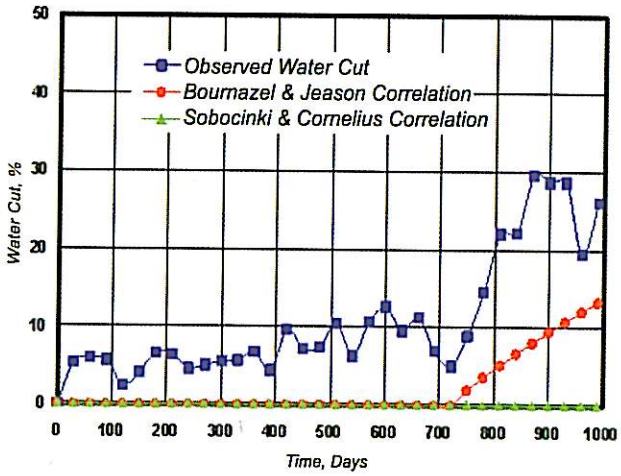


Fig. 1. Breakthrough time (theoretical correlations), well A-06.

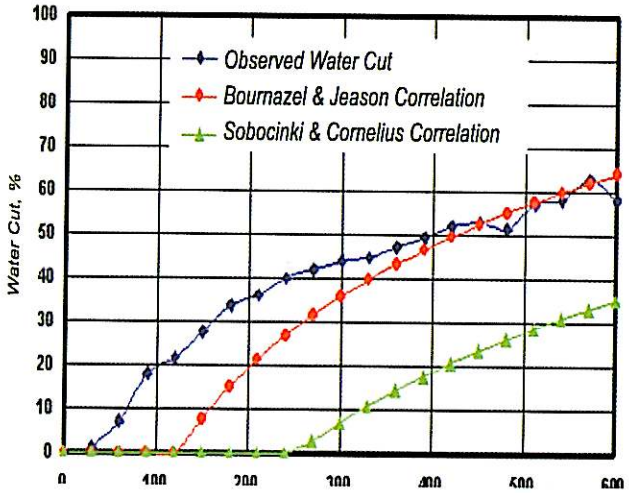


Fig. 2. Breakthrough time (theoretical correlations), well A-21.

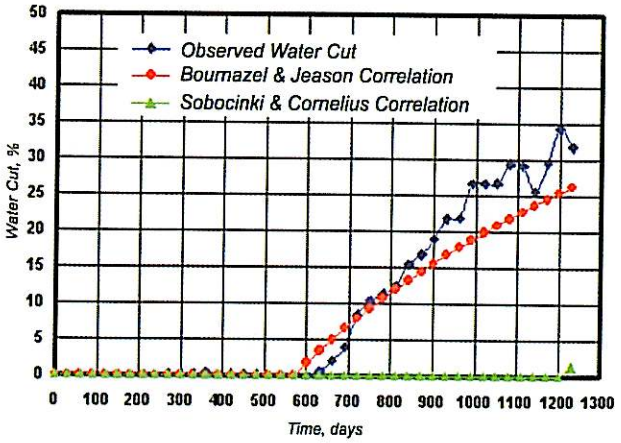


Fig. 3. Breakthrough time (theoretical correlations), well B-15.

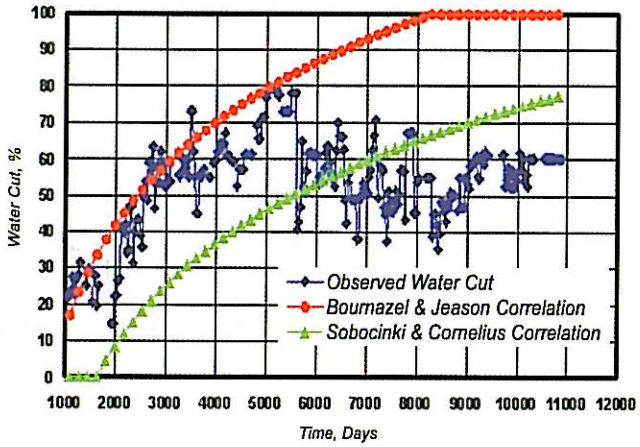


Fig. 4. Water cut performance using (Kuo and Desbrisay correlation) after breakthrough time calculated by Bournazel and Jeanson and Sobocinski and Cornelius correlarions, well A-06.

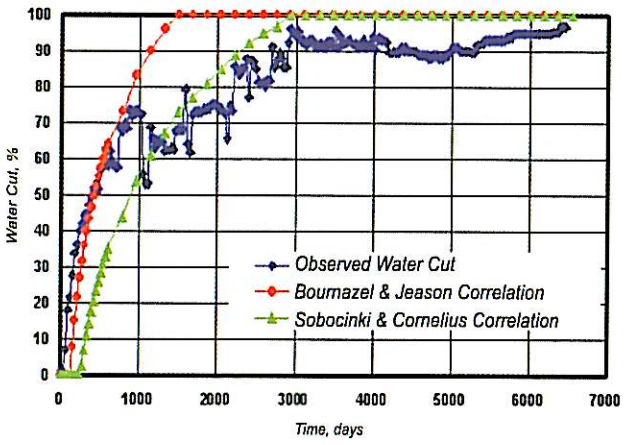


Fig. 5. Water cut performance using (Kuo and Desbrisay correlation) after breakthrough time calculated by Bournazel and Jeanson and Sobocinski and Cornelius correlarions, well A-21.

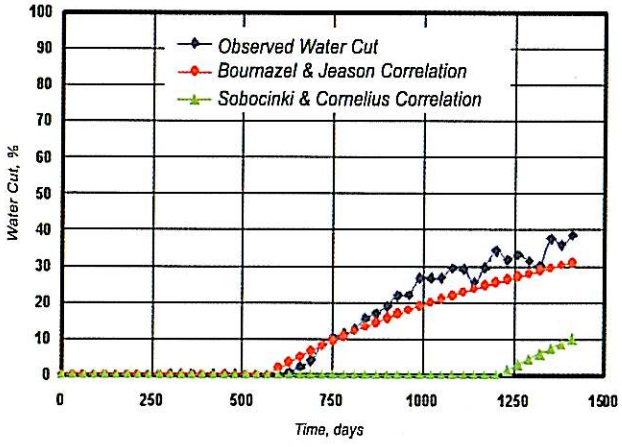


Fig. 6. Water cut performance using (Kuo and Desbrisay correlation) after breakthrough time calculated by Bournazel and Jeanson and Sobocinski and Cornelius correlarions, well B-15.

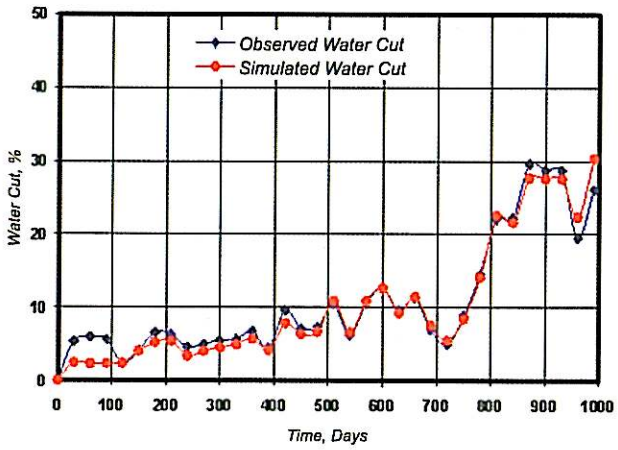


Fig. 7. Breakthrough time (simulation model), well A-06.

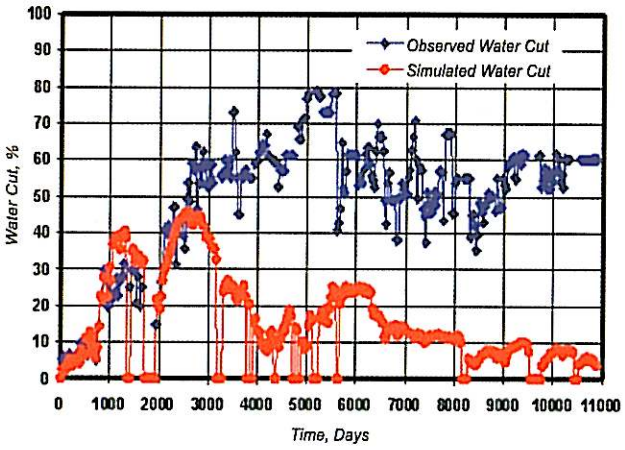


Fig. 8. Water cut performance after breakthrough, (simulation model), well A-06.

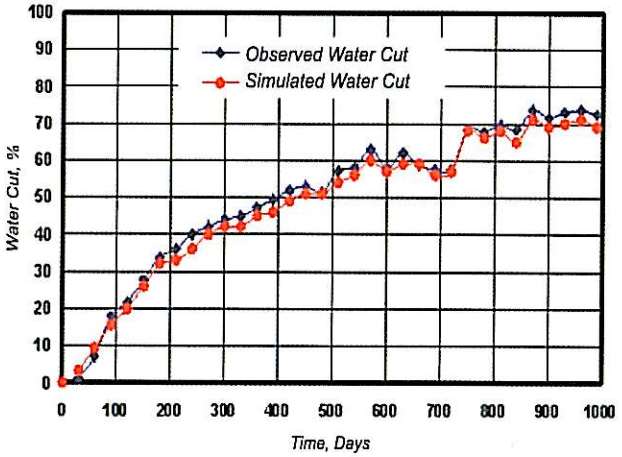


Fig. 9. Breakthrough time (simulation model), well A-21.

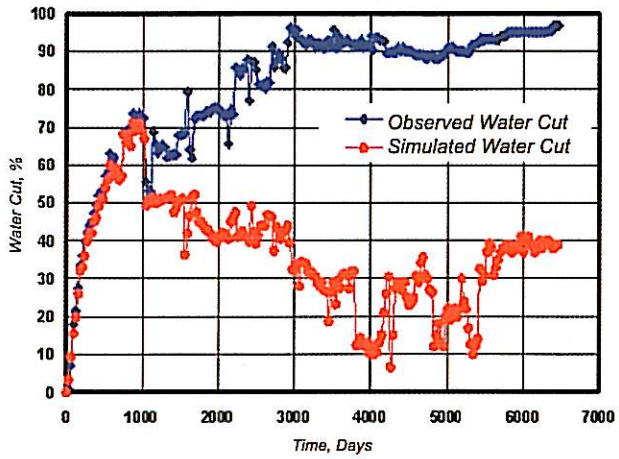


Fig. 10. Water cut performance after breakthrough, (simulation model), well A-21.

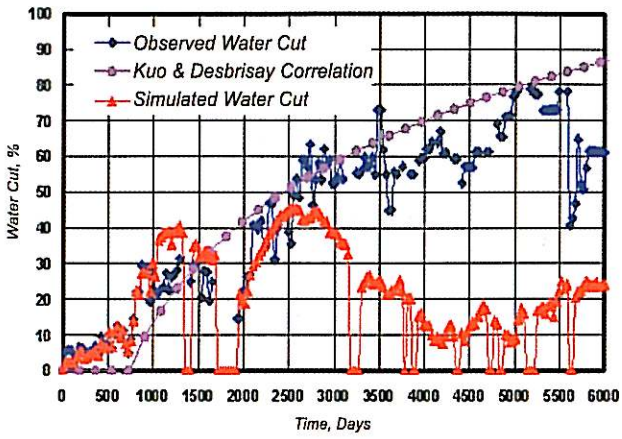


Fig. 13. Water cut performance prediction (theoretical and simulation model), well A-06.

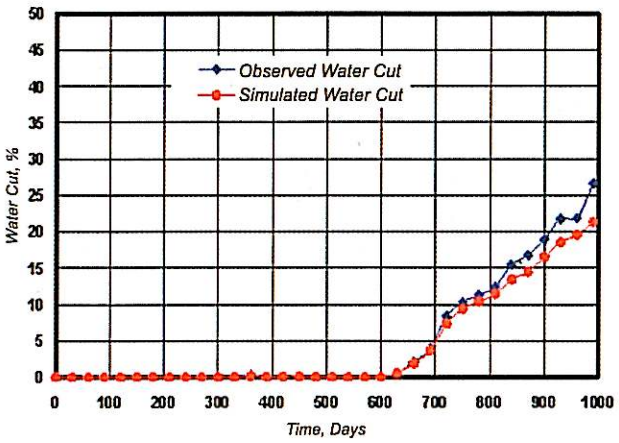


Fig. 11. Breakthrough time (simulation model), well B-15.

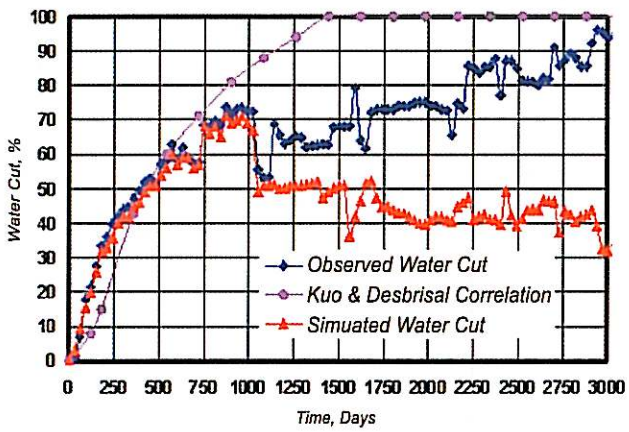


Fig. 14. Water cut performance prediction (theoretical and simulation model), well A-21.

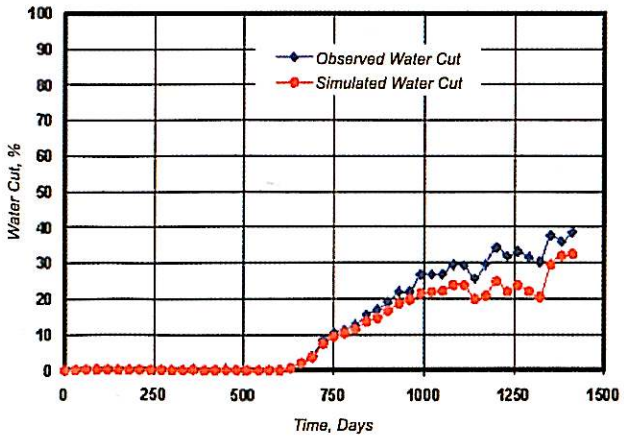


Fig. 12. Water cut performance after breakthrough, (simulation model), well B-15.

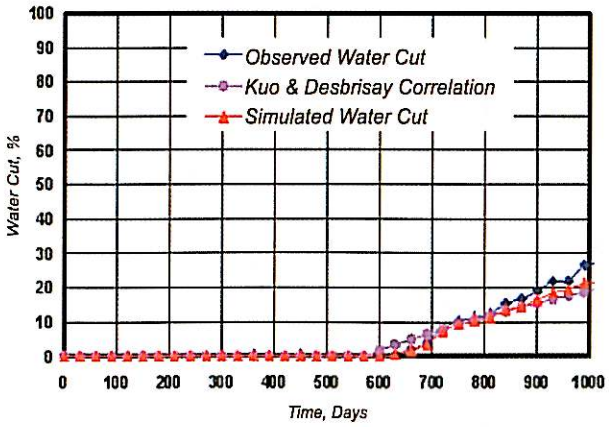


Fig. 15. Water cut performance prediction (theoretical and simulation model), well B-15.

Petroleum Res. J. Vol. 16 (2004); P. 53–56.

Modified Approach to Calculate Water Influx (Unsteady State)

Jawad Radhi R. Al-Assal*

طريقة معدلة لحساب تدفق الماء غير المستقر

جواد راضي العسل

تم في هذه الورقة وباستعمال طرق مختلفة[4,3,2] حل مثالين لحساب تدفق الماء غير المستقر من كتاب أساسيات الهندسة النفطية[1] بهدف توضيح أن معادلات Marsal مازالت في حاجة إلى بعض التحوير في الثوابت حتى تتوافق مع الحل الأصلي لـ Van Everdingen وHurst. إن هذه التعديلات غير ثابتة ولكنها تعتمد على المدى لقيم t_{ED}، t_D.

Abstract: *In this paper two examples for the calculation of water influx from Ref [1] are resolved using different techniques (Van Everdingen and Hurst[2], Fetkovich[3], Marsal[4] in order to demonstrate that Marsal Equations need some modification on the constants in order to be more consistent with the original solution of Van Everdingen and Hurst[2]. These modifications are not constant but are function of the range of r_{eD} and t_D.*

INTRODUCTION

A great number of papers were written about the subject of water influx calculations in unsteady state for radial and linear flow; so there is no need to go in detail about the theory of this subject .

The unsteady state influx theory of Van Everdingen and Hurst is used to calculate the cumulative water influx, under practically all circumstances, for radial and linear aquifers. Unfortunately, it has the disadvantage that the calculations are rather tedious due to the complexity of superposing solutions for each time step, also it requires tables of We_D and t_D.

Fetkovich tried to avoid or remove the necessity of superposition in theVan Everdingen and Hurst method .However it is used for limited aquifers only. Also it is initially still necessary to apply the unsteady state influx theory of Van Everdingen and Hurst for the first few time steps.

Marsal has shown that the Van Everdingen and Hurst tables of We_D and t_D can be fairly well approximated by the infinite radial unit function up to a dimensionless time of $t_D = 0.4\,(r_{eD} - 1)^2$. He used analytical expression to calculate the dimensionless water influx (W_{eD}).

The modified approach used almost the same analytical expression of Marsal but with slight modifications on the constants and there are some constrains on the values of r_{eD} and t_D.

THE MODIFIED APPROACH

Marsal has shown that the Van Everdingen and Hurst tables of We_D and t_D can be fairly well approximated by the infinite radial unit function up to a dimensionless time of $t_D = 0.4\,(r_{eD} - 1)^2$ .....(1)

The approximating function can be written in the following form:

$$W_{eD} = 0.5\,(r_{eD}^2 - 1)\,[1 - \exp(-2\,t_D / j^*)] \quad .....(2)$$

Where :

$$j^* = r_{eD}^4\,\ln(r_{eD})\,/(r_{eD}^2 - 1) + 0.25\,(1 - 3\,r_{eD}^2) \quad ....(3)$$

* Senior staff of reservoir eng. Sirte Oil Company ,Libya.

$$t_D = 2.309kt / \Phi\mu_w c_t r_o^2 \quad \text{.....(4)}$$

$$r_{eD} = r_e / r_o \quad \text{.....(5)}$$

The dimensionless time and aquifer constant for finite radial aquifers are defined as for infinite radial aquifers.

Applications of the above equations on the examples in Ref [1] gave some deviation from the results obtained using method of Van Ever and Hurst, especially for large value of re_D. So trial and error was used on the constants in the above equations and some constrains were put on the values of re_D and t_D as follow:

For $r_{eD} <= 6$ then

$$j^* = r_{eD}^4 \ln(r_{eD}) / (r_{eD}^2 - 1) + 0.245 (1 - 3 r_{eD}^2) \quad \text{.....(6)}$$

For $r_{eD} > 6$ then

$$j^* = r_{eD}^4 \ln(r_{eD}) / (r_{eD}^2 - 1) + 0.3071 (1 - 3 r_{eD}^2) \quad \text{.....(7)}$$

For $t_D <= 10$ then

$$W_{eD} = 0.5 (r_{eD}^2 - 1) [1 - \exp(-2.2 t_D / j^*)] \quad \text{.....(8)}$$

For $10 < t_D <= 20$ then

$$W_{eD} = 0.5 (r_{eD}^2 - 1) [1 - \exp(-2.15 t_D / j^*)] \quad \text{.....(9)}$$

For $t_D > 20$ then

$$W_{eD} = 0.5 (r_{eD}^2 - 1) [1 - \exp(-1.875 t_D / j^*)] \quad \text{.....(10)}$$

Table 1. Input data

Time (years)	t_D	Pressureat o.w.c (psia)	$We_D(r_{eD}=10)$	$We_D(r_{eD}=5)$
0	0.00	2720 (p_i)	0.00	0.00
1	5.67	2500	4.95	4.88
2	11.34	2290	8.12	7.46
3	17.01	2109	10.90	9.10
4	22.68	1949	13.50	10.09
5	28.35	1818	15.90	10.83
6	34.02	1702	18.10	11.27
7	39.69	1608	20.20	11.52
8	45.36	1535	22.20	11.69
9	51.03	1480	24.00	11.81
10	56.70	1440	25.70	11.89
h = 100 ft, k = 200 md, r_o = 9200 ft., $c_w = 3.x\ 10^{-6} psi^{-1}$, $c_f = 4.x10^{-6} psi^{-1}$, f = 140° / 360°, Φ = 0.25, μ_w = 0.55 cp.				

Examples

Two examples were taken from reference [1]. The input data are shown in Table 1. The four methods were applied using a short computer program (available on request) to calculate the cumulative water influx .The results are shown in Tables 2 and 3.

Table 2. Results of cumulative water influx calculated by different methods x10⁶bbl r_{eD} = 5

Time Year	t_D	Van and Hurst	Fekvich	Marsal	Modified
1	5.67	3.77	3.93	3.56	3.78
2	11.34	12.84	13.55	12.43	13.05
3	17.01	24.09	25.51	23.71	24.51
4	22.68	35.67	37.98	35.72	36.46
5	28.35	47.25	49.95	47.43	47.70
6	34.02	58.02	60.88	58.33	58.25
7	39.69	67.76	70.64	68.15	67.84
8	45.36	76.23	79.00	76.68	76.24
9	51.03	83.36	85.93	83.84	83.32
10	56.70	89.21	91.47	89.77	89.11

Table 3. Results of cumulative water influx calculated by different methods x10⁶bbl re_D = 10

Tim Year	t_D	Van and Hurst	Fekvich	Marsal	Modified
1	5.67	3.82	2.72	2.65	3.25
2	11.34	13.46	10.35	10.09	12.20
3	17.01	26.44	21.88	21.35	25.46
4	22.68	41.92	36.46	35.59	40.94
5	28.35	59.10	53.31	52.07	57.61
6	34.02	77.46	71.75	70.13	76.00
7	39.69	96.66	91.27	89.92	95.40
8	45.36	116.14	111.30	108.92	115.37
9	51.03	135.46	131.35	128.62	135.37
10	56.70	154.29	151.06	148.02	154.98

CONCLUSION

The results obtained using the suggested modifications of the Marsal Equations indicate clearly that the the Marsal constants need to be varied based on the values of r_{eD} and t_D .It is suggested that the Marsal Equations be re –written in the following form:

$$J^* = r_{eD}^4 \ln(r_{eD}) / (r_{eD}^2-1) + C_1 (1 - 3r_{eD}^2)$$

$$W_{eD} = 0.5 (r_{eD}^2 -1) (1 - \text{Exp}(C_2 t_D / J^*))$$

Due to the limited data available for analysis it was not possible to develop an analytical relationship between C_1 and J^* or between C_2 and t_D.

The main objective of this paper was to show the importance of varying the C_1 and C_2 constants based on the values of r_{eD} and t_D to conform with original solutions of Van Everdingen and Hurst. Consequently, it is recommended that future work should be devoted toward development of such analytical relations.

Nomenclature

c_f = aquifer compressibility, psi^{-1}
c_w = water compressibility, psi^{-1}
c_t = $c_f + c_w$
h = aquifer thickness, ft
k = permeability, md
r_o = reservoir radius, ft
r_e = aquifer radius, ft
r_{eD} = dimensionless radius
t = time, year
t_D = dimensionless time
Φ = porosity, fraction
μ_w = water viscosity, cp

REFERENCES

[1] Dake,L.P. *Fundamentals Of Reservoir Engineering.*
[2] Van Everdingen A.F. and Hurst W.,1949. The Application of Laplace Transformations to flow proplems in reservoirs . *Trans. AIME.* **186**,305-324.
[3] Fetkovich M.J. A simplified approach to water influx calculations: finite aquifer systems *J .Pet. Tech.*, July , 814-828.
[4] Marsal D., 1982. Topics of reservoir engineering. Course Notes Delft University of Technology.

Petroleum Res. J. Vol. 16 (2004); P. 57–64, 2 Figs.

Veeniacythereis Ibnalhaithami and Veenia (Veenia) ibnalhazmi

Two New Ostracode Species from the Upper Cretaceous of Iraq

Jenan M. Taha Al-Bashir*

Veeniacythereis بن الهيثمي و *Veenia* بن الحازمي نوعان جديدان من طائفة الاستراكود ضمن طبقات الكريتاسي العلوي بالعراق

جنان محمد طه البشير

تم في هذه الدراسة التعرف على نوع جديد من طائفة الاستراكود أطلق عليه *Veeniacythereis* بن الهيثمي وأعتبر من الأنواع الدالة على الكريتاسي العلوي (التوروني العلوي والسنتوني) بالعراق.

كما تم توثيق مستحاثة أخرى من نفس الطائفة من جنس *Veenia* بن الحازمي (Butler and Jones) ضمن التوروني العلوي والكونياكيان. وقد تضمن هذا البحث وصف تفصيلي لهاتين المستحاثتين، كما تمت مناقشة مجالهما الاستراتيغرافي وتصنيفهما وأماكن تواجدهما.

Abstract: *Veeniacythereis ibnalhaithami sp. nov., a new ostracode species of Veeniacythereis Gruendel, 1968, was regarded as characteristic species for the Upper Cretaceous rocks (Upper Turonian –Santonian) in Iraq.*

Veenia (Veenia) ibnalhazmi a new ostracode species of Veenia (Veenia) Butler and Jones, 1957; was recorded from Upper Turonian – Coniacian age of Iraq.

The two species are described in detail and their stratigraphic range, taxonomy and occurrence are discussed.

INTRODUCTION

Subsurface samples were obtained from five drilling wells located in the Middle and South of Iraq as follows: East Baghdad Well-3, South Rumaila Well-104, Safawi Well-1, Ghalaisan Well-1, and Kifl Well-2 (Fig. 1).

These samples were collected from the Upper Cretaceous strata of the Khasib Shaley and detrital limestones, the Tanuma Fissile Shales and the Sadi marly limestones. The Khasib Formation is underlain unconformably by the Mishrif or Kifl Formations (Fig. 2).

Repository

The holotype specimens are deposited in the Department of Palaeontoloty, British Museum (Natural History); and the paratype specimens are deposited with the author's collections, and an internal catalogue numbering system has been used.

* Oil Research and Development Centre Baghdad – Iraq.

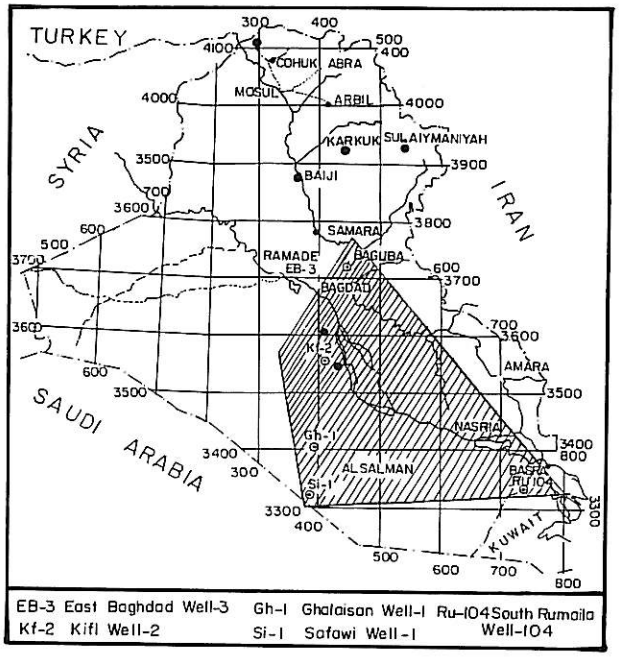


Fig. 1. Location map.

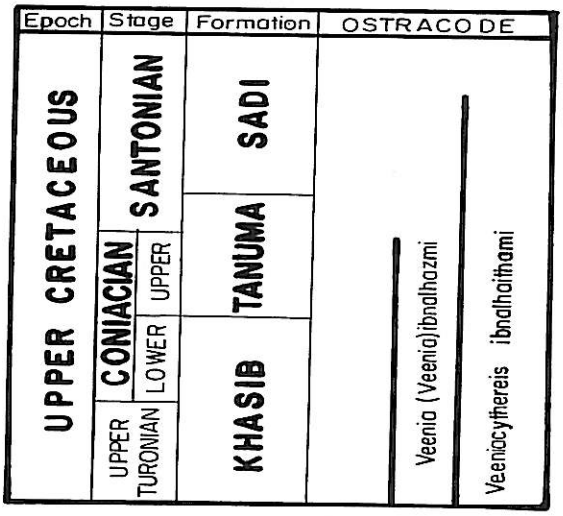


Fig. 2. Stratigraphic range chart of the two new ostracode species.

DESCRIPTION

Systematic description of the two new ostracode species is as follows:

A . Veeniacythereis ibnalhaithami

Systematic Description

Subclass	OSTRACODA	Latreille, 1806
Order	PODOCOPIDA	Muller, 1894
Suborder	PODOCOPINA	Sars, 1866
Superfamily	CYTHERACEA	Baird, 1850
Family	TRACHYLEBERIDIDAE	Sylvester-Bradley, 1948
Subfamily	TRACHYLEBERIDIDAE	Sylvester-Bradley, 1948

Genus *Veeniacythereis* Gruendel, 1973.
Veeniacythereis ibnalhaithami sp. nov. pl.1, figs,1-8.

Name: After Ali Al-Hasan Ibn Al-Haitham who was one of the most important mathematicians and physicists of the Arabs, in the tenth-eleventh century.

Diagnosis: A species of *Veeniacythereis* characterized by three longitudinal ridges, which show a tendency to divide into nodes. Surface of carapace varies from mainly smooth to partly reticulate; a prominent rounded tubercle lies in front of the subcentral tubercle at the antero-ventral corner, and consists of some small tubercles.

Holotype: Femal carapace, BM(NH)No.OS 12965, pl. 1 fig.1.

Paratype: J.T. (433-440), and J.T. (442-450).

Material: Total number of specimens found is 50. In South Rumaila Well-104, 22 specimens were found. In Ghalaisan Well-1, 7 specimens were found. In Safawi Well-1, 1 specimen only. In Kifl Well-2, 12 specimens were found and in East Baghdad Well-3, 8 specimens have been found.

Type Locality: South Rumaila Well-104.

Type Horizon: Khasib Formation, Upper Turonian-Lower Coniacian, depth of 2416m.

Stratigraphic range: UpperTuronian – Santonian.

Description: Carapace small, subquadrate to subrectangular in lateral view. Dorsal margin and ventral margins converging posteriorly into central pointed posterior end; dorsal margin straight; ventral margin weakly convex to slightly concave into selvage area. Anterior margin broadly and evenly rounded; posterior margin subtriangular. A well developed postero-cardinal angle in the left valve. Left valve with a pronounced hinge-ear on the antero-dorsal angle; left valve larger than the right. Eye tubercle rounded, large and prominent. Subcentral tubercle prominent, rounded and smooth; another prominent and smooth rounded tubercle lies at the antero-ventral corner of the carapace and clearly consists of some small

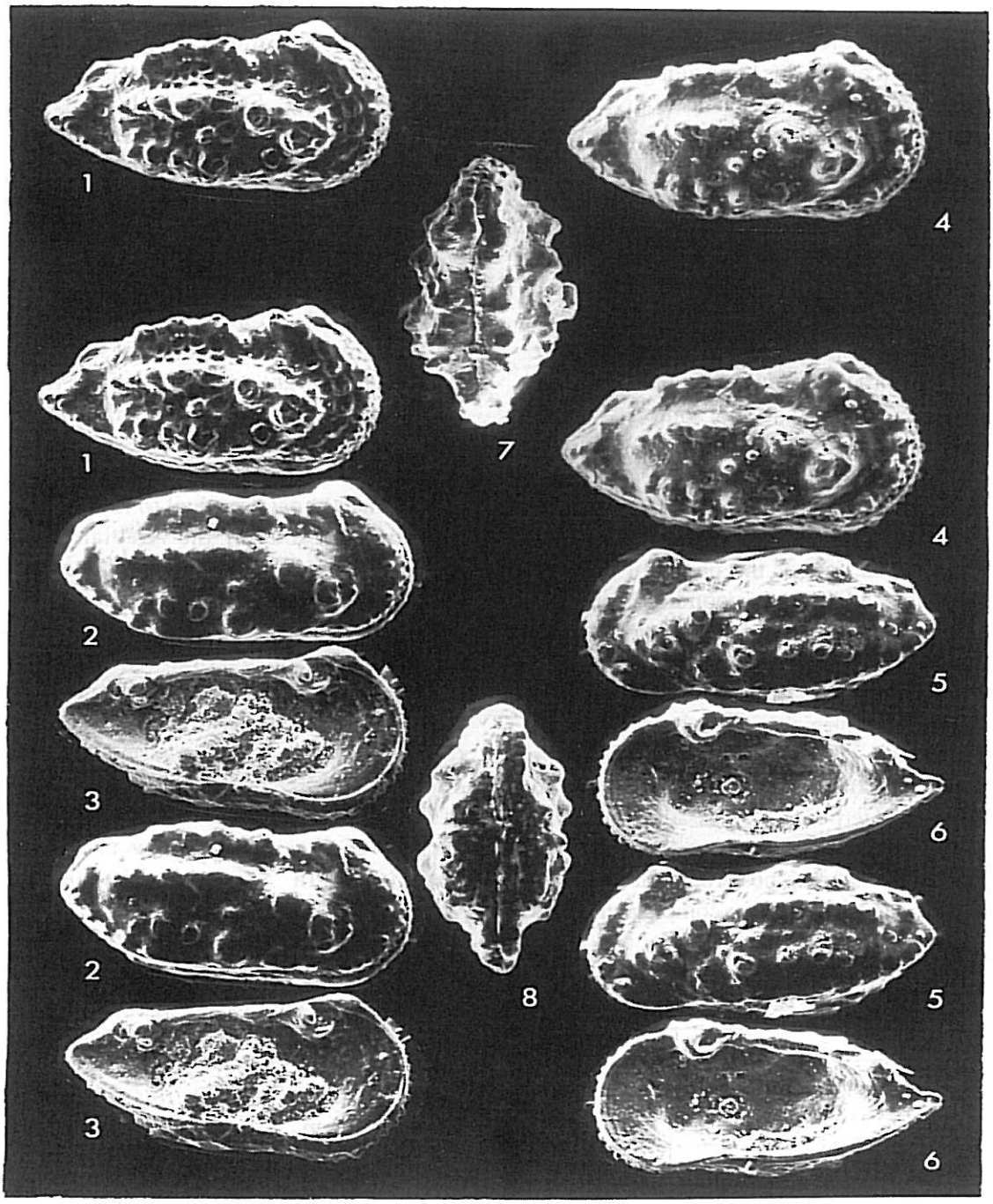


Plate - I

Veeniacythereis iIbnlhaithami sp. nov.

Plate I - 1 Female carapace, right valve, external, lateral view, (holotype OS 12965); stereoscopic paired photographs; South Rumaila Well-104, 2416m, Khasib Formation; X79.

Plate I - 2 Male carapace. right valve, external, lateral view, (paratype J.T. 434); stereoscopic paired photographs; Kifl well-2, 4365 ft, Tanuma Formation X75.

Plate I - 3 Female left valve, internal view, (paratype J.T. 443); South Rumaila Well-104, 2334m, Tanuma Formation; X78.

Plate I - 4 Female carapace, right valve, external, lateral view, (paratype J.T. 440); stereoscopic paired photographs; South Rumaila Well-104, 2352m, Tanuma Formation: X80.

Plate I - 5 Male carapace, left valve, external, lateral view, (paratype J.T. 433); stereoscopic paired photographs: Ghalaisan Well-1, 3725 ft, Tanuma Formation: X71.

Plate I - 6 Female right valve, internal, laterall view. (paratype J.T. 437); South Rumaila Well-104, 2416m, 2342m. Khasib Formation, X83.

Plate I - 7 Female carapace, external, external, view, (paratype J.T. 439); South Rumaila Well-104, 2380m, Khasib Formation; X73.

Plate I - 8 Female carapace, external, ventral view, (paratype J.T. 445); East Baghdad Well-3, 2290m, Tanuma Formation; X82.

tubercles. There are three longitudinal ridges which show a tendency to break into nodes. The dorsal ridge breaks into 3 or 4 nodes lying along the dorsal margin, these nodes usually coalesce giving the ridge a thickened and slightly sinuous appearance in lateral view. The median ridge is distinct and tuberculate, consisting, of 4 almost equal sized nodes which coalesce to form the ridge; the nodes are variably developed between specimens. The ventral ridge is broken into a series of 5-6 nodes parallel to the ventral margin. The surface of the carapace is variable from mainly smooth in most specimens to partly reticulate. The anterior marginal rim is present and has some 3-5 small pore cones or pustules; the anterior margin has some 10-14 small spines or rounded dentriculations; at the posterior margin there ar 4-5 pustules or rounded denticles and one pore cone or pustule lying at the dorsal part of the posterior margin. There are a few additional secondary nodes or very small pore cones between the major ones.

The Hinge is amphidont/heterodont, the anterior terminal hinge element of the right valve consisting of an anterior tooth with higher conical, smooth dorsal part and a lower ventral part which extends below the post-adjacent socket, giving a curved tooth in lateral view; the antero-median post-adjacent socket is deep, smooth and sub rounded, opened posteriorly and connected to a smooth postero-median groove. Elements of the left valve hinge complement those of the right. Muscle scars are not seen.

Dimensions: (in mm)

		L.	H.	L/H.
OS 12965	Holotype, Female, carapace	0.630	0.360	1.750
J.T. 442	Paratype, Female, carapace	0.610	1.350	1.742
J.T. 445	Paratype, Female, carapace	0.560	1.330	1.696
J.T. 439	Paratype, Female, carapace	0.630	0.380	1.657
J.T. 440	Paratype, Female, carapace	0.652	0.400	1.630
J.T. 443	Paratype, Female, LV	0.640	0.380	1.684
J.T. 437	Paratype, Female, RV	0.610	0.350	1.742
J.T. 433	Paratype, Male, carapace	0.720	0.350	2.057
J.T. 434	Paratype, Male, carapace	0.680	0.350	1.942

Discussion:

The specimens is assigned to *Veeniacythereis* Gruendel (1973) on the basis of the external appearance, the presence of a distinct hinge ear in the left valve, and well developed three longitudinal ridges; internally it has the same type of hinge structure.

Cythereis cf. OUM 1658-2 Grekoff (1968) illustrated by Grosdidier (1973, pl.12, Figs.89 a-d) from the Laffan Formation of the Coniacian ? of the coastal Fars Province of Iran, was considered by Grosdidier to be characteristic of that Formation and was reported from other areas. It seems to be similar to *Veeniacythereis ibnalhaithami* sp. nov. and Grosdidier,s figures indicate a somewhat similar variation to that seen in some specimens of *Veeniacythereis ibnalhaithami* sp. nov., *i.e.* the median ridge may be more or less ndose; figs. 89 a&d have an almost straight and non-nodose ridge, so if these forms are conspecific they extend the range of variation seen in the species. Sayyab (1956, unpublished Ph.D. dissertation) found specimens almost identical to this species in the Upper Cretaceous of the Arabian Gulf coast; which he named *Cythereis dukhanesis* sp.nov., describing its common occurrence in many wells along the Arabian Gulf. He placed his species in *Cythereis* stating that "the presence of a median tubercle, ventral and dorsal flanges and median ridge associated this species with *Cythereis*" however, he also remarks that "some doubt remains because of the poor preservation of the hinge". The ornamentation of the ventral surface in the ventral view is more clearly developed in Sayyab's species than in *Veeniacythereis ibnalhaithami* sp. nov. A more important difference was in the hinge which Sayyab described as having faintly crenulate anterior tooth and median groove; it is not clear how much importance should be attended to this observation. The figured specimens of *Cythereis* OUM 1658-2 illustrated by Grekoff (1968) from passage beds between the Coniacian and Santonian of Algeria, in pl.2, figs.24 a-d are not clearly illustrated, so giving a doubt as to whether they are identical to *Veeniacythereis ibnalhaithami* sp. nov. or not.

Occurrence:

This species known from the Upper Turonian-Santonian of South Ghalaisan Well-1, Safawi Well-1, Kifl Well-2, east Baghdad Well-3, and south Rumaila Well-104; in the latter well, it was found as contaminants in the highest lower Turonian. After Sayyab it is also recorded from the Upper Cretaceous strata of the western coast of the Arabian Gulf.

B. Veeniacythereis Ibnalhaithami

Systematic Description

Subclass	OSTRACODA	Latreille, 1806
Order	PODOCOPIDA	Muller, 1894
Suborder	PODOCOPIDA	Sars, 1866
Superfamily	CYTHERACEA	Baird, 1850
Family	TRACHYLEBERIDIDAE	Sylvester-Bradley, 1948
Subfamily	TRACHYLEBERIDIDAE	Sylvester-Bradley, 1948

Genus *Veenia* Butler and Jones, 1957
Subgenus *Veenia (Veenia)* Butler
And Jones, 1957
Veenia (Veenia) ibnaihazmi sp. nov.
pl. 2, figs. 1-8.

Name: After Abu Muhammad Ali Ibn Hazm, a versatile Spanish-Arab scholar, in the tenth and eleventh centuries.

Diagnosis: A species of *Veenia (Veenia)* with three longitudinal ridges (dorsal, median and ventral ridges), and smooth surface amongst the longitudinal ridges and rims with several pore cones. The median ridge joins the ventral ridge anteriorly; the area between the median and ventral ridge is raised. The anterior and antrto-ventral areas of the carapace are laterally depressed. Eye tubercle is pronounced. The posterior margin is triangular and elongate.

Holotype: Female carapace, BM(NH) OS 12963, pl. 2 fig. 1.

Paratype: J.T.9414 – 410).

Material: Total specimens are 7. In south Rumaila Well-104 section, 5 specimens have been reported.

Type Locality: South Rumaila Well-104 section.

Type Horizon: Tanuma Formation, Upper Coniacian, depth of 2342m.

Stratigraphic range: Upper Turonian- Coniacian.

Description: Medium sized, subtriangular carapace, with pronounced sexual dimorphism, males being more elongate than the females. Anterior margin evenly and broadly rounded, posterior margin elongate and triangular; dorsal and ventral margins sub-parallel in males, strongly converging towards posterior in the females; ventral margin concave in males, almost straight in females. A distinct eye tubercle is present; hinge ear only present in left valve, more prominent in females.

There are three distinct longitudinal ridges; the dorsal ridge is curved, the median ridge is straight, longer than the dorsal ridge; the ventral ridge is curved, seeming to join the median ridge at the anterior end.

There is no subcentral tubercle in the female, a slight subcentral tubercle is present in the male. An anterior marginal rim is present and bears 4-7 small pore cones. There are some 12 denticles along the anterior margin and some 4-6 denticles along the posterior margin.

The surface between these ridges and rims is smooth. Several pore cones can be observed. On the posterior area three prominent small pore cones are present; a small distinct node or pore cone lies in the median area of the valve, 2 prominent small spines lie near each other at the posterior end of the ventral ridge; dorsally there are six small pore cones that lie along the dorsal ridge and two small distinct pore cones are present at the anterior end. Internal features could not be observed.

Dimensions: (in mm)

		L.	H.	L/H.
OS 12963	Female (Holotype)	0.540	0.320	1.6875
J.T. 414	Male (paratype)	0.630	0.305	2.065
J.T. 415	Male =	0.640	0.325	1.969
J.T. 416,417	Male =	0.630	0.305	2.065
J.T. 418	Male =	0.635	0.330	1.924
J.T. 419	Female =	0.540	0.320	1.6875

Discussion: This species is tentatively placed in *Veenia (Veenia)* Butler and Jones (1957) because of its general external features, however no internal details are known.

ACKNOWLDGEMENTS

I would like to express my sincere thanks to the Oil Ministry of Iraq for providing the samples studied in this paper.

REFERENCES

Al-Bashir, J.M.T., 1986. Cretaceous Ostracoda of the

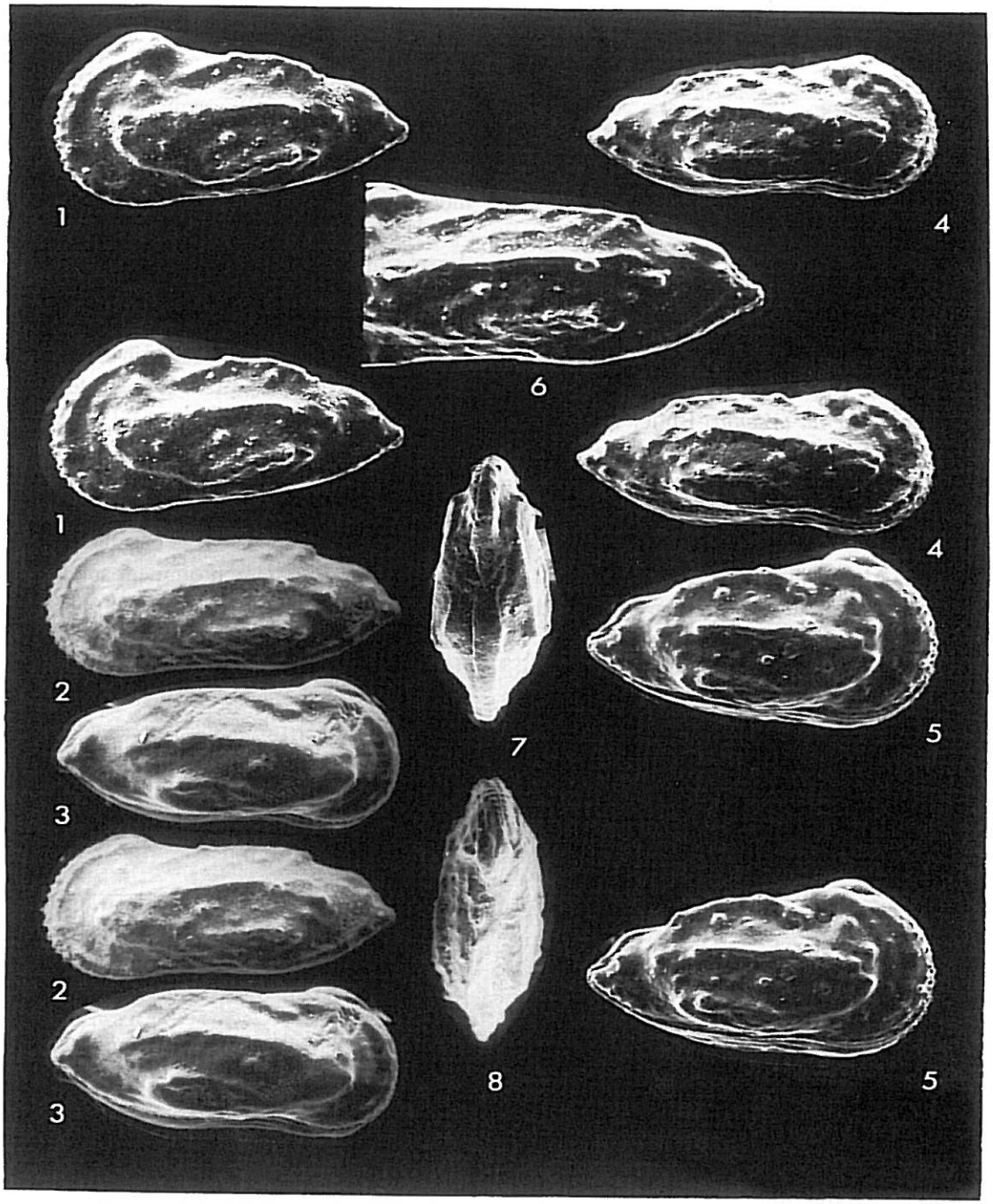


Plate - II

Veenia (*Veenia*) *ibnrhamzi* sp. nov.
All speciments from South Rumaila Well-104.

Plate II - 1 Female carapace, left valve, external, lateral view, (holotype OS 12963); stereoscopic paired photographs; 2342 m; Tanuma Formation; X94.

Plate II - 2 Male carapace, left valve, external, lateral, view, (paratype J.T. 416); stereoscopic paired photographs; 2342m; Tanuma Formation; X82

Plate II - 3 Male carapace, right valve, external, lateral view, (paratype J.T. 417); stereoscopic paired photographs; 2404 m. Khasib Formation; X79.

Plate II - 4 Male carapace, right valve, external, lateral view, ((paratype J.T. 415); stereoscopic paired photographs; 2340 m; Tanuma Formation; X79.

Plate II - 5 Female carapace, right valve, external lateral view, (paratype J.T. 419); stereoscopic paired photographs; 2374m, Tanuma Formation; X94.

Plate II - 6 Male carapace, left valve, external, postero-lateral view. (paratype J.T. 416); 2342m; Tanuma Formation; X91.

Plate II - 7 Male carapace, external, ventral view, (paratype J.T. 414); 2422m, Khasib Formation; X71.

Plate II - 8 Male carapace, external, dorsal view, (paratype J.T. 418); 2344m, Tanuma Formation; X70.

superfamily Cytheracea from Iraq, their biostratigraphy and correlation with adjacent regions, *Ph.D Thesis. University of Glasgow, Scotland*; 587p., 89pl., 19 figs., 7 tables.

Al-Bashir, J.M.T., 1988. Cretaceous and Lower Tertiary Ostracoda from Dhifriya Well-1 *O.E.C., Internal Report*, p.74, pl. 17, fig. 1, table 1, chart 1.

Butler, E.A. and Jones, D.E., 1957. Cretaceous Ostracoda of Protho and Rayburns Salt Domes Bienville Parish, Louisiana. Dept. Conserv., *Louisiana Geol. Surv. Bull.*, **32**, 1-65.

Grekoff, N., 1968. Sur la valeur stratigraphique et les relations paleogeographique de quelques ostracodes du Cretace, du Paleocene et de l'Eocene inferieur d'Algerie orientale. *Proc. 3rd African Micropaleont. Colloq. (Cairo).* 227-248. 3 pl.

Grosdidier, E., 1973. Associations d' ostracodes du cretace d' Iran. *Rev. Inst. France Petrole*. **28**.2., p. 131-169. pl. 1-15.

Grueendel, J., 1968. Neue Ostracoden aus der Salzbergmergel-Fazies (Santon) im Westlichen teil der Deutschen Demokratischen Republick. *Geol. Jb.*, **17**. 947-963.

Gruendel, J., 1973. Zur Entwicklung der Trachyleberididae (Ostracoda) in der Unterkreide und in der tieferen Oberrrrrkreide. Teil 1: Taxonomie. *Z Geol. Wiss. Berlin.* **1**.*11*:1463-1474.

Sayyab. A.S., 1956. Cretaceous Ostracoda from the Arabian Gulf-Area. *Ph. D. dissertation. State University of Iowa*: 138p., 5 pl.

Petroleum Res. J. Vol. 16 (2004): P. 65–76, 7 Figs.

Trace Elements and Stable Isotopes For The Abu Ghaylan Formation, Central Jabal Nafusah, NW Libya

Mahmoud T. El-Bakai*, Aisha K. Shalghoum* and Salama R. Ali*

العناصر الشحيحة والنظائر الثابتة لتكوين أبوغيلان في وسط جبل نفوسة – شمال غرب ليبيا

محمود البكاي وعائشة شلغوم وسلامة رحومة

يتكشف تكوين أبو غيلان في الجزء الشمالي الأوسط من جبل نفوسة شمال غرب ليبيا بين وادي غان شرقاً إلى الرابطة غرباً ، ولعوامل التعرية أكثر منها لأسباب الترسيب يختفي هذا التكوين في اتجاه الشرق بعد وادي غان.

ينتمي تكوين أبو غيلان للعصر الترياسي الأعلى والجوارسي المبكر ويمكن التعرف على هذا التكوين بمنطقة أبو غيلان وما جاورها لكونه محصوراً بين وحدتين من الصخور الرملية الحمراء هما تكوين أبوشيبة عند القاع وتكوين ككلة الفتاتي القاري من أعلى.

يتغير هذا التكوين جانبياً في اتجاه الغرب قرب كاف منطروس إلى سحنة مختلفة تسمى تكوين بئر الغنم. وتتشابه السحنات الصخرية لتكويني أبو غيلان وبئر الغنم، وكما ورد ذكره في عدة مراجع، مع رسوبيات الأرصفة الجيرية الضحلة.

من خلال المعلومات والنتائج المتحصل عليها من جهاز الأشعة السينية يمكن أن نعتبر أن تنظيم بلورات الدلومايت جيدة وأنه غير متعادل، أي أن نسبة جزيئاته من أكاسيد الكربونات إلى أكاسيد الماغنيسيوم غير متساوية.

بلغ متوسط قيمة نظائر الأكسجين الثابتة للدولومايت المتكوّن في رسوبيات أبو غيلان -1.66 بمقياس (PDB) بينما كان متوسط قيمة نظائر الكربون الثابتة له -0.28 (PDB). وتقل نظائر الأكسيجن الثابتة تدريجياً بازدياد العمق وهذا يعكس تزايد التصخر أثناء الردم أو دفن هذه الرسوبيات. ويحتوي الدولومايت في هذا التكوين عموماً على كميات ضئيلة من عناصر السترونشيوم والمنجنيز والصوديوم والحديد.

يمكن إستنتاج أنه هناك طريقتين ساهمتا في تكون الدولومايت أو إحلال الدولومايت محل الرسوبيات الأصلية لهذا التكوين وهما طريقة دخول ماء البحر إلى المستنقعات المالحة ليصبح سائل غني بالماغنيسيوم ومرور هذا السائل خلال الرسوبيات التي تعلوه ثم تبخر، أما الطريقة الأخرى فهي إختلاط المياه العذبة التي تمر خلال الرسوبيات إلى أسفل بمياه البحر المالحة المتسربة إلى الرسوبيات.

Abstract: *The Abu Ghaylan Formation is well exposed in north-centeral Jabal Nafusah, northwest Libya, between Wadi Ghan to the east and Ar Rabitah to the west. Abu Ghaylan Formation is missing towards the east owing to erosional factors rather than depositional.*

The Upper Triassic-Lower Jurassic stratigraphic section (Abu Ghaylan Formation) in the vicinity of Gharyan is easily distinguished at Abu Ghaylan and neighbouring areas where it lies between two red-coloured rock units, the Abu Shaybah Formation at

* Petroleum Research Centre, Tripoli, Libya.

the base and the continental clastics of the Kiklah Formation at the top.

The Abu Ghaylan unit further west grades into the Bir al Ghanam Formation near kaf Mantrus The lithofacies of the Abu Ghaylan as descriped in litrature, is analogous to the shallow shelf carbonates.

Two types of dolomite can be differentiated petrographically based on crystal size and precursor facies. The data gathered from XRD analysis suggest that the Abu Ghaylan dolomite types seem to be mainly non-stoichiometric and well-ordered.

Stable carbon and oxygen data are reported from dolomite and calcite from the Abu Ghaylan Formation. Surface dolomite samples have a mean $\delta^{18}O$ value of -1.66 per mil, and a mean $\delta^{13}C$ value of -0.28 per mil (all values are relative to PDB). Oxygen isotopic ratios become progressively lighter by depth, and reflect progressive lithification of the Abu Ghaylan sediments during burial.

The lack of significants in both carbon and oxygen isotopes from estimated values for the Upper Triassic-Lower Jurassic carbonate precludes meteoric influence during Abu Ghaylan diagenesis. Abu Ghaylan dolomites generally have low trace elements (Sr, Mn, Na and Fe) concentration.

Two mechanisms were involved in the formation of the Abu Ghaylan's dolomite; they are hypersaline reflux and mixed water.

INTRODUCTION

Abu Ghaylan Formation (Christie, 1955) in its outcrop is limited to the area between Wadi Ghan in the east and Ar Rabitah to the west of Jabal Nafusah (Fig. 1), north-western Libya. Locally thin section of Abu Ghaylan is exposed just east of Suk Al Ahad (Fatmi and Sbeta, 1991).

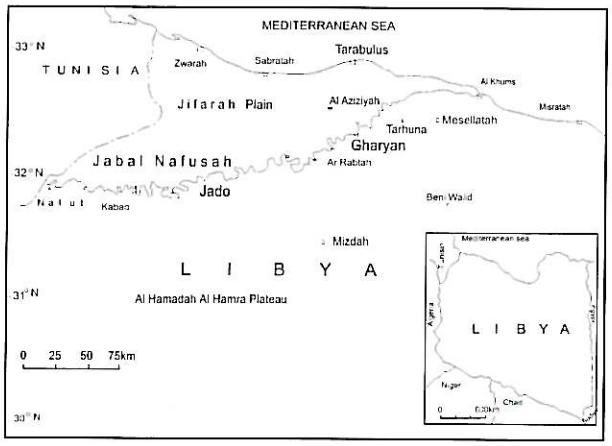


Fig. 1. Location map.

Abu Ghaylan Formation is missing towards the east (Fig. 2) owing to erosional factors rather than depositional (Desio *et al*, 1963; Burollet, 1963a and b; Magnier, 1963). This formation passes to the west into the Bir al Ghanam Formation, which is composed mainly of gypsum. The thickness of the Abu Ghaylan carbonates in the type section at Abu Ghaylan area is about fifty eight meters. It is composed mainly of light-coloured white to buff to light brown dolomite and dolomitic limestone. The lower twenty meters (Fig. 3) are highly fractured and recemented to form breccia (Fig. 4). Above the most fractured band a narrow layer of dolomitized oolitic limestone contains numerous small ghosts or indeterminate fossils.

The middle part is compact, recrystallized and yellowish massive dolomite. At the top the carbonate rocks are interbedded with clay, the upper most layers, however, being very hard, compact and oolitic. A trace of chert was found in this formation in Abu Ghaylan area which increases towards the west (south of Kaf Takut) forming a permanent resistant band.

Abu Ghaylan Formation occupies an intermediate position in the scarp face. It is easily distinguished at Abu Ghaylan and the neighbouring areas, where it lies unconformably between two red-coloured rock units, the Abu Shaybah Formation at base and the Kiklah Formation at top.

Owing to the lack of well-preserved fossils as a result of extensive dolomitization, the age of the Abu

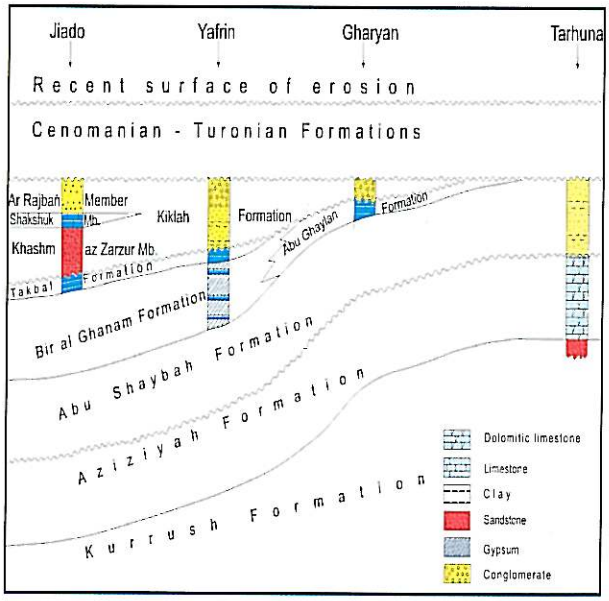


Fig. 2. Stratigraphic cross-section [(not to scale), after Fatmi and Sbeta, 1991].

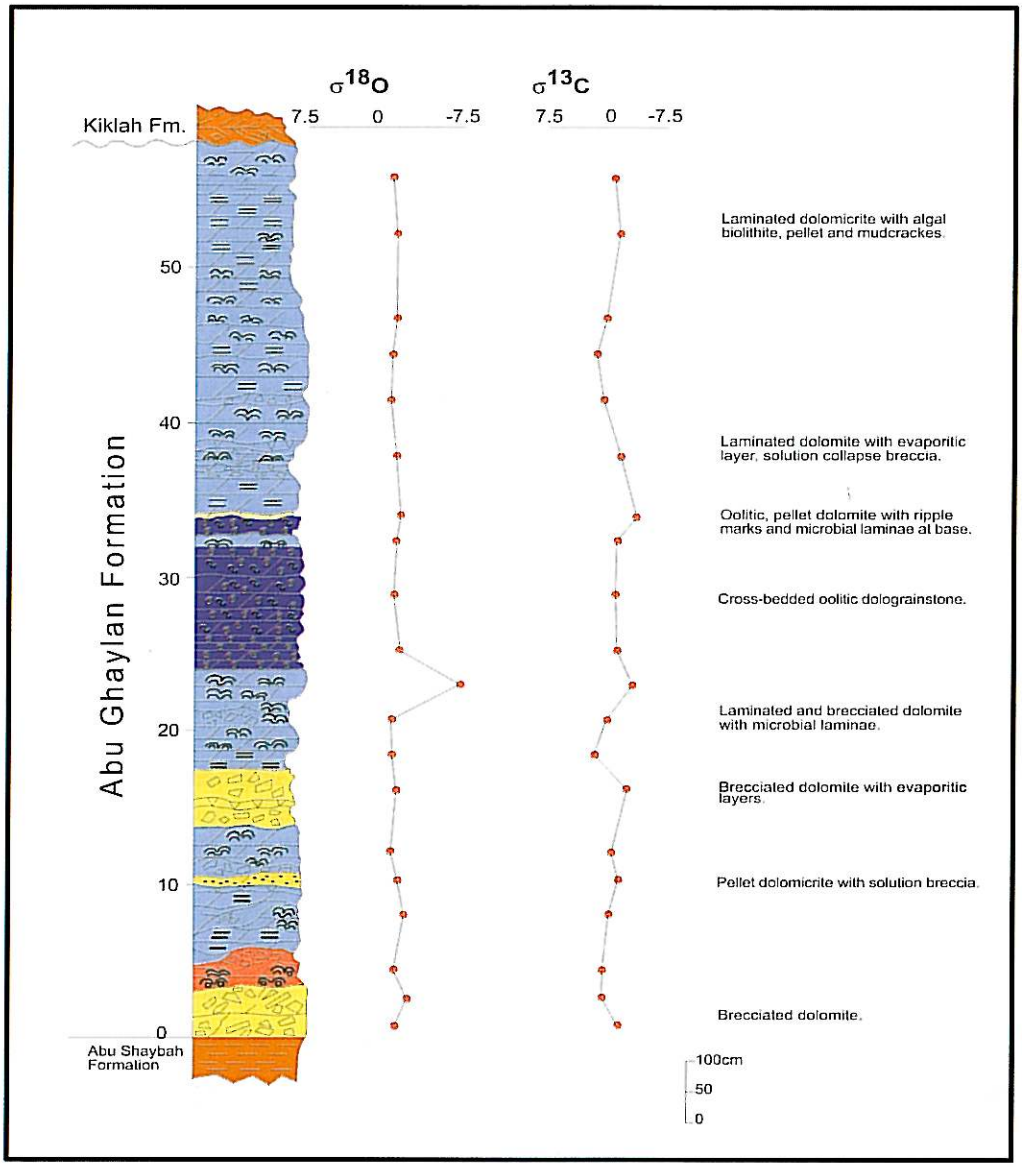


Fig. 3. Columnar section of the Abu Ghaylan Formation at Abu Ghaylan- Gharyan new road, in central Jabal Nafusah.



Fig. 4. General view of the Abu Ghaylan Formation showing collapse breccia. Photo was taken along the road approximately 1km west of Abu Ghaylan Police Station.

Ghaylan Formation is interpreted on the basis of its stratigraphic position. The Abu Ghaylan Formation and a part of the Bir al Ghanam Formation at top and the Abu Shaybah Formation were dated as Carnian (Christie, 1955), on the other hand the overlying middle and upper members of the Bir al Ghanam Formation are of Upper Triassic-Lower Jurassic age. Therefore, the age of the Abu Ghaylan Formation can be assigned to the time lapse between the Carnian and the Bajocian (Burollet, 1960 and El Hinnawy and Chesitev, 1975).

PETROGRAPHY

The extensive dolomite sequence of the Abu

Ghaylan Formation is fine crystalline and light-coloured white to buff to light gray brown in colour. Breccia with vertical fractures, microbial laminae and some dissolution vugs are distinctive characteristics.

Petrographically, the dolomites of the Abu Ghaylan Formation can be divided into two main types on the basis of crystals size and original sediments or precursor facies.

Type-I dolomite (Fig. 5) is very fine and is volumetrically dominated, non-ferroan and consists of dense interlocking, anhedral or nonplanar-a crystals less than 10 μm in size, with irregular intercrystalline boundaries. Type-I dolomite is non-mimetically replaced precursor mudstone or pellets and/or microbial mudstone/wackestone. The texture is mainly xenomorphic.

Type-II dolomite (Fig. 6) is non-ferroan commonly mimetic, preserving textural details of the precursor limestone (poorly to well-sorted bi-oolitic and oolitic packstone/grainstone), as well as depositional fabrics. Crystals of this type of dolomites which are present close to pore spaces are zoned with cloudy cores and clean rimes.

Calcite cement exhibits large, blocky crystals observed in some filling pore spaces, notably with irregular contacts with dolomite crystals. Some zones of the dolomite crystals are dissolved out and are replaced by calcite (calcitization or dedolomitization).

GEOCHEMISTRY

It has been shown that the geochemistry of dolomites, including their major and trace elements concentration and isotopic composition, is an essential complement to geologic and petrographic studies (Veizer, 1983).

Most diagenetic carbonates represent the alteration products of sedimentary phases that were originally crystallized from seawater. Over the past two decades, studies of modern seawater and sediment samples as well as ancient fossils permit the estimation of the trace element and stable isotopic composition of equilibrium marine carbonates for a given time (*e.g.* M'Rabet, 1981; Veizer, 1983; DePaolo and Ingram, 1985).

Abu Ghaylan formation extends westward and grades into Bir al Ghanam Formation. The latter sediments are mainly composed of massive gypsum and anhydrite and minor sandstone and clay. Bir al Ghanam Formation is thickening westwards where it was deposited in a continuously sinking shallow, mostly closed, sedimentary basin varying between lagoonal gypsum facies to open marine environment carbonate facies (Banerjee, 1980). Some samples were collected at the Bir al Ghanam village and adjacent areas for geochemical analysis.

Results of these analyses exhibit that the collected samples from the shale and carbonate beds of the

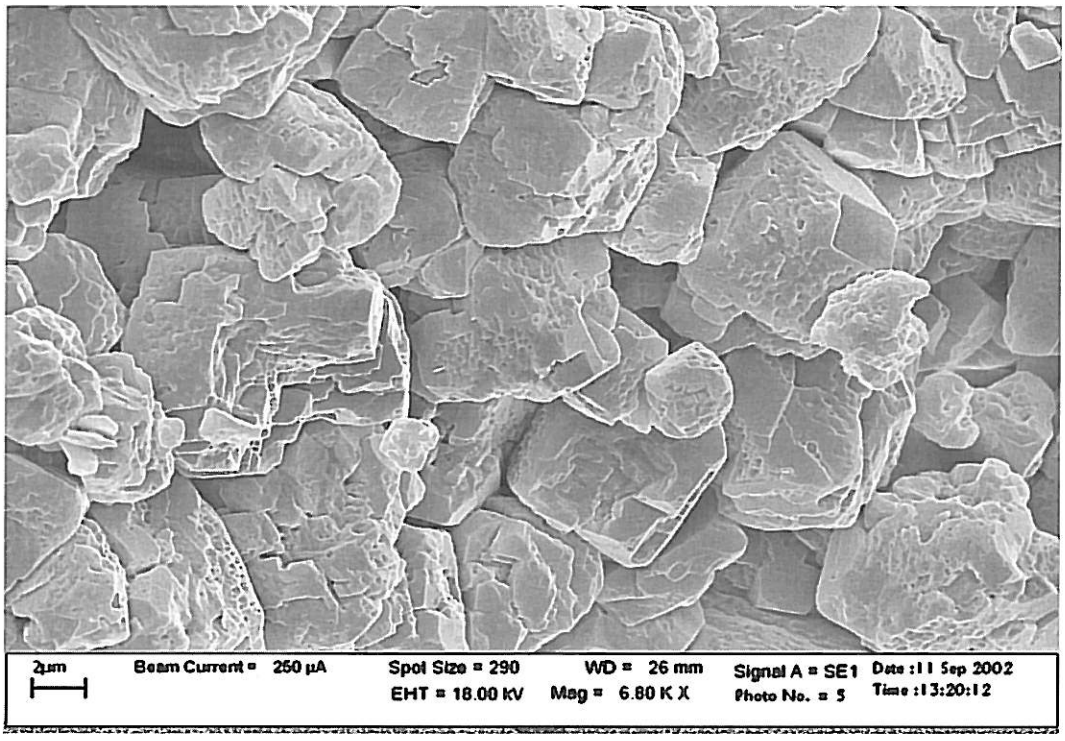


Fig. 5 Scanning electron photomicrograph of Type-I Dolomite.

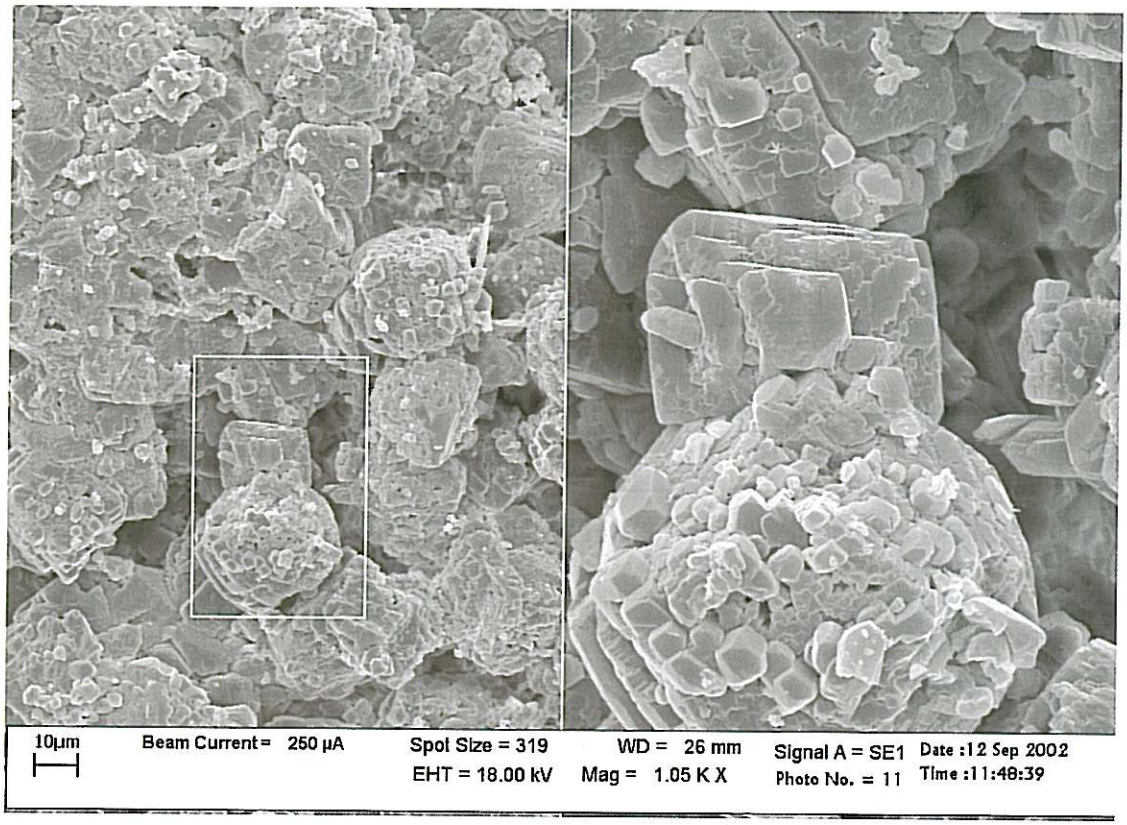


Fig. 6. Scanning electron photomicrograph of Type-II Dolomite.

Bir al Ghanam Formation are fair to good source rock with an average value of 1-3% total organic carbon (TOC) content. These sediments need further investigation in order to know their potential and their extention at subsurface which is expected to form a good source in the Jifarah Basin.

Stoichiometry and Crystal Order

As discussed by many authers such as Hardy and Tucker (1988); Tucker and Wright (1990), many if not most, natural dolomites are non-stoichiometric, i.e they do not have the ideal molar ratio of $CaCO_3/MgCO_3$ of 50/50. Stoichiometry of the Abu Ghaylan dolomite is determined by XRD analysis of whole rock powder . The $CaCO_3$ content was calculated using Lumsden's (1979) equation "Mole % $CaCO_3$= Md+B"; where M is (333.3), B is (-911.99) and d is the observed d-spacing (Å). This technique is also used in order to provide more information on the ordering of the dolomite crystals by dividing the intensity of peak (015) over peak (110). The greater the ratio of the highest of the ordering peak 015 to diffraction peak 110, the higher the degree of order (Tucker and Wright, 1990).

XRD data can be useful to distinguish between different types of dolomite within one carbonate formation, but with some overlap (Hardy & Tucker,1988), by plotting relationships between the ordering ratio versus the mole % $CaCO_3$ for all types of dolomite (Fig. 7a). Two types of dolomite can be recognized based on stoichiometry and ordering ratio from the data gathered from XRD analysis, the Abu Ghaylan dolomite types seem to be mainly non-stoichiometric and well-ordered.

The mole % $CaCO_3$ of very fine crystalline (Type-I) dolomite ranges from $Ca_{0.47}Mg_{0.53}$ to $Ca_{0.45}Mg_{0.46}$ with an average mole % $CaCO_3$ 50.1, and its ordering ratio ranges from 0.58 to 0.83 with an average of 0.71. However, mole % $CaCO_3$ of type-II dolomite ranges from $Ca_{0.46}Mg_{0.54}$ to $Ca_{0.53}Mg_{0.47}$ with an average mole % $CaCO_3$ 49.1, and its ordering ratio ranges from 0.46 to 0.95 with an average of 0.73.

Trace Elements

Trace elements concentration within the different dolomite types of the Abu Ghaylan Formation is determind by Atomic Absorption at Petroleum Research Centre Labs.

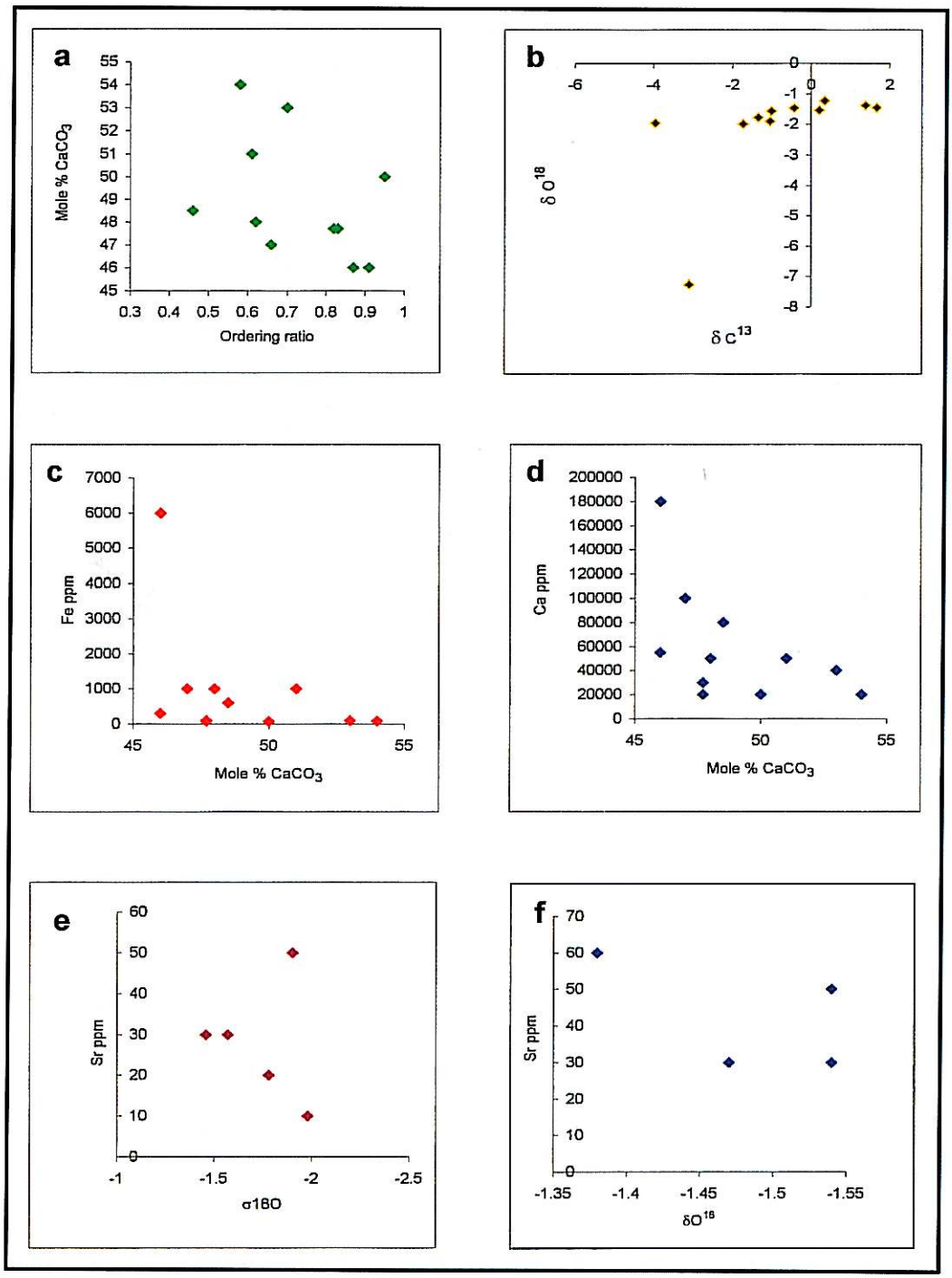


Fig. 7 Relationships between mole % Ca CO_3, trace elements, stable isotopes and stoichometry of the Abu Ghaylan dolomites.

Strontium

Strontium has received more attention in recent years than any other trace element in order to use it in the interpretation of formation of dolomite and diagenetic environment (Land, 1980).

The strontium concentration of the Abu Ghaylan Formation is generally low. Table (1) reports trace element concentrations in the Abu Ghaylan dolomites and in other dolomites reported in the literature.

The Sr concentration of Type-I dolomite of the Abu Ghaylan ranges from 10-30 ppm with an average of 20 ppm.

Type-II dolomite which replaced packstone and grainstone, has slightly higher Sr concentration. It ranges from 10-50 ppm, with an average of 28 ppm.

Table 1. Correlation of trace element concentrations in the Upper Triassic–Lower Jurassic Abu Ghaylan dolomites (this study) and various other dolomites reported in the literature:

Locality and Reference (s)	Formation (age) and dolomite type (s)	Sr (ppm)	Na (ppm)	Mn (ppm)	Fe (ppm)
Egypt	El Heiz Formation				
Holail *et al*, 1988	(Cenomanian dolom.)	120	650	1900	-
	El Hefhuf Formation				
	(Campanian dolom.)	103	425	720	-
U.S.A.	Smackover Fm.				
Moore *et al*,1988	(U. Jurassic)				
	Evaporitic dolomite	261-490	512-990	89-172	416-1200
	Early coarse dol.	42-69	117-185	42-137	51-114
	Early fine dolomite	40-89	129-212	59-710	58-2663
	Late- zoned replacive dolomite	53-83	112-192	110	689
	Late saddle dolomite	93-139	256-399	418-1571	3631-36294
Tunisia	Central Tunisia				
M'Rabet (1981)	(L. Cretaceous)				
	Dolomite associated with quartz	0-65	390-1370		11600-68100
	Dolomite associated with evaporite	6-175	440-1940		3000-11900
	Dolomite associated with palaekarst	0-90	440-950		2000-22600
	Dolomite associated with lacustrin	0-150	380-980		600-10800
U.S.A.Zenger and	Subsurface cores				
Dunham, 1988	(Siluro-Devonian)				
	Saddle dolomite	8	759	117	250
	Medium to coarse dol.	4	884	75	134
	Fine dolomite	8	832	74	154
	Coarse to fine dol.	4	1165	52	593
	Medium to coarse dolomite	9	1053	73	314
Tunisia Soussi and	Central Tunisia				
M'Rabet, 1994	(Jurassic)				
	Burial dolomite	0-50	65-2025	38-382	255-8290
Libya (this study)	Abu Ghaylan Fm., U. Triassic-L. Jurassic				
	Dolomite Type-I	0	238	34	320
	Dolomite Type-II	8	300	50	414

Sodium

Sodium concentration in diagentic phases is used in order to obtain more information about the salinty of the diagenetic fluids during preciptation and accordingly the mechanism responsible for dolomitization (Land,1980; Shukla,1988; Humphery, 1988).

Sodium in the Abu Ghaylan dolomites is generally low and its concentration is slightly lower in type-I (compared to Type-II dolomite).

It ranges from 130-320 ppm in Type-I, with an average of 238 ppm. Na concentration ranges from 110 to 680 ppm in type-II dolomite, with an average 300 ppm.

Manganese

Mn contents in Type-I dolomite of the Abu Ghaylan sediments are low, ranging from 15 to 50ppm, having an average of 34 ppm, Type-II ranges from 40-60 ppm, having an average of 50ppm.

Iron

Concentration of iron may provide information on the oxidation-reduction state of the diagentic environment. The low concentration probably represents preciptation from oxidizing diagentic water (Humphery, 1988 and many others).

Fe concentrations in Type-I dolomite ranges from 90 to 1000 ppm, with an average of 320 ppm, whereas Type-II is simlar to Type-I and it ranges from 70 to 1000 ppm with an average of 414 ppm.

Stable Isotopes

Whole-rock samples from Abu Ghaylan sediments were analysed for ^{18}O and ^{13}C isotopes. All isotopic measurments reported here are in per mil PDB values.

Average $\delta^{18}O$ and $\delta^{13}C$ of the fine crystalline dolomite Type-I are -1.4% and +0.91% respectively. $\delta^{18}O$ varies from -1.54 to -1.23% and $\delta^{13}C$ from +0.22 to +1.68% (Fig. 7b).

Type-II dolomite is similar to Type-I in terms of $\delta^{18}O$, but has depleted values in $\delta^{13}C$ compared to Type-I dolomite. Average $\delta^{18}O$ of this dolomite is -1.74 and it ranges from -1.46 to -1.98%. $\delta^{13}C$ values of dolomite Type-II range from -1.72 to -0.43%, with an average of -1.11% (Fig. 7b).

Calcites from Abu Ghaylan deposits show a widespread distribution of $\delta^{18}O$ (between -7.26 to -1.95%) and less variable of $\delta^{13}C$ (between -3.96 to -3.1%, Fig. 7b).

DISCUSSION AND INTERPRETATION

The origin of large scale ancient dolomite has been a controversial subject. Pervasively dolomitized ancient sequences such as the Abu Ghaylan Formation contrast with Holocene dolomites, which are extremely limited in both areal extent and occurrences throughout the world. No modern analogue exists for these extensive, thick, ancient dolomites.

The lack of a comparable present day analogue limits the application of information to develop models for ancient dolomites. Also, it has not yet proved possible to synthesise dolomite in laboratory at conditions which approxinate the earth's surface (low temperature; see Usdowski, 1994).

In considering models for thick, extensive dolomites in the past, a source for magnesium and a mechanism to pump the dolomitizing fluid through thick sediments must be found.

Land (1985) has pointed out that seawater is the only natural source for extensive dolomitization on the earth's surface. Sea water may be the ultimate source of Mg for many regionally extensive dolomite sequences. Dolomites are susceptible to varying source and composition, which may produce new textures and compositions on precursor phases (Banner, 1986; Gregg and Shelton, 1990; Kupecz *et al*, 1993; Nielson *et al*, 1994). Early diagenetic dolomites in many ancient carbonate platforms were formed by seawater, modified seawater and mixed meteoric-marine water (Adams and Rhodes, 1960; Mckenzie *et al*, 1980; Land, 1985; Machel and Mountjoy, 1986; Hardie, 1987; James *et al*, 1993; Sun, 1994).These early diagenetic dolomites are subsequencely altered, because they are intially metastable, calcium-rich phase (Land,1985). Many examples of alteration have been recognized in recent years (Banner *et al*, 1988; Kupecz *et al*,1993).

This study represents the first attempt of analysing trace elements and stable isotope composition of Upper Triassic-Lower Jurassic rocks from the Nafusah escarpment in north-west Libya and may shed light on the proceses of dolomitization of the Abu Ghaylan Formation in this area.

Type-I dolomite is very fine and non-plannar (Fig. 5). The absence of vugs and moldes that formed in the subsurface environments and dissolved core of some dolomite grains is typical of dolomite formed under near-surface low temperature. The non-ferroan character and low Fe content (Fig. 7c) of dolomite Type-I is further support for near-surface oxidizing conditions.

The sedimentary structures associated with the fine crystalline Type-I dolomite such as microbial laminae, layers of evaporite and solution collapse breccia suggest that this type is an early dolomite formed in supratidal-intertidal environment under the influence of refluxing brines. This type of dolomite is associated with evaporites, therefore, it is more variable in calcium contents (Fig. 5d), and the XRD for Type-I indicates that it is an early diagenetic dolomites precipitant from solution with relatively high Mg/Ca ratios which were probably evaporitic (reflux model).

The suggested model is consistent with the early timing and low Fe and Mn contents (average 320ppm and 34 ppm respectively).

Petrographic observation such as absence of exposure and invasion of meteoric water features in this type of dolomites does not favour mixing zone

origin. Moreover, oxygen isotope composition of this dolomite is higher than the general values estimated for marine calcite (0% to +2%) proposed by Hudson (1977). Therefore, Type-I dolomite is interpreted as being formed by the hypersaline reflux model.

Dense mosaics of fine crystalline (5-70m) planar-a and planar-s dolomite Type-II (Fig. 6) is typical of dolomites formed under near-surface low temperature (average C) saline to hypersaline conditions (Gregg and Sibley, 1984; Machel and Mountjoy, 1987; Zenger and Dunham, 1988; Gregg and Shelton, 1990). They are commonly mimetic, preserving textural details of the precursor limestones (Fig. 6) as well as primary depositional fabrics where these are not overprinted. Their isotopic composition is close to those values estimated for dolomites precipitated from sea water (Muntjoy and Amthor, 1994).

Type-II dolomite is moderately to highly ordered and non-stoichiometric, showing that this dolomite type was precipitated at an early stage from solution of low Mg/Ca ratio, which was probably more humid and non-evaporitic, suggesting mixed marine-meteoric fluids as the diagenetic solution for the Type-II dolomite formation (Badiozamani, 1973).

Type-II dolomite has low Sr content (average 28ppm). Dolomite which formed from aragonite, high-Mg calcite and low-Mg calcite during the early stages has high Sr contents (500-600ppm), this may indicate that the dolomite has been precipitated from hypersaline solution process (Tucker, 1982; 1983; Tucker and Wright, 1990). The Sr content of dolomite type-II does not favour hypersaline model. Instead, it favours a mixing zone solution which usually has Sr contents of 70-300 ppm (Rodgers *et al*, 1982; Tucker and Wright, 1990) and would support a high-Mg calcite precursor rather than aragonite (Veizer, 1978, 1983). Furthermore, the mimetic_textures of completely dolomitized ooides should have heavy isotopic composition if the precursor was aragonite.

Low Fe and Mn contents noted in dolomite type-II (average 44ppm and 50ppm respectively) clearly indicates diagenesis dominated by meteoric water under oxidizing conditions during dolomitization. On the others hand, marine and hypersaline dolomites clearly contain high Na concentrations, as would expected from precipitation of these diagentic environments.

Type-II dolomite contains low Na (average 298ppm) which falls within the range of dolomite whose origin is ascribed to mixed-water precipitation (Humphrey, 1988).

The isotopic compostion of Type-II dolomite which ranges from -1.98% to -1.46% ^{18}O and from -1.72% to -0.43% ^{13}C might suggest less variable fluid compositions than for Type-I dolomite. Therefore, Type-II dolomite probably was formed in a mixing zone of $\sigma^{18}O$ and $\sigma^{13}C$-enriched seawater and $\sigma^{18}O$ and $\sigma^{13}C$-depleted freshwater at low temperature ranges from 49°C to 52°C (average 51°C) assumuing σ_w = o%. The positive correlation between Sr contents and oxygen isotope values for Type-II dolomite (Fig. 7e) compared to the same relation for Type-I (Fig. 7f) may reflect lower salinity (M'Rabat, 1981) related to meteoric influences. Furthermore, oxygen isotope values of this dolomite are comparable to other values for dolomites attributed to a mixed water origin, such as Holocene dolomites from Jamaica (Land, 1973) and Upper Cretaceous dolomites from Egypt (Holail *et al*, 1988).

Finally, the strongly negative $\sigma^{18}O$ (-7.26%) and moderately light $\sigma^{13}C$ (-3.96%) of a calcite which survived dolomitization are consistent with calcite precipitation during later stage under the influence of fresh water.

ACKNOWLEDGEMENTS

Field work and sample processing of this research were funded by the Petroleum Research Centre (PRC) of the National Oil Corporation (NOC). Authors would like to extend their sincere thanks to Mr Osama Burshan and Miss Fowzia Lahmar for their patience during SEM performance.

We are grateful to Mr Jalal Siefanasar for his assistance and performance of XRD analysis.

We would like to thank all colleagues and friends in the Exploration and Exploitation Research Department of the PRC for their help and support.

REFERENCES

Adams, J. E. and Rhodes, M. L., 1960. Dolomitization by seepage refluxion. *Bull. Am. Ass. Petrol. Geol.*, ***44***, 1912-1920.

Assereto, A. and Benelli, F., 1971. Sedimentilogy of the Pre-Cenomanian formations of Jebel Gharian, Libya. In: C. Gray (ed) *Symp. Geology of Libya, Fac. Sci., Univ. Libya, Tripoli* 37-85.

Badiozamani, K., 1973. The Dorag dolomitization - application to the Middle Ordovician of Wisconsin. *J. Sed. Petr.*, ***43***, 965-984.

Banner, J. L., 1986. *Petrologic and Geochemical*

Constraints on the Origin of Regionally Extensive Dolomites of the Mississippian Burligtone and Keokuk Fms., Iowa, Illinois and Missouri. Unpublished Ph. D. thesis, State University of New York: 368p.

Banner, J. L., Hanson, G. L. and Meyers, W. J. 1988. Water-rock interaction history of regionally extensive dolomites of the Burligton-Keokuk Formation (Mississippian): Isotopic Evidence. In: V. Shukla,. and P. A Baker, (eds) Sedimentology and Geochemistry of Dolostones, *Spec. Publ., Soc. Econ. Paleont. Miner., **43,*** 97-113.

Banerjee, S. 1980. Stratigraphic Lexicon of Libya. *Industrial Research Centre, Tripoli, Bull., **13***, 300p.

Burollet, P. F. 1960. Lexique Stratigraphic International, **4**, Afrique, Pt. 4a, Libye. *Stratigraphic Commission, Cent.Nat. Rech. Sci.*, Paris., 62 P.

Burollet, P. F. 1963a. Le Trias en Tunisie et Libye. Relations avec le Trias Europeen et Saharrien. *86th Cong. Soc. Sav., Colloque Trias, Montpellier 1961: 1-15, Carte. Fr. Bur. Rech. Geol. Minieres, Mem., **15,*** 482-494.

Burollet, P. F. 1963b., Discussion of Libyan stratigraphy. *Rev. Inst. Petrole, **18,*** 1323-1325.

Christie, A. M. 1955 reprinted, 1966., Geology of the Garian area, Tripolitania, Libya. *Geol. Section, Bull., **5,** Kingdom of Libya, Ministry of Industry,* 64p.

DePaolo, D. J. and Ingram, B. L. 1985. High resolution stratigraphy with strontium isotopes. *Science, **227,*** 938-941.

Desio, A., Ronchetti, C. R., Pozzi, R., Cleici, F., Invernizzi, G., Pisoni, C. and Vigano, P. L. 1963. Stratigraphic studies in the Tripolitanian Jebel (Libya). *Riv. Ital. Paleont., Mem., **9,*** 126p.

El Hinnawy, M. and Cheshitev, G. 1975., Geological map of Libya, 1: 250,000: Sheet Tarabulus, NI33-13, Explanatory Booklet. *Industrial Research Centre, Tarabulus, Libya*, 65 p.

Fatmi, A. N. and Sbeta, A. M. , 1991., The significance of the occurrence of Abu Ghaylan and Kiklah formations east of Wadi Ghan, eastern Jabal Nafusah. In: M. J. Salem, A. M. Sbeta and M. R. Bakbak(eds) *The Geology of Libya,* Elsevier, London, ***VI:*** 2227-2233.

Gregg, J. M. and Shelton, K. L. , 1990. Dolomitization and dolomite neomorphism in the back reef facies of the Bonneterre and Davies formations (Cambrian), southeastern Missouri. *J. Sed. Petr., **60,*** 549-562.

Gregg, J. M. and Sibley, D. F. , 1984. Epigenetic dolomitization and the origin of xenotopic dolomite textures. *J. Sed. Petr., **54,*** 908-931.

Hammuda, O. S. , 1969. Jurassic and lower Cretaceous Rocks of Central Jebal Nefusa, Northwestern Libya. *Petr. Expl. Soc. Libya*, 74P.

Hardie, L. A. , 1987. Dolomitization: a critical view of some current views.*J. Sed. Petr., **57,*** 166-183.

Hardy, R. and Tucker, M. E. , 1988. X-Ray powder diffraction of sediments. In: M. E. Tucker (ed). *Technique in Sedimentology*, Blackwell, Oxford, 191-228.

Holail, H., Lohmann, K. C. and Sanders, I. , 1988. Dolomitization and dedolomitization of Upper Cretaceous carbonates: Bahariya Oasis, Egypt. In: V. Shukla, and P. A Baker,.(eds), Sedimentology and Geochemistry of Dolostones. *Spec. Publ., Soc. Econ. Paleont. Miner., **43,*** 191-207.

Hudson, J. D. , 1977. Stable isotopes and limestone lithification. *J. Geol. Soc. London, **133,*** 637-660.

Humphrey, J. D. , 1988. Late Pleistocene mixing zone dolomitization, southeastern Barbadose, West Indies. *Sedimentology, **35,*** 327-348.

James N. P., Bone, Y. and Kyser, T. K. , 1993. Shallow burial dolomitization of mid-Cenozoic, cool-water, calcitic, deep-shelf limestones, southern Australia. *J. Sed. Petr., **63(3):*** 528-538.

Kupecz, J. A., Montanez, I. P. and Gao, G. , 1993. Recrystallization of dolomite with time. In: R. Rezak, and , D. L. Lavoie (eds) , *Carbonate Microfabrics, Frontiers in Sedimentary Geology,* Springer-Verlag, New York: 187-194.

Land, L. S., 1973. Contemporaneous dolomitization of middle Pleistocene reef by meteoric water, north Jamaica. *Bull. Marine Science, **23***, 64-93.

Land, L. S. ,1980. The isotopic and trace element geochemistry of dolomite: the state of the art. In: D. H. Zenger, J. B. Dunham and R. L. Ethington (eds). Concepts and Models of Dolomitization. *Soc. Econ. Paleont. Mineral., Spec. Publ., **28,*** 87-110.

Land, L. S. ,1985. The origin of massive dolomite. *J. Geol. Education, **33,*** 112-125.

Lumsden, D. N., 1979. Discrepancy between thin section and X-ray estimates of dolomite in limestone. *J. Sed. Petr*, **49**, 429-436.

Machel, H. G.and Anderson, J. H. 1989. Pervasive subsurface dolomitization of the Nisku Formation in Central Alberta. *J. Sed. Petr., **59(6),*** 891-911.

Machel, H. G. and Mountjoy, E. W. ,1986. Chemistry and environments of dolomitization - a reapraisal. *Earth-Science Reviews, **23,*** 175-222.

Machel, H. G. and Mountjoy, E. W. ,1987. General constraints on extensive pervasive dolomitization-and their application to the Devonian carbonates of western Canada. *Bull. Can. Petr. Geol., **35(2),*** 143-158.

Magnier, P. ,1963. Etude stratigraphic dan le Gebel Nefousa et le Gebel Garian (Tripolitaine, Libye). *Bull. Sec. Geol. France, **5,*** 89-94.

McKenzie, J. A., Hsu, K. J. and Schneider, J. F., 1980. Movement of subsurface waters under the sabkha, Abu Dhabi, U.A.E., and its relationship to evaporative dolomite. In: D. H. Zenger, J. B. Dunham and R. L. Ethington (eds.). Concepts and Models of Dolomitization *Spec. Publ., Soc. Econ. Paleont. Miner., **28,*** 11-30.

M'Rabet, A., 1981. Diffrentiation of environments of dolomite dormation, Lower Cretaceous of central Tunisia. *Sedimentology, **28,*** 331-352.

Moore, C. H., Chowdhury, A. and Chan, L., 1988. Upper

Jurrassic platform dolomitization, northwesternof Mexico: a tale of two water. In: V. Shukla,and P. A. Baker (eds.). Sedimentology and Geochemistry of Dolomites, *Spec. Publ., Soc Econ. Paleont Minor.*, ***43***, 175-190.

Mountjoy, E. W. and Amthor, J. E., 1994. Has burial dolomitization come of age? Some answers from the western Canada sedimentary basin. . In: B., Purser, M., Tucker and D. J., Zenger (eds.). Dolomite a volume in honour of Dolomieu. *Inter. Assoc. Sediment., Spec. Publ.* ***21***, 203-405.

Nielsen, P., Swenen, R. and Keppens, E., 1994. Multiple-step recrystallization within massive ancient dolomite units: an example from the dinantian of Belgium. *Sedimentology,* ***41***, 567-584.

Rodgers, K. A., Easton, A. J. and Downes, C. J., 1982. The chemistry of carbonate rocks of Niue Island, south Pacific. *J. Geol.,* ***90,*** 645-662.

Shukla, V., 1988. Sedimentology and geochemistry of a regional dolostone: correlation of trace elements with dolomite fabrics. In: (eds) V. Shukla and P. A. Baker. Sedimentology and Geochemistry of Dolostones (ed. by:, and,.), *Spec. Publ., Soc. Econ. Paleont. Miner.,* ***43,*** 145-157.

Sun, S. Q., 1994. A Reappraisal of dolomite abundance and occurrence in the Phanerozoic. *J. Sed. Research,* ***A64,*** 396-404.

Soussi, M. and M'Rabet, A., 1994. Burial dolomization of organic-rich and organic-poor carbonates, Jurassic of centeral Tunisa. In: B., Purser, M., Tucker and D. J., Zenger (eds.). Dolomite a volume in honour of Dolomieu. *Inter. Assoc. Sediment., Spec. Publ.* ***21***, 429-445.

Tucker, M.E., 1982. Precambrian dolomites: petrographic and isotopic evidence that they differ from phanerozoic dolomites. *Geology,* ***10,*** 7-12.

Tucker, M. E., 1983. Diagenesis, geochemistry, and origin of a precambrian dolomite: The beck Spring dolomite of eastern California. *J. Sed. Petr.,* ***53(4),*** 1097-1119.

Tucker, M. E. and Wright, V. P., 1990. Carbonate Sedimentology. Blackell, Oxford: 482p.

Usdowski, E., 1994. Synthesis of Dolomite and Geochemical Implications. In: Dolomites A Volume in Honour of Dolomieu (ed. By: Purser, B., Tucker, M. and Zenger, D. J.), *Inter. Assoc. Sediment., spec. Publ.,* ***21***, 345-360.

Varol, B. and Magaritz, M., 1992. Dolomitization, time boundaries and unconformities: examples from the dolostone of the Taurus Mesozoic sequence, south-central Turkey. *Sed. Geol.,* ***76,*** 117-133.

Veizer, J., 1978. Simulation of diagenesis- a model based on strontium depletion: dscussion, *Can. J. Earth Sci.,* ***15,*** 1683-1685.

Veizer, J., 1983. Chemical diagenesis of carbonates: theory and application of trace element technique. *Soc. Eco. Paleont. Mineral., Short Course,* ***10,*** 30-1 to 3-100.

Zenger, D. H. and Dunham, J. B., 1988. Dolomitization of Siluro-Devonian limestones in a deep core (3,350m), Southeastern New Mexico. In: V. Shukla and P. A. Baker (eds.) Sedimentology and Geocemistry of Dolostones, *Spec. Publ., Soc. Econ. Paleont. Miner.,* ***43,*** 161-173.

Petroleum Res. J. Vol. 16 (2004): P. 77–82, 7 Figs.

Determination of Copolymer Composition Monomer Reactivity Ratios and Distribution Sequences of Different Acenaphthalene Copolymers Using the Ultra-Violet Absorption Method

Saleh A. Al-Zamzam

تعيين البوليميرات الأسنيفثالية التساهمية وتوزيعها التتابعي باستخدام طريقة إمتصاص الأشعة فوق البنفسجينة

صالح عبد السلام الزمزام

امتصاص الأشعة بواسطة الأنظمة البوليميرية المتصلة بوحدات أروماتية متدلية بالتفرع ينتج حالات مثارة ضوئياً. هذه الظاهرة جديرة بالاهتمام خاصة أن بعض نظام البوليميرات يمكن استخدامها في أنظمة تجميع ونقل الطاقة الشمسية.

تم تحضير بوليمر الاسنيفثالين بواسطة البلمرة بالمحلول عند 60° م. كما تم تحضير سلسلة من بوليمير الأسنيفثالين التساهمي مع الأكريلونيتريل والميثل أكريلونيتريل بواسطة البلمرة المستحلبية. وقد تم تعيين متوسط الوزن الجزئي اللزوجي يقع بين 18,000 و39,000 حسب نسب التركيز المختلفة لبوليمير الأسنيفثالين التساهمي، حيث تم تحضير تراكيز مختلفة من هذه البوليميرات (من 1-8) وتم تعيين امتصاصها لـ UV في التراكيز المختلفة على مدة طول موجي بين 250 إلى 350 نانوميتر وذلك باستخدام مطياف الأشعة فوق البنفسجية نوع كاري-14 وكذلك تم حساب نسبة تركيز الأسنيفثالين ونسبة فاعلية الوحدات في البوليمير التساهمي. حيث وجد أن مطياف الأشعة فوق البنفسجية يمكن استخدامه لتعيين تركيب البوليمير وكذلك التوزيع التسلسلي بطريقة مماثلة لطرق التحليل الفلزي ومعادلة التركيب البوليميري التساهمي. وبذلك تم تعيين متوسط أطول توالي السلاسل لبوليمير الأسنيفثالين التساهمي والتي وجد أنها متفقة مع الأطوال التي حسبت بمعادلة التركيب البوليميري التساهمي وهذا يوضح أن البوليمير التساهمي أسنيفثالين/اكريلونترايل مرتب على أساس تبادلي.

Abstract: *The absorption of radiation by polymeric systems containing pendent aromatic units produces photo-excited states. This phenomenon has generated considerable research interest since polymeric systems may be used for energy collection and transmission.*

Poly (Acenaphthalene) was prepared by solution polymerization at 60C°. A series of copolymers of Acenaphthalene and acrylonitrile were prepared by emulsion polymerization.The molecular weights of homopolymer of Acenaphthalene and its copolymers were determined experimentally by viscosity measurements for different runs. The average molecular weight (Mv) was found to be between 18000 and 39000 depending on the copolymer composition ratios in the runs.

Different feed ratios of homopolymers and copolymers were prepared in different run numbers (1– 8). Cary 14 Ultra–Violet absorption spectrophotometer was used to determine the UV absorption of polymers with different concentration at wavelengths range between 250–350 nm. Then the percentages of Acenaphthalene (ACN) in the copolymer and monomer reactivity ratios were calculated.

It was found that Ultra-Violet absorption spectroscopy can be applied to give similar results

* Al-Fateh University – Faculty of Engineering , Department of Chemical Engineering, Tripoli, Libya.

for the copolymer percentage composition and distribution sequences consistent with elemental analysis and copolymer composition equation. The average lengths of a given sequence has been calculated and the sequence length of ACN units in the copolymer are in close agreement with those obtained using the copolymer composition equation, indicating the highly alternating character of the copolymer Ploy (ACN-CO-AN).

INTRODUCTION

The absorption of UV energy by fluorophores attached to a polymer chain and the subsequent energy migration by way of excitons are subjects of theoretical interest [1-2]. This phenomenon has general considerable research interest since polymeric systems may be used for solar energy collection and transmission. The production of these electronically excited states in polymeric systems and the photophysical behavior associated with those states continue to be an active area of research[3-4]. The preparation of polyacenaphthalene Poly (ACN) and its copolymers with 2-vinylnaphthalene (2VN) Poly (ACN-CO-2VN), acrylonitrile (AN) Poly(ACN-CO-AN), methacrylonitrile (MAN) Poly(ACN-CO-MAN), vinylcarbazol (VC) Poly (ACN-CO-VC), and the studies of the Exciton migration on these copolymers using excited singlets, excimers or exciplexes which is limited by polymer structure were previously reported [5-6].

The overall efficiency of excimer formation will be determined by polymer chain conformation. A helical conformation allows stacking of chromophores outside the main coil of the copolymer. Thus, intramolecular association depends upon the repeated distance between the *trans* groups of the helix.

Ultra-violet absorption spectroscopy (UV) as a tool for the determination of Monomer reactivity ratios (r_1 & r_2) as well as the distribution sequences of copolymer.

Determination of the copolymer composition and knowing the monomer reactivity ratio is very important for knowing and determining the longest energy migration lengths.

The maximum energy migration lengths in copolymers of Acenaphthalene with acrylonitrile, methacrylonitriles, and 1-vinylnaphthalene with the percentages (47%, 5%, 78%) of ACN in each of the copolymer were reported to be 70, 88 and 94 angstrom respectively [7].

The percentage of Acenaphthalene (ACN) in the copolymers was determined by different methods. In this work Ultra-Violet absorption spectroscopy was applied to give good results which are similar to those obtained by the tedious process of elemental analysis. This accurate and easily-handled technique was developed for poly(ACN-CO-AN) and poly(ACN-CO-MAN) as shown in Tables 1 and 2.

Another important techniques is the determination of the degree of alteration by knowing monomer reactivity ratios runs r_1 and r_2. It is also possible to determine the distribution sequences of the copolymers chain in a quantitative manner.

This sequence distribution can be determined and calculated by Harrowed and Ritchey equation[8] based on the run number (R) which is defined as "the average number of uninterrupted monomer sequences for runs that occur in a copolymer chain per 100 monomer units".

MATERIAL AND EXPERIMENTAL METHODS

Poly(Acenaphthalene) was prepared by solution polymerization at 60C^0 using Azo-bis-isobutyronitrile (AIBN) as an initiator in dry degassed benzene. Copolymers of Acenaphthalene and acrylonitrile were prepared by emulsion polymerization. [9], in a mixture of water/ethanol, potassium persulfate was used as an initiator. Emulsifier and surfactant were added.

The molecular weights of homopolymer of Acenaphthalene and its copolymer were determined experimentally by viscosity measurements for different runs by Ostwald viscosity method at constant temperature for all runs, then the Mark Sakurada equation { $[\eta] = k M^a$} was used. Where $[\eta]$ is the intrinsic viscosity, (k) and (a) are constants which depend on the solvent. (k) = 3.0 x 10^{-4} and (a) = 0.594 for benzene used as a solvent [10]. The number average molecular weight was found to be between 18000 and 39000 according to the copolymer composition ratios in the runs.

Samples of homopolymer and copolymers of Acenaphthalene were purified by dissolving the polymers in 100-ml benzene and precipitated by 600 cm^3 methanol. Drying was carried out in a vacuum at 25 C^o. 0.1 g/l of each of the polymer and copolymers were dissolved in 1,2-dichloroethane and the following three concentrations were prepared 2 x 10^{-3} g/l, 4x10^{-3} g/l, and 8x10^{-3} g/l.

Different feed ratios of homopolymers and

copolymers were prepared in different run numbers (1 – 8).

Cary 14 Ultra – Violet absorption spectrometry was used to determine the absorption of polymers with different concentration at wavelengths between 250 – 350 nm.

RESULTS AND DISCUSSION

The UV absorption spectra for different concentrations of the homopolymer Acenaphthalene in 1,2-dichloroethane solvent and its copolymer Poly(ACN-CO-AN), were shown in spectra figures 1 and 2 respectively.

The percentage of ACN [F_1] in the copolymers was determined from UV absorption spectra. The absorption at 290, 300 and 306 nm were used to calculate the percentage of ACN in the copolymers. At 290 nm, Poly (ACN) has a strong absorption peak. For a concentration of $8x10^{-3}$ g/l the absorbance is 0.43 as shown in figure 1.

The percentage composition of ACN in the copolymer is given by the following equation :

$$F = \frac{A_{copoly.}\ g/l}{A_{homo.}\ g/l} \times 100 \qquad (1)$$

Where F is the percentage of ACN.

$A_{copoly.}$ is the absorption at concentration 6×10^{-3} g/l for the copolymer.

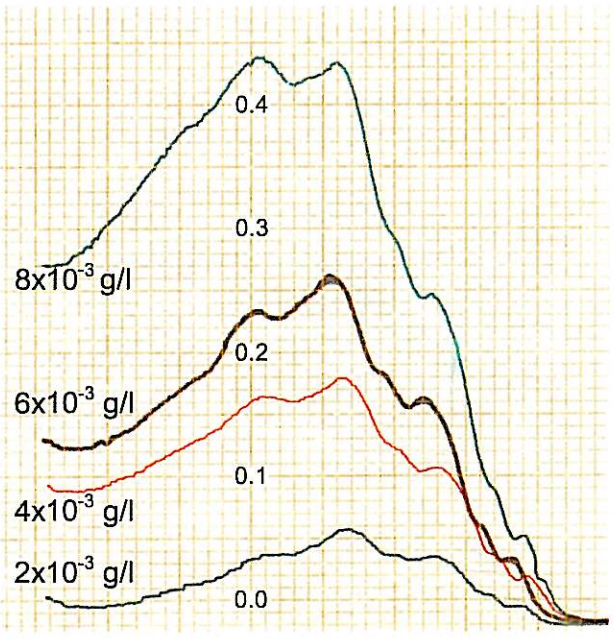


Fig. 1. UV spectrum of Poly(acenaphthalene) dissolved in 1, 2-dichloroethane at different concentrations, g/l. in, Abs 1.

A_{homo} is the absorbance at the same concentration for the homopolymer at a given wavelength.

Example :

run number 1:

$F_1 = \frac{0.10}{0.26} \times 100 = 38.5\ \%$ at λ 290 nm

$F_2 = \frac{0.65}{0.18} \times 100 = 36\%$ at λ 300 nm

The values in the denominator are obtained from figure 2.

These F values are listed in Tables 1 and 2.

The absorption at 290, 300, 306 nm. *vs*.concentrations of Poly (ACN) homopolymer plotted in figure 3 shows a maximum absorption at 290 nm.

The resulting values listed in Table 1 column (a) are the percentage of Acenaphthalene (F) in the copolymer Poly(ACN-CO-AN) calculated from experimental data of the UV absorption method. The

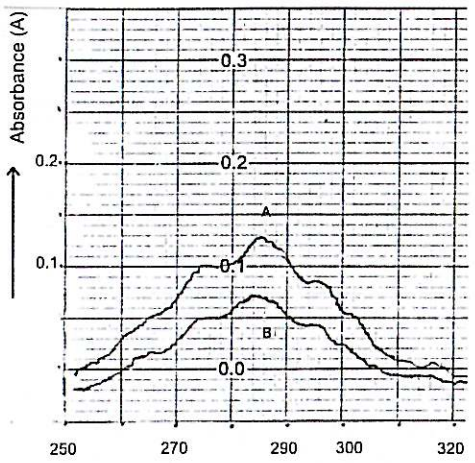


Fig. 2. Absorption of Poly(ACN-CO-AN), 36% ACN in copolymer, Concentration of curve A) ($6x10^{-3}$g/l), concentration of curve B (4×10^{-3} g/l).

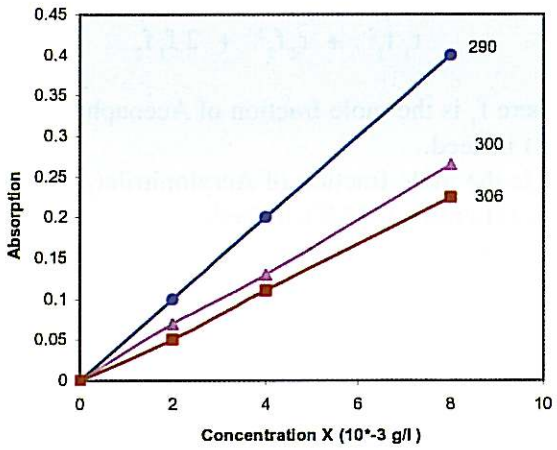


Fig. 3. Absorption (A) vs concentration of poly (Acenaphthalene).

values in Table 1 column (b) are the percentage of ACN of the same copolymer obtained by Nitrogen elemental analysis.

Similarly, values in Table 2 column (a) and (b) are the percentage of Acenaphthalene in the copolymer Poly(ACN-CO-MAN). F is the percentage of Acenaphthalene in the copolymer, (usually F is the mole fraction, here it is expressed as a percent).

Table 1. Composition of Poly(ACN-CO-AN)

Run numbers	ACN : AN feed ratio	% ACN (F) in incopolymer (a)	%ACN (F) copolymer (b)
1	1 : 9	38	36
2	2 : 8	47	48
3	3 : 6	66	76
4	4 : 6	78	84
5	5 : 5	76	82
6	6 : 4	80	89
7	8 : 2	90	91
8	9 : 1	95	94

Table 2. Composition of poly (ACN-CO-MAN)

Run numbers	ACN : MAN	%ACN (a)	% ACN (b)
1	0.05 : 0.09	14	16
2	0.03 : 0.97	07	09
3	0.01 : 0.99	04	05

Monomer reactivity ratios of Poly (ACN-CO-AN) and poly(ACN-CO-MAN) can be calculated by using the copolymer composition equation[8], which gives the copolymer composition as the mole fraction of monomer in the copolymer.

$$F_1 = \frac{r_1 f_1^2 + f_1 f_2}{r_1 f_1^2 + r_2 f_2^2 + 2 f_1 f_2} \qquad (2)$$

where f_1 is the mole fraction of Acenaphthalene (ACN) in feed.

f_2 is the mole fraction of Acrylonitrile(AN), or Methacrylonitrile (MAN), in feed.

r_1 is the monomer reactivity ratio of Acenaphthalene (ACN).

r_2 is the monomer reactivity ratio of Acrylonitrile (AN) or Methacrylonitrile (MAN).

F_1 is the mole fraction of Acenaphthalene (ACN) in the copolymer.

The plots of r_1 *vs* r_2 for run numbers 1,2,7 and 8 are shown in figure 4, for poly(ACN-CO-AN). Four lines crossed at (P) ($r_1 = 2.40$) and ($r_2 = 0.10$). By using these values the percentages of ACN in copolymers were calculated by equation (2)[7] and found to be in good agreement with UV data method.

The values of ACN composition in poly(ACN-CO-AN) which are listed in Table 1 were calculated by the Nitrogen weight % analysis as shown in Table 3 and figure 5.

Table 3. Weight percent Nitrogen and mole fractions of polymers.

Run No.	ACN :AN Feed ratio	Analytical (wt%) (a)	F_1 ACN (b)	F_1 AN (c)
1	1 : 9	10.09	0.36	0.64
2	2 : 8	7.22	0.48	0.52
3	3 : 6	2.48	0.76	0.24
4	4 : 6	1.58	0.84	0.16
5	5 : 5	1.83	0.82	0.18
6	6 : 4	1.02	0.89	0.11
7	8 :2	0.89	0.91	0.09
8	9: 1	0.68	0.94	0.06

(a) Theoretical wt. % N2 in the copolymer (ACN –CO – AN).
(b) Mole fraction ACN in the copolymer obtained by (1- F_{AN}).
(c) Mole fraction AN in the copolymer,obtained by reading the value of weight (N_2 %) directly from the graph (Fig. 5).

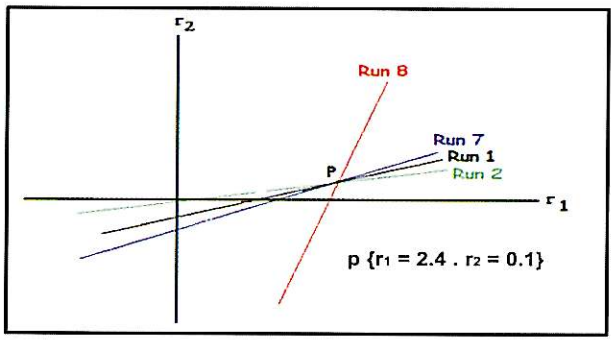


Fig. 4. Monomer reactivity ratios, r_1 *vs* r_2 in Poly (ACN-CO-AN).

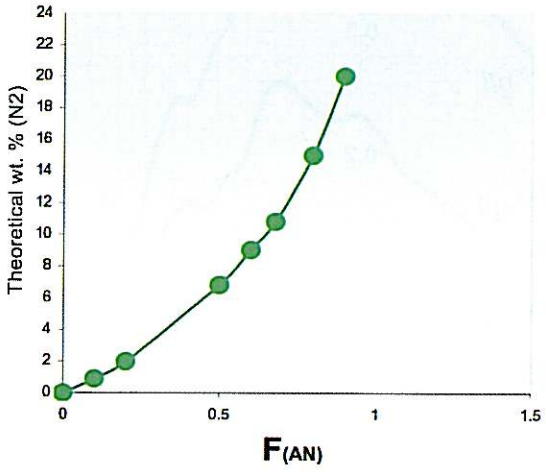


Fig. 5. Theoretical weight % (N2) *vs* Nitrogen F_{AN}.

The plots of mole fractions of ACN [F_1] in poly(ACN-CO-AN) and poly (ACN-CO-MAN) vs. the mole fraction of ACN in feed (f_1) are shown in figure 6 and figure 7.

Curve (A) shows the value calculated from the copolymer composition equation, where r_1 is 2.40 and r_2 is 0.1 for copolymer poly(ACN-CO-AN), r_1 = 2.38 and r_2 = 0.15 for the copolymer poly(ACN-CO-MAN).

Curve (B) shows the experimental data from UV spectra. The close agreement between curve (A) and curve (B) indicates the utility of quantitative UV analysis for the copolymers used in this work.

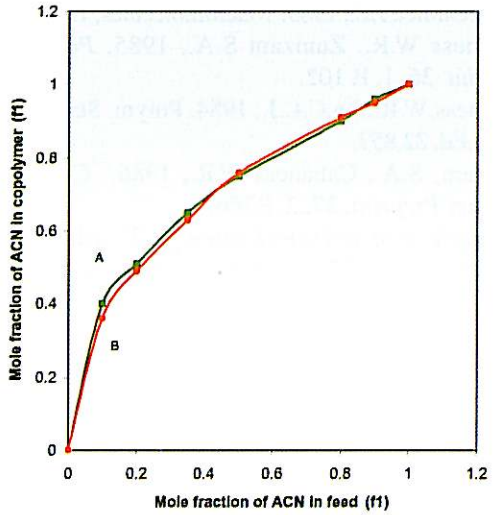


Fig. 6. mole fraction of ACN (F1) in poly (ACN-CO-AN) vs. mole fraction of ACN in feed f1. Curve A calculated from copolymer composition equation, Curve B calculated from UV absorption data.

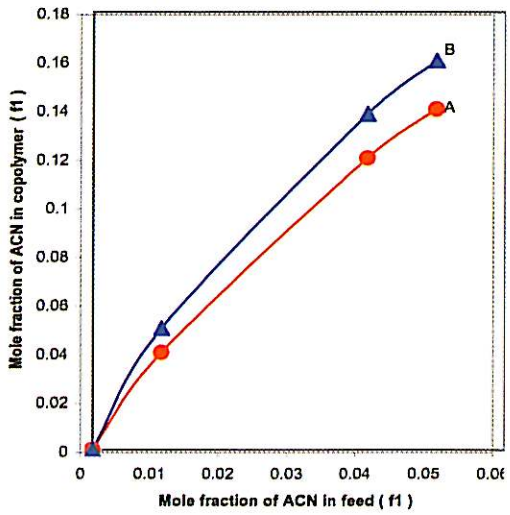


Fig. 7. mole fraction of ACN (F1) in poly (ACN –CO-MAN) *vs* mole fraction of ACN in feed f1,Curve A calculated from copolymer composition equation, curve B calculated from UV absoprtion data.

It is well known in radical copolymerization that when the $\Sigma r_1 . r_2$ product is zero or less than one, a perfect alternating copolymer is obtained, but when $\Sigma r_1 . r_2$ product is equal to one an ideal random copolymer is obtained. Since the product of the reactivity ratios $\Sigma r_1 . r_2$ for the ACN-AN copolymer is less than one and close to zero (2.4 x 0.1 = 0.2) then the copolymer has the tendency to alternate.

It is possible to determine the degree of alteration as well as the distribution of various monomer sequences in the copolymer chain in quantitative manner. Once the r_1, r_2, f_1, f_2, and F (% ACN) in the copolymer are known, it is possible to determine the sequence distribution. The calculation is based on the run number (R) which is defined as " The average number of uninterrupted monomer sequence (or runs) that occur in a copolymer chain per 100 monomer units" derived by Harwood and Ritchey as follows[8].

$$R = \frac{200}{2 + r_1 . f_1/f_2 + r_2 . f_1/f_2} \quad (3)$$

where f_1 and f_2 are the mole fraction of ACN and AN in feed respectively and $r_1.r_2$ are the monomer reactivity ratios of ACN and AN respectively.

The sequence distribution (Triads) can be calculated by the following relationship [8] :

$$F_{111} = \frac{[f1 - R/200]^2}{(f_1)^2} \quad (4)$$

$$F_{212} = \frac{[R/200]^2}{(f_1)^2} \quad (5)$$

$$F_{121} = \frac{[R/200]^2}{(f_2)^2} \quad (6)$$

$$F_{222} = \frac{[f_2 - R/200]^2}{(f_2)^2} \quad (7)$$

$$F_{112} + F_{211} = \frac{R/100\ [f_1 - R/200]}{(f_1)^2} \quad (8)$$

$$F_{122} + F_{221} = \frac{R/100\ [f2 - R/200]}{(f_2)^2} \quad (9)$$

$$\Sigma F_{ijk} = 2.0$$

The results of this calculation for triads are listed in table 4.

The average lengths of a given sequence can be calculated by: ACN= r x f1/f2 + 1

The sequence lengths of ACN &AN units in a

Table 4. Calculation for the triad fractions of poly (ACN-CO-AN)

(R)	Feed	ratio	F111	F212	F121	F222	F112+ F211	Total
67	2 : 8	0.25	0.97	0.20	0.28	0.0	0.22	1.92
58	3 : 6	0.02	0.70	0.18	0.32	0.20	0.49	1.91
53	4 : 6	0.12	0.44	0.19	0.32	0.31	0.41	1.80
44	5 : 5	0.31	0.19	0.19	0.31	0.49	0.49	1.98
35	6 : 4	0.50	0.08	0.18	0.33	0.38	0.49	1.97
17	8 : 2	0.79	0.01	0.18	0.32	0.18	0.47	1.95
08	9 : 1	0.90	0.17	0.16	0.36	0.08	0.48	1.98

copolymer of 47% ACN (feed ratio 2:8) are shown to be 1.6 and 1.4 respectively. These are in close agreement with the sequence calculated in table 4 indicating the highly alternating character of the (ACN-CO-AN) copolymer. These results of the sequence lengths and copolymer composition equation together with the quantitative absorption data give a good conclusion to support our evidence that alternating copolymers allow stacking chromophores outside the main coil of the copolymer and increase the efficiency of the energy (Exciton) to migrate along the chromophores of the copolymer so that energy may be transmitted or trapped.

REFERENCES

[1] Guillet, J.E;Rendall., 1986. Macromolecules, 19, 224.

[2] Burkhart, R.D.; Dawood, I., 1986. Macromolecules, 19,447.

[3] Winnik, M.A.,Slomkoski, S., 1986. Macromolecules, 19,500.

[4] Ren,x;Guillet, J.E., 1985. Macromolecules, 18,2012.

[5] Cabaness W.R., Zamzam S.A., 1985. *Polymer Preprint* **26**, 1, P. 102.

[6] Cabaness,W.R.; lin,C,L.J., 1984. Polym. Sci. Poly. Chem.Ed. **22**,857.

[7] Zamzam, S.A., Cabaness W.R., 1986. C.Chen, *Polymer Preprint*,.**27**,.2, P.366,

[8] *Principle s of polymerization*, " 3rd eddition, G.Odian, P.455- 457 , John Wiley & Sons, New York (1991).

[9] Cabaness W.R., S.A.Zamzam S.A. 1987. *Photophysics of Polymers* Charles E.Hoyle, John Torkelson, editors,Library of congress cataloging-in-publication data 1987 energy migration p.358.

[10] Brandrup.J,Immergut.E, Editor, 1975. *Polymer Handbook*, pp.IV,1 and 23 J. Wiley